Estimating Wave Attenuation through Diverse Floodplain Forests in the Netherlands

MSc Thesis Hydraulic Engineering
Eliane van Boxtel

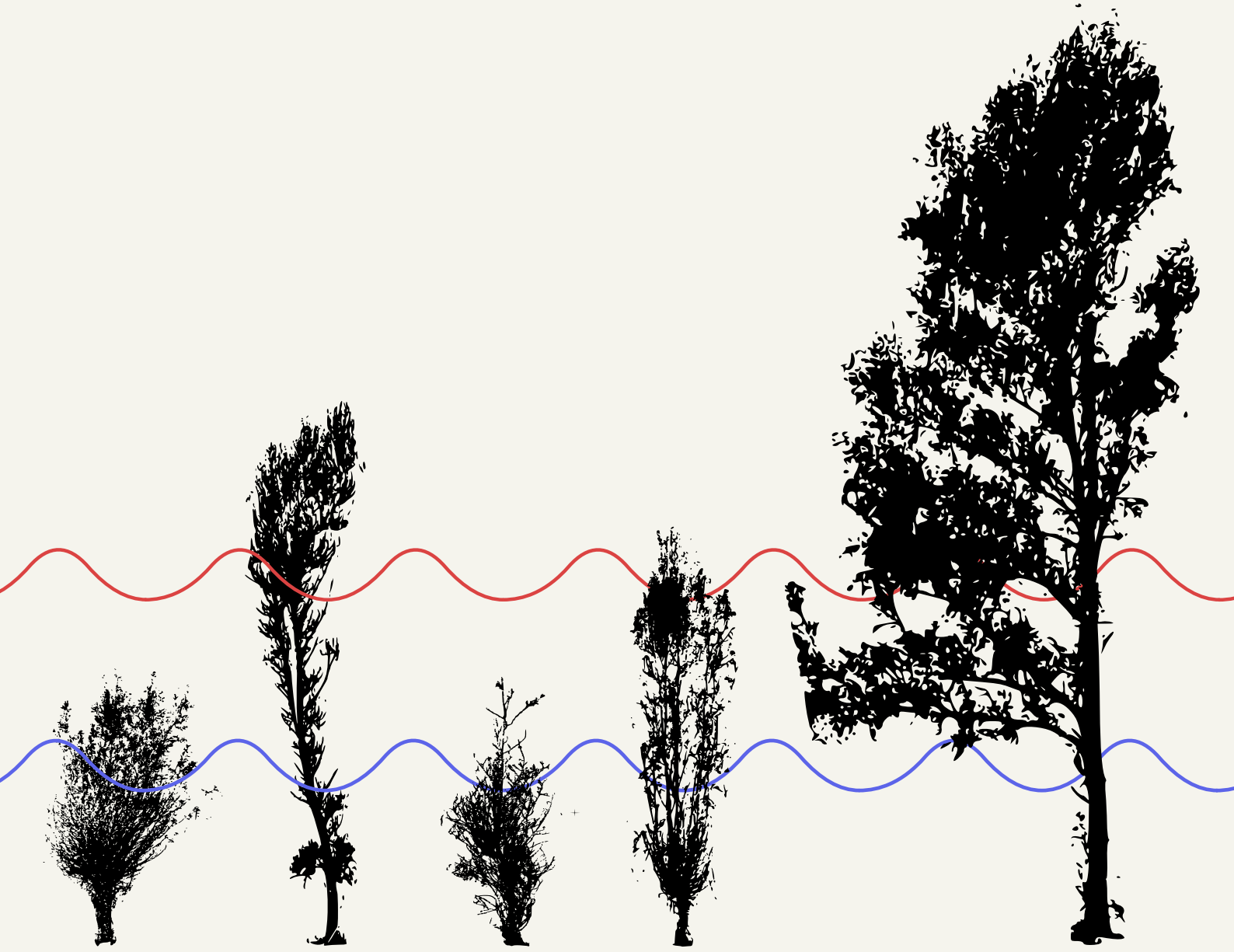

TU Delft

Estimating Wave Attenuation through Diverse Floodplain Forests in the Netherlands

by

Eliane van Boxtel

to obtain the degree of Master of Science
at Delft University of Technology
to be defended publicly on Thursday April 16, 2026 at 16:00.

Thesis Committee:	Dr. Ir. S. Kalloe	TU Delft
	Prof. Dr. Ir. B.K. van Wesenbeeck	TU Delft
	Asst. Prof. Dr. Ir. R.C. Lindenbergh	TU Delft
Project duration:	September 2025 – April 2026	
Faculty:	Faculty of Civil Engineering and Geosciences	TU Delft

TU Delft

Preface

My time at Delft University of Technology has strongly shaped the way I approach engineering challenges. Throughout my studies in Civil Engineering, I developed a growing interest in sustainability and an appreciation for interdisciplinary collaboration. Over the past years, I have come to value the importance of a holistic approach in which engineering, ecology, and sustainability reinforce one another. I came to realise that many of today's environmental challenges cannot be addressed from a single perspective, but instead require the integration of engineering knowledge with local, ecological, and environmental understanding.

This mindset guided my choice to specialise in Hydraulic Engineering, where the interaction between natural systems and engineering processes sparked my interest. The research presented in this thesis reflects this perspective by exploring how vegetation structure in riparian floodplain forests influences wave attenuation and how such ecosystems can contribute to nature-based flood protection strategies. The interdisciplinary nature of this research has made this project especially meaningful to me. This thesis represents both the final stage of my Master's degree in Hydraulic Engineering at Delft University of Technology and the culmination of the learning process I experienced during my time studying in Delft.

I would like to express my sincere gratitude to my supervisors for their guidance, support, and valuable feedback throughout this research. I greatly appreciated the different perspectives within the supervisory committee. The combination of insights from Terrestrial Laser Scanning, ecological understanding, and hydraulic engineering helped shape the direction of this research and broadened my perspective throughout the process. Their emphasis on developing a clear and coherent narrative challenged me to remain critical and focused on what was essential throughout the research process. The meetings and discussions during this project were particularly inspiring and have motivated me to continue working in this field.

Finally, I am deeply grateful to my friends and family for their support throughout my studies. Their encouragement, whether through long nights, lively discussions, or brainstorming sessions, has been invaluable, as have the many joyful memories we shared over the past years. I would also like to thank the many inspiring people I met during my time in Delft and the memorable experiences that enriched this journey, both academically and personally.

Eliane A. van Boxtel
Delft, April 2026

Abstract

Vegetated foreshores are increasingly applied as nature-based flood defence measures, yet field evidence quantifying wave attenuation capacity of structurally diverse natural forests under flood conditions remains limited. Furthermore, complex vegetation structure is often overly simplified in spectral wave models. This study investigates how diverse floodplain forest structure governs wave attenuation and evaluates Terrestrial Laser Scanning (TLS) as a method for deriving vegetation structural parameters across contrasting forest stands.

The performance of TLS was evaluated using a reliability framework that defined the maximum distance over which vegetation structure could reliably be extracted from the point clouds. Within this reliable domain, frontal surface area profiles ($a(z)$) were reconstructed and implemented in the phase-averaged wave model SWAN to simulate wave attenuation under varying water levels and wave forcing. Attenuation was governed by the interaction between submerged vegetation structure ($a(z)\,C_d(z)$) and wave orbital velocities ($u(z)$), resulting in dissipation proportional to $a(z)\,C_d(z)\,u(z)^3$. Pioneer and managed stands were characterised by concentrated low vegetation structure, limited horizontal patchiness, and structurally similar trees. Under moderate inundation conditions (1.6–4.0 m water depth above the forest floor), these stands produced the strongest wave attenuation with the smallest range of outcomes, with a median of approximately 40% and an interquartile range of 25–55% for a forest width of 100 m. Late-successional stands, in contrast, were characterised by vertically distributed vegetation structure, pronounced horizontal patchiness, and structurally complex, diverse trees. Under the same conditions, these stands produced lower and more variable attenuation, with a median of approximately 20% and an interquartile range of 5–55%. These results indicate that vertical vegetation structure primarily controls the magnitude of wave attenuation, whereas horizontal patchiness governs the variability of attenuation within forest stands. However, attenuation varied across hydraulic conditions and vegetation types, indicating that wave attenuation is not a fixed property of forest structure.

Compared to overly simplified, vertically uniform vegetation representations, TLS-derived $a(z)$ profiles improved structural realism and captured depth-dependent attenuation behaviour. By linking high-resolution TLS-derived vegetation structure to wave modelling, this study provides a quantitative framework for evaluating structurally diverse floodplain forests as nature-based flood defences.

Contents

Nomenclature

Abbreviations

Abbreviation	Definition
AHN	Actueel Hoogtebestand Nederland (National Height Model)
DBH	Diameter at Breast Height
FSA	Frontal Surface Area
GPS	Global Positioning System
Hydra-NL	Hydraulic boundary condition software developed by Rijkswaterstaat for probabilistic water level and wave statistics
JONSWAP	Joint North Sea Wave Project
KC	Keulegan–Carpenter (number)
MAE	Median Absolute Error
NAP	Normaal Amsterdams Peil (Amsterdam Ordnance Datum)
NND	Nearest-Neighbour Distance
SWAN	Simulating WAves Nearshore
TLS	Terrestrial Laser Scanning

Symbols

Symbol	Definition	Unit
$a(z)$	Frontal surface area density profile (vertical)	$[\mathrm{m}^{-1}]$
$a_i(z)$	Vertical frontal surface area density profile of subplot i	$[\mathrm{m}^{-1}]$
$a_{P_k}(z)$	Percentile-based vertical frontal surface area density profile	$[\mathrm{m}^{-1}]$
A_{crown}	Crown area in top view (2D convex hull)	$[\mathrm{m}^2]$
A_{ground}	Circular ground area within reliability distance	$[\mathrm{m}^2]$
$b_v N_v$	Frontal area density per unit volume (standard SWAN)	$[\mathrm{m}^{-1}]$
C	Azimuthal coverage fraction	[–]
C_D	Bulk drag coefficient	[–]
d	Scanner distance	[m]
d_{coverage}	Reliability distance criterion: azimuthal coverage	[m]
d_{density}	Reliability distance criterion: point density	[m]
d_{reliable}	Scan-specific maximum reliability distance	[m]
d_{tree}	Reliability distance criterion: tree detectability	[m]
$d_{\Delta z}$	Reliability distance criterion: vertical sampling	[m]
D	Representative vegetation diameter	[m]
D_{ij}	L_1 distance between normalised tree profiles i and j	[–]
ΔFSA	Stand-level horizontal patchiness metric	$[\mathrm{m}^2]$
Δz	Vertical layer thickness / vertical point spacing	[m]
Δz_{90-50}	Spread between 90th and 50th percentile of Δz	[m]

Symbol	Definition	Unit
FSA	Frontal Surface Area	[m^2]
FSA_{branch}	Branch frontal surface area	[m^2]
FSA_{stem}	Stem frontal surface area	[m^2]
FSA_{total}	Total (height-integrated) frontal surface area	[m^2]
g	Gravitational acceleration	[m/s^2]
h	Water level	[m]
H_s	Significant wave height	[m]
i	Tree or subplot index	[–]
KC	Keulegan–Carpenter number	[–]
N	Total number of radial bands / subplot realisations	[–]
N_c	Number of branches in diameter class c	[–]
N_{stem}	Number of stems intersecting the subplot slice	[–]
N_{woody}	Total woody element density (count) in subplot slice	[–]
$p(z)$	Unit-normalised vertical frontal area profile	[m^{-1}]
P_i	Point density in search volume around tree i	[pts/m^2]
P_k	k-th percentile (e.g. $k \in \{10, 50, 90\}$)	[–]
r	Radial band index	[–]
R	Branchiness Index	[–]
R^2	Coefficient of determination	[–]
S_{ij}	Pairwise tree shape similarity ($\in [0, 1]$)	[–]
S_{op}	Fictitious deep-water wave steepness	[–]
T_p	Peak wave period	[s]
$u_{\max}$	Maximum horizontal wave orbital velocity amplitude	[m/s]
v	Voxel edge length	[m]
W	Forest width	[m]
z	Elevation above ground level	[m]
α	Alpha-shape concavity parameter	[–]
δ_i	Binary tree detection indicator for tree i	[–]
Δr	Radial bin width	[m]
$\Delta\theta$	Azimuthal sector resolution	[°]
$\tilde{D}$	Median point density of occupied azimuthal sectors	[pts/m^2]

1. General Introduction

1.1. Relevance of Research

Around 55% of the Netherlands lies in flood-prone areas, of which approximately 26% is located below sea level (Eijgenraam et al. 2014). Climate change is projected to alter river flow regimes across Europe, affecting the magnitude, timing, and variability of discharge and placing increasing pressure on flood defence systems (Schneider et al. 2013). At the same time, population growth and economic development further increase the potential consequences and economic costs of flooding (Jongman 2018; S. Jonkman et al. 2013). Maintaining flood safety therefore requires continuous reinforcement of dikes and levees. However, conventional engineering solutions increasingly face spatial, environmental, and financial constraints. This has stimulated growing interest in Nature-based Solutions (NbS), which aim to combine hydraulic safety with ecological and societal benefits (Van Wesenbeeck et al. 2017; Vuik, S. N. Jonkman, et al. 2016; Temmerman, Meire, et al. 2013).

Vegetated foreshores are increasingly recognised as natural flood defences because vegetation attenuates waves and currents through drag-induced energy dissipation. Numerous studies have demonstrated that coastal ecosystems such as salt marshes and mangrove forests can substantially reduce wave loads on flood defences (Vuik, Borsje, et al. 2019; Gijsman et al. 2021; Temmerman, Horstman, et al. 2023; Möller et al. 2014; Van Loon-Steensma and Kok 2016). Incorporating vegetated foreshores into flood protection strategies can therefore reduce hydraulic loading and potentially lower construction and maintenance costs (Vuik, S. N. Jonkman, et al. 2016; Penning et al. 2016).

Similar mechanisms also occur in riverine environments. In Dutch floodplains, riparian vegetation, such as willow forests, frequently develops on river foreshores and can attenuate locally generated waves through drag forces exerted by stems and branches (van Wesenbeeck et al. 2022; Kalloe et al. 2022; van Starrenburg, Mancheño, et al. 2026; Ren et al. 2021). These findings highlight the potential contribution of floodplain forests to flood risk reduction along river dikes.

However, most existing studies focus on relatively uniform managed vegetation systems such as pollarded or planted willow stands. Natural riparian floodplain forests are structurally complex ecosystems shaped by dynamic hydrological conditions, species composition, and management history (Karrenberg et al. 2002; Markus-Michalczyk and Michalczyk 2023). As a result, these forests exhibit substantial variability in stem density, branching architecture, canopy layering, and vegetation height. Such structural characteristics directly control drag forces and frontal surface area exposed to incoming waves (Tinoco et al. 2020). Understanding how this structural variability influences wave attenuation is therefore essential for evaluating the potential of biodiverse floodplain forests as nature-based flood defences.

1.2. Problem Definition

Accurately representing vegetation in wave attenuation models remains challenging. Many models represent vegetation using overly simplified parameterisations such as arrays of rigid cylinders or coarse vertical vegetation layers (Mendez and Losada 2004). While these simplifications facilitate modelling, they neglect the structural heterogeneity of natural vegetation systems. In riparian floodplain forests, complex vertical distributions of vegetation elements can interact differently with wave orbital motion. These variations strongly influence vegetation drag and wave energy dissipation (Augustin et al. 2009; Tang et al. 2022), meaning overly simplified vegetation representations may lead to inaccurate attenuation estimates (Tinoco et al. 2020).

A key limitation in addressing this problem is the lack of detailed structural data for natural riparian forests. Terrestrial Laser Scanning (TLS) provides a promising approach for overcoming this limitation by capturing high-resolution three-dimensional measurements of forest structure. From TLS point clouds, structural metrics such as vertical frontal surface area distributions can be derived and incorporated into hydrodynamic models (Straatsma et al. 2008; Jalonen et al. 2015; Antonarakis, Richards, Brasington, and Muller 2010; Malhi et al. 2018; Dunlop et al. 2025). However, TLS measurements in dense forests are affected by occlusion and distance-dependent reductions in point density, which may introduce bias in derived structural metrics (Dassot et al. 2011; Wilkes et al. 2017). Assessing the reliability of TLS-derived structural parameters is therefore an important prerequisite before applying them in wave attenuation modelling.

This research investigates how structural variability in biodiverse riparian floodplain forests influences wave attenuation. Vegetation characteristics are derived from TLS measurements and complementary field observations and subsequently incorporated into the spectral wave model SWAN. By analysing how vertical vegetation structure varies between contrasting forest types and how these differences influence wave attenuation, this study aims to improve the representation of diverse vegetated foreshores in flood risk assessments and support their integration into nature-based dike protection strategies.

1.3. Research questions

The objective of this thesis is to investigate how variation in vertical vegetation structure in diverse riparian forests influences wave attenuation. Vegetation structure is quantified using Terrestrial Laser Scanning (TLS) and complementary hand measurements and subsequently incorporated into the spectral wave model SWAN. This objective is addressed through the following research questions:

Main question:
How does variation in vertical vegetation structure influence wave attenuation in diverse forests along Dutch floodplains?

Subquestions:
1. How does the accuracy of TLS-derived vegetation parameters vary across complex and diverse forest conditions?
2. How do different TLS-based processing methods influence the estimation of vertical frontal surface area density profiles?
3. How do different vegetation types vary in their vertical frontal surface area density profiles?
4. How do differences in vegetation structure, represented by vertical frontal surface area density profiles, influence wave attenuation?
5. How can the results inform the integration of diverse vegetated foreshores into flood risk assessments and forest management strategies?

As illustrated in Figure 1, these sub-questions are operationalised through three research components: validation and parameterisation of TLS-derived vegetation structure, observations of vegetation structure, and wave attenuation modelling.

1.4. Thesis structure

First, a literature review examines how vegetation influences wave attenuation and what role vegetated foreshores play in flood risk reduction. Insights from an exploration of an exist-

ing Terrestrial Laser Scanning (TLS) dataset informed the design of a targeted fieldwork campaign. Based on this preparation, new TLS measurements and complementary hand measurements were collected to characterise the vertical vegetation structure of diverse floodplain forests in the Netherlands. The collected field data are subsequently processed to derive vegetation structural parameters, including vertical frontal surface area density profiles. These parameters are then incorporated into the spectral wave model SWAN to analyse how differences in vegetation structure influence wave attenuation. The main results of this analysis are presented in a scientific paper included as a chapter in this thesis.

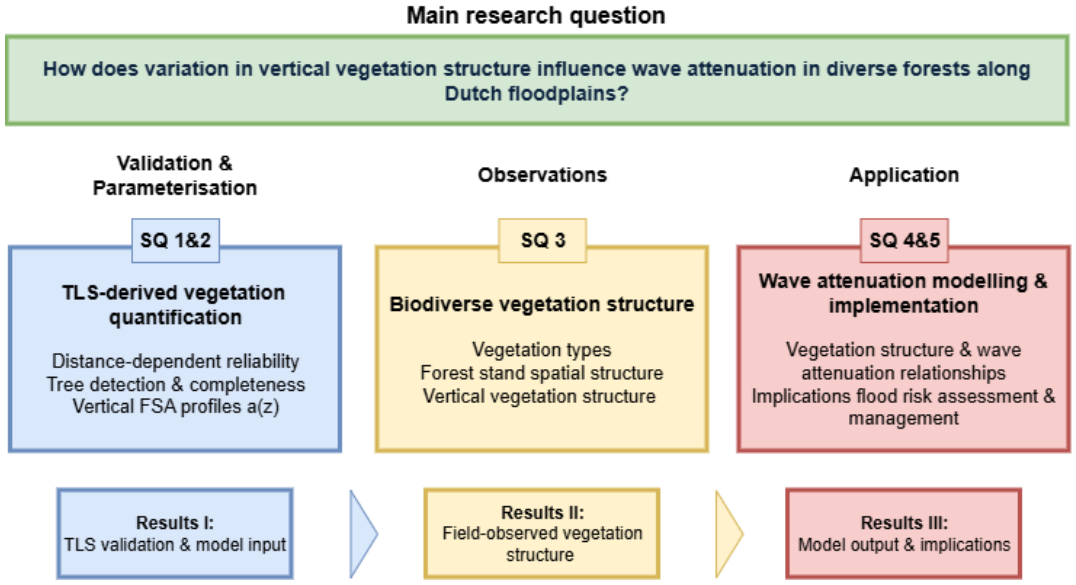

Figure 1: Conceptual research framework linking the validation and parameterisation of TLS-derived vegetation structure to wave attenuation modelling. The framework shows how the main research question is addressed through a sequence of sub-questions.

2. Theoretical Background

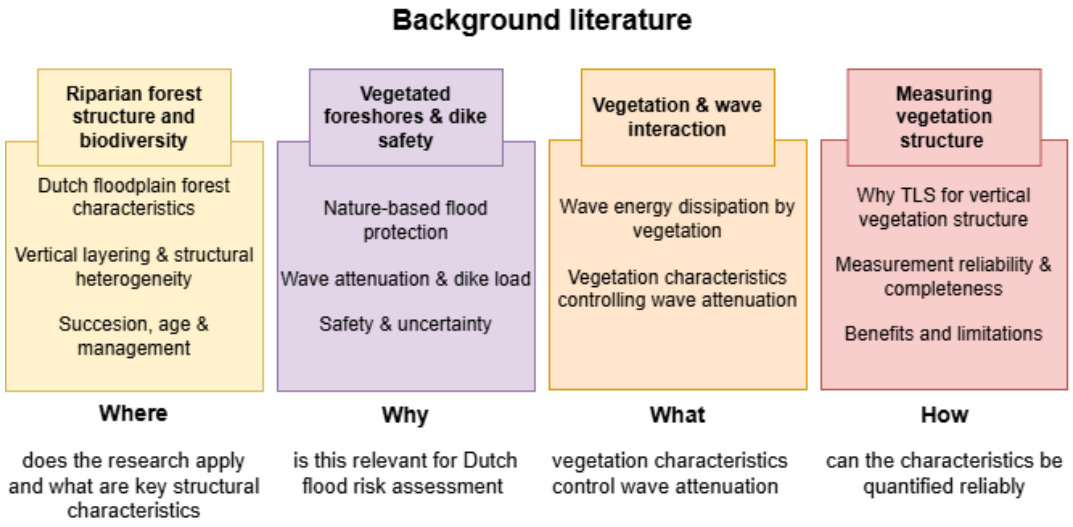

Figure 2: Conceptual framework guiding the focus and methodological choices of this research. Linking riparian floodplain forest structure (Where), the relevance of vegetated foreshores for dike safety (Why), vegetation–wave interaction processes (What), and methods for quantifying vegetation structure using TLS (How), highlighting key knowledge gaps related to wave attenuation in riparian forests.

Floodplain forests along Dutch rivers are structurally diverse systems in which vegetation traits vary both horizontally and vertically. This structural heterogeneity is relevant for flood risk reduction, because vegetation can dissipate wave energy and thereby reduce hydraulic loads on dikes. The magnitude of this effect depends on which vegetation elements interact with wave orbital motion at a given water depth.

As illustrated in Figure 2, this literature review brings together four research domains that directly support this study: (i) riparian forest structure and succession in Dutch floodplains, (ii) the role of vegetated foreshores in dike safety and flood risk reduction, (iii) vegetation–wave interactions and the structural characteristics governing wave attenuation, and (iv) methods to quantify vertical vegetation structure, with particular attention to the reliability of Terrestrial Laser Scanning (TLS) measurements. Together, these themes define the conceptual basis of the research and highlight the main knowledge gaps addressed in this study.

2.1. Riparian forest structure and biodiversity in Dutch floodplains

Riparian forests along Dutch rivers are structurally diverse systems, in which vegetation type, structure, and age vary across floodplain elevation gradients and vertical layers. Species composition typically reflects the local flooding regime. Softwood species, such as willow and poplar, dominate lower and frequently flooded zones, while hardwood species such as oak and elm occur in higher and less frequently flooded areas. Flooding duration is the strongest predictor of survival, followed by velocity, while depth is less important (Kramer et al. 2008).

However, riparian forest structure does not depend on hydrology alone. Local environmental conditions, species composition, and management practices can strongly influence forest development (Karrenberg et al. 2002; Markus-Michalczyk and Michalczyk 2023). As a result, riparian floodplain forests exhibit substantial variation in stem density, flexibility, and branching architecture (Markus-Michalczyk and Michalczyk 2023). Together, forest type, ver-

tical layering (canopy, trunk layer, and understorey), successional stage, and management determine the structural variability of riparian floodplain forests. This variability results in forest stands ranging from dense and relatively homogeneous pioneer vegetation to more open and structurally heterogeneous mature forests, which may interact differently with waves.

2.1.1 Softwood floodplain forest

Softwood floodplain forests occur in the lower parts of floodplains and are regularly inundated, and are dominated by willow and poplar (Oettel et al. 2022). Within about 50 years, these species form dense stands with relatively uniform canopy age and limited woody species diversity (Schnitzler 1994). As a result, softwood floodplain forests are typically characterized by high stem densities and relatively homogeneous vertical structures. Due to their low floodplain position and dense vegetation structure, softwood forests are expected to interact strongly with wave orbital motion.

2.1.2 Hardwood floodplain forest

Hardwood floodplain forests occur in the higher and less frequently flooded parts of floodplains and are typically dominated by elm, ash, or oak (Oettel et al. 2022). Compared to softwood forests, hardwood stands generally have a more open and irregular canopy structure with lower stem densities, which allows the development of species-rich understoreys and multiple vegetation layers (Schnitzler 1994). Hardwood forests are less tolerant of prolonged flooding, and therefore occur primarily in elevated floodplain zones where inundation frequency is lower (Oettel et al. 2022; Kramer et al. 2008). The resulting vertical and horizontal structural diversity suggests that hardwood floodplain forests may interact with waves differently than the denser and more homogeneous softwood forests.

2.1.3 Understory

Understorey vegetation forms an additional structural layer within riparian floodplain forests and contributes to vertical heterogeneity beneath the main canopy. Its development depends on forest type, flooding regime, successional stage, and management practices, resulting in variation within and between floodplain forest types.

In softwood floodplain forests, frequent inundation and disturbance often limit understorey development, resulting in sparse herbaceous layers or early successional shrubs. In contrast, hardwood floodplain forests typically support more developed and species-rich understoreys, due to lower flood disturbance, longer successional development, and more open canopy structures (Schnitzler 1994). Differences in canopy openness and light availability therefore play an important role in shaping understorey structure (McClain et al. 2011; Lecerf et al. 2016).

2.1.4 Management and age

Forest structure in riparian floodplains is strongly influenced by vegetation age, successional stage, and management practices. Succession drives transitions from open grassland and shrub-dominated vegetation to more mature forest structures, leading to systematic changes in stem density, vertical layering, and canopy development (Villarin et al. 2009). Management interventions such as mowing, grazing, or forest clearing can reset or redirect these successional trajectories, thereby altering forest structure over time (Makaske et al. 2011).

Makaske et al. (2011) demonstrated that successional stage and management strongly affect vegetation structure in floodplain environments, with shrubs and young successional stages producing higher hydraulic roughness than mature forests. These findings illustrate

how vegetation structure evolves with age and management, resulting in floodplain forests with contrasting structural configurations.

2.2. Vegetated foreshores and dike safety

Vegetation on foreshores can effectively attenuate waves and thereby reduce hydraulic loads on dikes. For this research, the specific focus is on the effect of river waves on biodiverse floodplain forests in front of dikes. Vegetated foreshores are therefore increasingly considered as nature-based components of flood defence systems, where vegetation contributes to wave attenuation before waves reach the dike.

Vegetation reduces wave loads primarily through drag forces exerted by stems and branches and through depth-induced wave breaking on shallow foreshore platforms. Numerous studies have demonstrated the effectiveness of this mechanism in coastal ecosystems. Salt marshes, mangrove forests, and reed fields can substantially reduce wave heights before they reach coastal flood defences, thereby lowering hydraulic loading on dikes and levees (Vuik, Borsje, et al. 2019; Gijsman et al. 2021; Temmerman, Horstman, et al. 2023; Möller et al. 2014). Including such vegetated foreshores in flood probability calculations has been shown to reduce the probability of dike failure (Vuik, S. N. Jonkman, et al. 2016). Vegetated foreshores can also contribute to flood risk reduction during failure events by lowering water level rise rates and limiting flood depths in the hinterland (van den Hoven et al. 2023).

Because vegetation can reduce wave loads, it is increasingly incorporated into hybrid flood protection strategies that combine engineering structures with natural systems. Such approaches can lead to more sustainable and cost-effective flood defence designs, for example by reducing the required crest height of levees (van Zelst et al. 2021). However, the effectiveness of vegetated foreshores depends strongly on their geomorphological development and ecological dynamics. Wave attenuation is typically most effective on wide and relatively elevated vegetated foreshores, whereas ecological value often increases under dynamic conditions with spatial variability in elevation and vegetation structure. Consequently, designs that allow natural foreshore dynamics may provide ecological benefits but also introduce uncertainty in wave attenuation capacity, which must be considered in dike safety assessments (Van Loon-Steensma and Kok 2016).

While most research on vegetated foreshores has focused on coastal ecosystems, similar mechanisms also occur in riverine environments. In Dutch floodplains, willow forests frequently develop on river foreshores and can interact with wind-generated waves. Recent studies have shown that pollarded willow stands can significantly attenuate wave heights due to the large frontal surface area of trunks and branches, which increases vegetation drag and wave energy dissipation (van Wesenbeeck et al. 2022; Kalloe et al. 2022; van Starrenburg, Mancheño, et al. 2026). These studies demonstrate the potential of riparian forests to contribute to dike safety, but they typically focus on relatively uniform managed stands.

In practice, the development of vegetated foreshores depends strongly on local hydrodynamic conditions. The pilot project described by (Penning et al. 2016) along the Houtribdijk in Lake Markermeer showed that high wave exposure can prevent vegetation establishment, resulting instead in the development of a dynamic sandy foreshore. This highlights that the effectiveness of vegetated foreshores depends not only on vegetation presence but also on local environmental conditions and vegetation structure.

In contrast to managed or experimental vegetation systems, biodiverse floodplain forests already exist along many Dutch rivers and form natural vegetated foreshores in front of dikes. These forests exhibit substantial structural variability in stem density, branching architecture, and vertical vegetation distribution, which may influence their effectiveness in attenuating

waves. Understanding how such structural variability affects wave attenuation is therefore important for evaluating the flood protection potential of riparian floodplain forests.

In riverine environments, the hydraulic loading acting on vegetated foreshores is largely controlled by locally generated river waves, whose characteristics depend on wind conditions, water levels, and navigation traffic.

2.3. River waves

It is essential to understand the types of river waves that affect floodplain forests along rivers and the adjacent dikes. In riverine environments, waves are primarily generated by wind acting on the water surface. Wide water surfaces, high water levels, and strong winds can generate significant wave heights that increase hydraulic loading on dikes (Ren et al. 2021). The development of wind-generated waves depends mainly on fetch length, wind speed, wind duration, and wind direction (Breugem and Holthuijsen 2007).

In addition to wind waves, ship-generated waves can also contribute to hydraulic loading in navigable rivers (Fenton et al. 2023). These waves are produced by vessel movement and depend on factors such as vessel size, sailing speed, water depth, and the distance between the ship and the shoreline (Dempwolff et al. 2022). In rivers with intensive navigation, ship waves may therefore contribute to the overall wave climate acting on floodplain vegetation and dikes.

For dike safety assessments in the Netherlands, hydraulic loading conditions are typically determined using probabilistic models such as Hydra-NL. Hydra-NL computes probabilistic distributions of hydraulic loads, including water levels and wind-generated waves, under varying meteorological and hydraulic conditions. These probabilistic wave conditions can subsequently be used as input for wave attenuation modelling in vegetated foreshores.

2.4. Wave-Vegetation interaction

Most experimental and numerical studies of wave–vegetation interaction rely on simplified representations of vegetation, such as rigid stems, uniform diameters, fixed heights, or regular planting patterns (Dalrymple et al. 1984; Mendez and Losada 2004; Anderson and Smith 2014; Augustin et al. 2009; Maza et al. 2015). While such simplifications improve experimental control and reproducibility, they can also bias the results by hiding or amplifying relevant physical processes found in natural conditions (Tinoco et al. 2020). Studies have therefore questioned the realism of these idealised representations. Lara et al. (2016) note that representing vegetation as cylindrical elements may not accurately capture the geometrical and mechanical properties of vegetation stems. Similarly, Ozeren et al. (2014) showed that arrays of rigid cylinders may not sufficiently reproduce the wave height dissipation induced by real plants.

2.4.1 Key parameters for wave attenuation by vegetation

Wave attenuation within vegetated environments results from momentum transfer between oscillatory wave motion and vegetation elements. Several vegetation and hydraulic parameters influence how waves are attenuated as they propagate through vegetated areas. These parameters have been identified across laboratory experiments, numerical modelling, and field studies as the most influential for quantifying vegetation–wave interactions. While many studies focus on coastal vegetation such as salt marshes and mangroves, recent work has also investigated wave attenuation in riparian forests, demonstrating that vegetation structure strongly influences hydraulic performance (van Wesenbeeck et al. 2022; Kalloe et al. 2022; van Starrenburg,

Mancheño, et al. 2026). The following parameters are some of the most important:

- **Frontal surface area:** The frontal surface area presented to incoming waves is a key determinant of drag and energy dissipation (Lightbody and Nepf 2006; van Wesenbeeck et al. 2022; Kalloe et al. 2022). In forested vegetation, frontal surface area is distributed vertically across stems, branches, and other vegetation elements. Different vegetation layers can interact with orbital velocities at different depths in the water column, thereby influencing wave energy dissipation (Ren et al. 2021). The vertical distribution of frontal surface area therefore represents an important parameter for describing vegetation–wave interactions in forested environments.

- **Drag coefficient (C_D):** The drag coefficient represents the resistance exerted by vegetation elements on oscillatory flow and therefore directly controls the magnitude of vegetation-induced wave dissipation. However, C_D remains an uncertain parameter and may vary with vegetation characteristics and hydrodynamic conditions. For example, Maza et al. (2015) found that the drag coefficient can change with vegetation density. Under oscillatory wave conditions, C_D is commonly related to the Keulegan–Carpenter number (KC), which describes the ratio between orbital excursion and vegetation diameter (Augustin et al. 2009; Jadhav et al. 2013; van Wesenbeeck et al. 2022). Reported values for rigid woody vegetation typically range between approximately 0.7 and 1.5 (**Sumer**).

- **Water depth vs. vegetation height:** The relative height of vegetation compared to the water depth strongly influences wave attenuation. Attenuation is generally greatest when vegetation is emergent and occupies the full water column (Foster-Martinez et al. 2018; Baker et al. 2022). When vegetation is submerged, the upper part of the water column, where orbital velocities are highest, remains partially unobstructed, resulting in reduced attenuation (Augustin et al. 2009). This highlights the importance of the vertical distribution of vegetation within the water column for vegetation–wave interactions (Tang et al. 2022; Ren et al. 2021).

- **Forest width:** The width of the vegetated belt strongly influences wave attenuation, as waves progressively dissipate energy while propagating through vegetation. Wave height reduction therefore generally increases with vegetation width (Quang Bao 2011; van Zelst et al. 2021). Recent modelling studies further show that wider forest belts not only increase wave attenuation but also reduce uncertainty in predicted wave reduction (Wesenbeeck et al. 2025). Consequently, forest width is an important parameter when assessing the flood protection potential of vegetated foreshores.

- **Density:** Vegetation density influences wave attenuation because a larger number of vegetation elements increases drag forces acting on the flow. Several experimental and modelling studies therefore identify vegetation density as one of the most influential parameters controlling wave attenuation (Zhang et al. 2021; Tang et al. 2022; Augustin et al. 2009). In riparian forests, stem density can vary strongly between stands, making forest density an important parameter when assessing wave attenuation in these environments (Karrenberg et al. 2002; Markus-Michalczyk and Michalczyk 2023).

- **Stem diameter:** Stem thickness directly affects both rigidity and frontal surface area, which influence the drag forces exerted on waves. The stem diameter provides a practical way to capture structural differences between younger stands with thinner stems and more mature forests with thicker trunks (Zhang et al. 2021; Kelty et al. 2022; van

Wesenbeeck et al. 2022). In riparian forests, stem diameter therefore represents an important structural parameter influencing vegetation–wave interactions.

- **Flexibility:** Vegetation flexibility influences how plants deform under wave forcing and therefore affects the effective drag exerted on the flow and the resulting wave attenuation. Flexible vegetation can bend or reconfigure under hydrodynamic forcing, which may reduce the effective resistance compared with rigid elements (van Veelen et al. 2021; Ren et al. 2021). In riparian forests, flexibility varies between species and plant components, with young stems and branches typically more flexible than mature woody trunks. These differences in plant mechanical properties may therefore influence wave attenuation between riparian forest types (van Starrenburg, Mancheño, et al. 2026).

In addition to woody vegetation elements, leaves may also contribute to vegetation drag. Several studies on vegetated flow resistance have shown that foliage can significantly increase drag in leafy conditions (Vogel 1996; Järvelä 2002; Järvelä 2004). However, under wave forcing, flexible leaves tend to bend and align with the flow, reducing their effective frontal area. As a result, the contribution of leaves to wave attenuation may be limited compared with woody vegetation elements (van Wesenbeeck et al. 2022). Furthermore, extreme hydraulic conditions in temperate regions often occur during winter when many riparian trees are leafless, further reducing the role of foliage in wave attenuation processes (Kalloe et al. 2022).

In biodiverse forests, vegetation characteristics such as frontal surface area, density, stem diameter, flexibility, and vertical distribution occur simultaneously and interact within the same stand. Riparian forests often contain mixtures of tall and short trees, flexible branches, dense patches, and open gaps, which together determine how vegetation interacts with waves under varying water levels and wave conditions. Consequently, vegetation parameters should be considered collectively when evaluating wave attenuation in structurally diverse floodplain forests.

2.5. LiDAR for forest structural analysis

Accurate quantification of tree structural parameters is essential for understanding how riparian vegetation influences wave attenuation through vegetated foreshores. Several remote sensing techniques have proven valuable for this purpose. Airborne LiDAR, for example, is widely used to characterise vegetation at stand and landscape scales. However, it is less suitable for resolving below-canopy elements such as understorey vegetation and trunk structure, because these components are often occluded by upper crown layers and dense canopies (Hilker et al. 2010). Moreover, first- and last-pulse airborne LiDAR data are generally insufficient to capture the full vertical complexity of vegetation, because intermediate canopy layers are often undersampled (Antonarakis, Richards, Brasington, and Bithell 2009).

In contrast, Terrestrial Laser Scanning (TLS) enables detailed assessment of forest geometry and can provide objective measurements of tree height, DBH and stem density. Compared with manual field measurements, which are often time-consuming and subject to observer interpretation, TLS offers a more systematic and spatially explicit approach (Hopkinson et al. 2003). In addition to capturing below-canopy vegetation elements, TLS enables detailed three-dimensional reconstruction of trees and canopies. It can capture high-resolution representations of tree form and obtain millions of points within relatively small forest stands, thereby providing rich three-dimensional information on forest architecture (Malhi et al. 2018; Antonarakis, Richards, Brasington, and Muller 2010).

2.5.1 What is TLS

TLS provides distance measurements to surrounding objects by emitting a large number of laser pulses within the instrument's field of view, which together form a three-dimensional (3D) point cloud representation of the scanned environment. When the laser beams interact with objects, part of the energy is reflected, transmitted, or absorbed. The relative proportions of these processes depend on the material properties of the object, its orientation relative to the laser beam, the incidence angle, and the travel path of the beam. Some materials reflect laser energy more efficiently than others, and different surface orientations also influence the strength of the returned signal. Additionally, the intensity of the return signal decreases with increasing distance, which affects the strength of the recorded return.

A single emitted pulse may produce multiple returns when it encounters different surfaces along its path, for example branches, leaves, and the ground. These returns can have different intensities and are recorded as separate points in the point cloud. Depending on the instrument configuration, scanners may record only the first return, the last return, or multiple intermediate returns (Béland, Widlowski, et al. 2011).

In addition to static terrestrial laser scanning, mobile or kinematic laser scanning systems have recently been developed for forest mapping. These systems often rely on Simultaneous Localization and Mapping (SLAM) algorithms to reconstruct three-dimensional forest environments while the sensor is moving. Although such systems enable faster data acquisition, the complex geometry of forests and occlusion between trees can reduce localization accuracy and mapping completeness compared with static TLS approaches (Shao et al. 2020).

There are two main approaches used by TLS instruments to estimate distances. The first is the Time-of-Flight (TOF) method. In this approach, discrete laser pulses are emitted and the travel time required for the pulse to reach an object and return to the scanner is measured. Using the known speed of light, this travel time is converted into a distance measurement. The second method is the Phase Shift (PS) method. Phase shift scanners emit a continuous modulated signal in which the frequency and amplitude are encoded. The phase difference between the emitted and received signal is then measured and translated into a distance estimate (Calders et al. 2020).

2.5.2 TLS measurement methods

In the single-scan method, the laser scanner is placed at a single location and only one scan is performed. This approach is the fastest, but it only captures the side of objects that is visible from the scanner position, meaning that parts of trees may remain unobserved in the point cloud. In the multi-scan method, several scans (generally three or four) are performed from different positions around the objects. The individual scans are subsequently merged into a single point cloud through geometric registration, typically using the known positions of reference targets that are visible from multiple scan locations. This method increases field measurement time and post-processing effort, depending on the number of scans and the method used to detect reference targets in the point cloud (e.g. automatic or manual detection). However, it generally provides a more complete three-dimensional representation of the scanned objects (Dassot et al. 2011). Because a single scan location may suffer from limited sampling and occlusion caused by foreground vegetation, a multi-scan setup can help to reduce these effects by capturing the objects from multiple viewing angles. Nevertheless, increasing the number of scans beyond three to five does not necessarily lead to substantial improvements in reconstruction accuracy (Torralba et al. 2022).

The laser beam incidence angle, defined as the angle between the emitted laser beam and the intercepted surface, influences both the probability of occlusion and the strength of

the returned signal. At larger incidence angles, reflections become weaker and the likelihood of missing returns increases, which can reduce the completeness of the recorded point cloud (Hosoi and Omasa 2006).

TLS instruments themselves also vary in their technical specifications, including the range-finding principle (phase shift or time-of-flight), laser wavelength, return type, measurement range, range accuracy, and beam divergence.

2.5.3 TLS data processing methods

To extract forest metrics from TLS data, various processing methods can be applied. Broadly, these methods can be divided into two categories. The first category includes structural reconstruction methods, which convert the point cloud into explicit 3D representations of vegetation structure. These representations enable the estimation of physical parameters such as tree height, DBH, or frontal surface area. The second category consists of beam–vegetation interaction methods, which do not reconstruct physical structures but instead analyze how laser beams interact with vegetation. These methods estimate the amount and distribution of plant material based on patterns of laser interceptions and gaps.

Complex meshing In surface meshing methods, the TLS point cloud is converted into a continuous surface representation using meshing algorithms such as Delaunay triangulation or Poisson surface reconstruction. These algorithms connect neighbouring points that likely belong to the same surface while avoiding connections across large gaps, thereby reconstructing realistic geometric structures. The resulting mesh consists of triangles that approximate the scanned surfaces. The area of these triangles can subsequently be calculated at different heights to derive vertical structural metrics such as the frontal surface area density $a(z)$ (Antonarakis, Richards, Brasington, and Bithell 2009). Meshing techniques are widely applied in forestry, for example to estimate leaf surface area (Yun et al. 2016) or stem volume using tetrahedral models (You et al. 2023).

Tree voxelization Voxelization converts the point cloud into a regular three-dimensional grid of small cubes called voxels, each representing a fixed volume of space. Points from the point cloud are assigned to the corresponding voxels, allowing vegetation structure to be analysed in a spatially consistent framework. This approach helps reduce the effects of uneven point density caused by occlusion or scanning geometry, as neighbouring points within the same voxel can still represent the local structure (Mathes et al. 2023). Voxel-based approaches enable several types of analysis:

1. Binary or continuous voxel values. Each voxel can store binary or continuous values describing vegetation presence or density. In the simplest case, voxels are assigned a value of 1 when containing points and 0 when empty, providing a basic three-dimensional representation of canopy structure (Stoker 2004; Antonarakis, Richards, Brasington, and Bithell 2009).

2. Contact frequency. Contact frequency quantifies vegetation density by counting the number of laser beam intersections within a voxel. Hosoi and Omasa (2006) define it as the mean number of contacts per beam insertion, while Béland, Widlowski, et al. (2011) describe it as the number of intersections per unit beam path length within the voxel. Higher contact frequencies indicate denser vegetation.

3. Ray tracing. Ray tracing simulates virtual laser beams passing through the voxelized canopy model. These beams interact with vegetation elements through absorption, reflection, scattering, or transmission, allowing the estimation of light propagation, canopy density, and vegetation distribution (Hosoi and Omasa 2006).

Geometric modelling Geometric modelling reconstructs tree architecture by fitting geometric primitives such as cylinders or tapered segments to the TLS point cloud. Quantitative Structure Models (QSMs) are a widely used example of this approach. QSMs represent trees as hierarchical collections of geometric elements approximating trunks and branches, enabling the estimation of structural parameters such as diameter at breast height (DBH), tree height, branch diameters, and woody volume (Malhi et al. 2018; Raumonen et al. 2015).

Several algorithms and modelling strategies have been developed for this purpose (Newnham et al. 2015), and open-source tools such as TreeQSM, SimpleTree, and alpha-shape methods have facilitated wider application of these techniques (Hackenberg et al. 2015).

Gap fraction Gap fraction describes the probability that a ray of light passes through the canopy without intercepting vegetation elements. Directional gap fraction refers specifically to the probability that a laser beam travelling in a given direction does not intersect canopy material (Danson et al. 2007). Two main approaches are used to estimate gap fraction from TLS data:

1. Pulse-based method. In this approach, directional gap fraction is calculated as the ratio between emitted laser pulses and detected returns within specific zenith angle bands and height intervals (Calders et al. 2020). TLS-derived gap fractions have been shown to produce results comparable to hemispherical photography while providing detailed three-dimensional information on canopy structure (Dassot et al. 2011; Jupp et al. 2009).

2. Voxel-based method. Gap fraction can also be estimated from voxelized canopy models using metrics such as contact frequency or ray tracing, which quantify beam–vegetation interactions within the voxel grid (Béland, Widlowski, et al. 2011).

Gap fraction can be related to structural vegetation indices such as Leaf Area Index (LAI) and Plant Area Index (PAI) through the Beer–Lambert law (Calders et al. 2020). These indices are ecologically important and can also be incorporated into hydrodynamic models, for example as inputs for vegetation resistance formulations in flow or wave attenuation simulations (Antonarakis, Richards, Brasington, and Bithell 2009).

For the present study, two relatively simple processing approaches are selected to estimate frontal surface area. A concave hull (alpha shape) approach applied to horizontal slices of the point cloud is used to capture internal gaps and crown irregularities, thereby providing a realistic representation of frontal surface area (Yan 2019; de Bruijn 2020; Kalloe et al. 2022). In addition, voxelization is applied by discretizing the point cloud into a three-dimensional grid, from which vegetation presence per voxel is used to estimate frontal surface area density (Antonarakis, Richards, Brasington, and Bithell 2009). More computationally intensive reconstruction methods do not necessarily lead to more accurate estimates of the frontal surface area relevant for wave attenuation, and may therefore not justify the additional effort for the large number of trees analysed in this study.

2.5.4 TLS limitations

TLS can provide detailed information about forest structure, but several limitations influence data acquisition and processing. High scanning resolutions or multiple scan positions produce large datasets, which increase both scanning time and post-processing requirements. Multi-scan approaches further require additional field time for placing reference targets and accurately registering scans. Consequently, a compromise is often necessary between data quality, field effort, and computational processing capacity, depending on the objectives of the study.

Occlusion is one of the main limitations in TLS measurements. Vegetation elements such

as lower branches, surrounding trees, and understorey vegetation can block laser beams and prevent parts of the vegetation from being recorded, resulting in lower point densities in occluded regions. Stand density also affects the extent of occlusion, as forests with closely spaced trees are more prone to beam blockage and therefore often require multiple scanning positions. In addition, the distance between the scanner and the tree influences which parts of the canopy are visible: scans taken close to the tree may cause occlusion of the upper canopy, whereas scans taken from greater distances can lead to occlusion of the lower trunk and understorey vegetation (Wilkes et al. 2017). Occlusion can also introduce bias in TLS-derived forest metrics. Vegetation density may be underestimated when parts of the canopy or smaller trees remain undetected, while DBH estimates may be biased towards larger trees if smaller individuals are not captured in the point cloud. Consequently, TLS can represent forest geometry in great detail, but ecological diversity metrics may remain incomplete unless multiple scan positions are combined (Boucher et al. 2021).

Leaf-on and leaf-off conditions also influence TLS data quality. The presence of foliage increases occlusion and reduces the penetration of laser beams into the canopy. This effect depends on the species. For example, beech forms dense canopies with foliage extending into the lower crown due to its high shade tolerance, whereas species such as spruce often lose needles in the lower canopy under dense stand conditions. As a result, laser beams may experience greater interception in species with dense foliage structures (Mathes et al. 2023). Consequently, scanning under leaf-off conditions can reduce occlusion and improve the visibility of woody vegetation elements.

Weather conditions can further affect TLS measurements. Wind can cause movement of branches and leaves, resulting in misaligned points and reduced structural accuracy. Rain and snow can intercept laser beams and introduce noise in the point cloud, while extreme temperatures can affect instrument performance. In addition, laser beams directed toward the sun may not return reliable signals, which can further increase noise in the data (Dassot et al. 2011). Noise in TLS data can compromise subsequent modelling and reconstruction processes. Many reconstruction and analysis methods rely on high-quality point clouds to accurately represent vegetation structure. Therefore, careful data acquisition and filtering are necessary to ensure reliable outputs from TLS processing workflows (Calders et al. 2020).

TLS processing methods also introduce methodological limitations. In voxel-based approaches, voxel size strongly influences the representation of vegetation structure. Voxels must be small enough to capture structural detail, but smaller voxel sizes increase computational requirements and model complexity (Béland, Baldocchi, et al. 2014). Larger voxels reduce computational demands and can smooth over gaps caused by occlusion, but this occurs at the expense of structural precision (Mathes et al. 2023). Similarly, meshing techniques can be sensitive to noise and missing data caused by occlusion, which may result in unrealistic or inaccurate surface reconstructions.

2.5.5 Quantifying vegetation parameters with TLS

TLS offers a more systematic and detailed approach for quantifying vegetation structure than traditional fieldwork. Jalonen et al. (2015) demonstrated that TLS can be used to derive frontal surface area from point clouds in the context of modelling floodplain flows, and Straatsma et al. (2008) applied frontal surface area metrics in Dutch floodplains to predict hydrodynamic vegetation density. TLS has the advantage that (1) it produces spatially explicit vegetation density maps, (2) it allows vegetation structure to be analysed in three dimensions, and (3) the spatial resolution of the analysis can be adjusted from individual branches and trees to entire stands depending on the research scale. Similarly, Kükenbrink et al. (2021)

showed that TLS can extract tree metrics such as DBH, crown dimensions, and vertical structure. TLS-based wood volume estimates have also shown strong potential for quantifying above-ground biomass (AGB), independent of species, size, or form. These capabilities make TLS particularly suitable for quantifying vegetation structural parameters relevant to wave attenuation, which are often too variable or complex to measure reliably using traditional field methods.

The vegetation structural parameters derived from TLS, such as vertically distributed frontal surface area density profiles $a(z)$, can subsequently be used as input for numerical wave attenuation models such as SWAN.

2.6. Wave attenuation modelling with SWAN

Wave attenuation by vegetation can be represented using a drag-based formulation, in which energy dissipation results from the work performed by wave orbital velocities on submerged vegetation, as described by the drag force component of the Morison equation (Morison et al. 1950). In this approach, dissipation is expressed as a function of vegetation structure and a bulk drag coefficient C_d, following the vegetation drag formulation originally proposed by Dalrymple et al. (1984) and later extended to spectral wave models by Mendez and Losada (2004). Subsequently, Suzuki et al. (2012) adapted this formulation to account for vertically varying vegetation structure through the frontal surface area density profile $a(z)$. This formulation is implemented in the phase-averaged spectral wave model SWAN (Simulating WAves Nearshore), which solves the spectral balance equation for wave action density to simulate wave propagation and transformation (Booij et al. 1999). Because SWAN is a phase-averaged model, only the cycle-averaged drag contribution to wave energy dissipation is represented. Inertia forces influence instantaneous hydrodynamic loading but perform no net work over a wave period and therefore do not contribute to wave height decay in the spectral balance equation. Using vertically distributed vegetation properties such as $a(z)$ allows structurally complex vegetation, such as floodplain forests, to be represented more realistically in numerical wave attenuation simulations.

2.7. Knowledge gap

Previous research has demonstrated that vegetated foreshores such as salt marshes, mangroves, and reed fields can significantly reduce wave loads on dikes by dissipating wave energy. These findings have established vegetation as a promising nature-based component of flood defence systems. Field observations and modelling studies confirm the importance of parameters such as vegetation density, vegetation height relative to water depth, plant flexibility, and frontal surface area in determining wave attenuation capacity. Terrestrial Laser scanning (TLS) has proven to be a powerful tool for quantifying these vegetation traits, offering detailed three-dimensional reconstructions of forest structure and capturing structural variability at multiple scales.

However, most studies to date have focused either on simplified vegetation representations (e.g., rigid cylinders), on coastal ecosystems such as salt marshes and mangrove belts, or on relatively uniform managed vegetation types such as pollarded willow stands. Consequently, the structural complexity of natural riparian floodplain forests has received far less attention. Riparian forests exhibit substantial variability in stem density, branching architecture, canopy layering, and vertical distribution of vegetation elements, yet this variability is rarely represented in wave attenuation models.

As a result, there remains limited understanding of how structural heterogeneity in natural floodplain forests influences wave attenuation along river dikes. In particular, the role of the

vertical distribution of frontal surface area and other key vegetation parameters in controlling wave attenuation under riverine conditions is not well quantified.

This study addresses this gap by quantifying the structural variability of diverse floodplain forests using TLS-derived vegetation metrics and evaluating how this variability influences wave attenuation in numerical simulations. By deriving vertical frontal surface area density profiles from TLS point clouds and incorporating these profiles into the spectral wave model SWAN, the study provides new insight into how structurally diverse riparian forests influence wave attenuation compared with simplified vegetation representations commonly used in wave models.

Estimating Wave Attenuation through Diverse Floodplain Forests in the Netherlands

Eliane A. van Boxtel, Su A. Kalloe, Roderik Lindenbergh & Bregje K. van Wesenbeeck

[1]Delft University of Technology
Faculty of Civil Engineering and Geosciences
Stevinweg 1, 2628 CN Delft, The Netherlands

Abstract. Vegetated foreshores are increasingly applied as nature-based flood defence measures, yet field evidence quantifying wave attenuation capacity of structurally diverse natural forests under flood conditions remains limited. Furthermore, complex vegetation structure is often overly simplified in spectral wave models. This study investigates how diverse floodplain forest structure governs wave attenuation and evaluates Terrestrial Laser Scanning (TLS) as a method for deriving vegetation structural parameters across contrasting forest stands.

The performance of TLS was evaluated using a reliability framework that defined the maximum distance over which vegetation structure could reliably be extracted from the point clouds. Within this reliable domain, frontal surface area profiles ($a(z)$) were reconstructed and implemented in the phase-averaged wave model SWAN to simulate wave attenuation under varying water levels and wave forcing. Attenuation was governed by the interaction between submerged vegetation structure ($a(z)\,C_d(z)$) and wave orbital velocities ($u(z)$), resulting in dissipation proportional to $a(z)\,C_d(z)\,u(z)^3$. Pioneer and managed stands were characterised by concentrated low vegetation structure, limited horizontal patchiness, and structurally similar trees. Under moderate inundation conditions (1.6–4.0 m water depth above the forest floor), these stands produced the strongest wave attenuation with the smallest range of outcomes, with a median of approximately 40% and an interquartile range of 25–55% for a forest width of 100 m. Late-successional stands, in contrast, were characterised by vertically distributed vegetation structure, pronounced horizontal patchiness, and structurally complex, diverse trees. Under the same conditions, these stands produced lower and more variable attenuation, with a median of approximately 20% and an interquartile range of 5–55%. These results indicate that vertical vegetation structure primarily controls the magnitude of wave attenuation, whereas horizontal patchiness governs the variability of attenuation within forest stands. However, attenuation varied across hydraulic conditions and vegetation types, indicating that wave attenuation is not a fixed property of forest structure.

Compared to overly simplified, vertically uniform vegetation representations, TLS-derived $a(z)$ profiles improved structural realism and captured depth-dependent attenuation behaviour. By linking high-resolution TLS-derived vegetation structure to wave modelling, this study provides a quantitative framework for evaluating structurally diverse floodplain forests as nature-based flood defences.

Keywords: Wave attenuation, Riparian floodplain forests, Frontal surface area density, Terrestrial Laser Scanning (TLS), Spectral wave modelling.

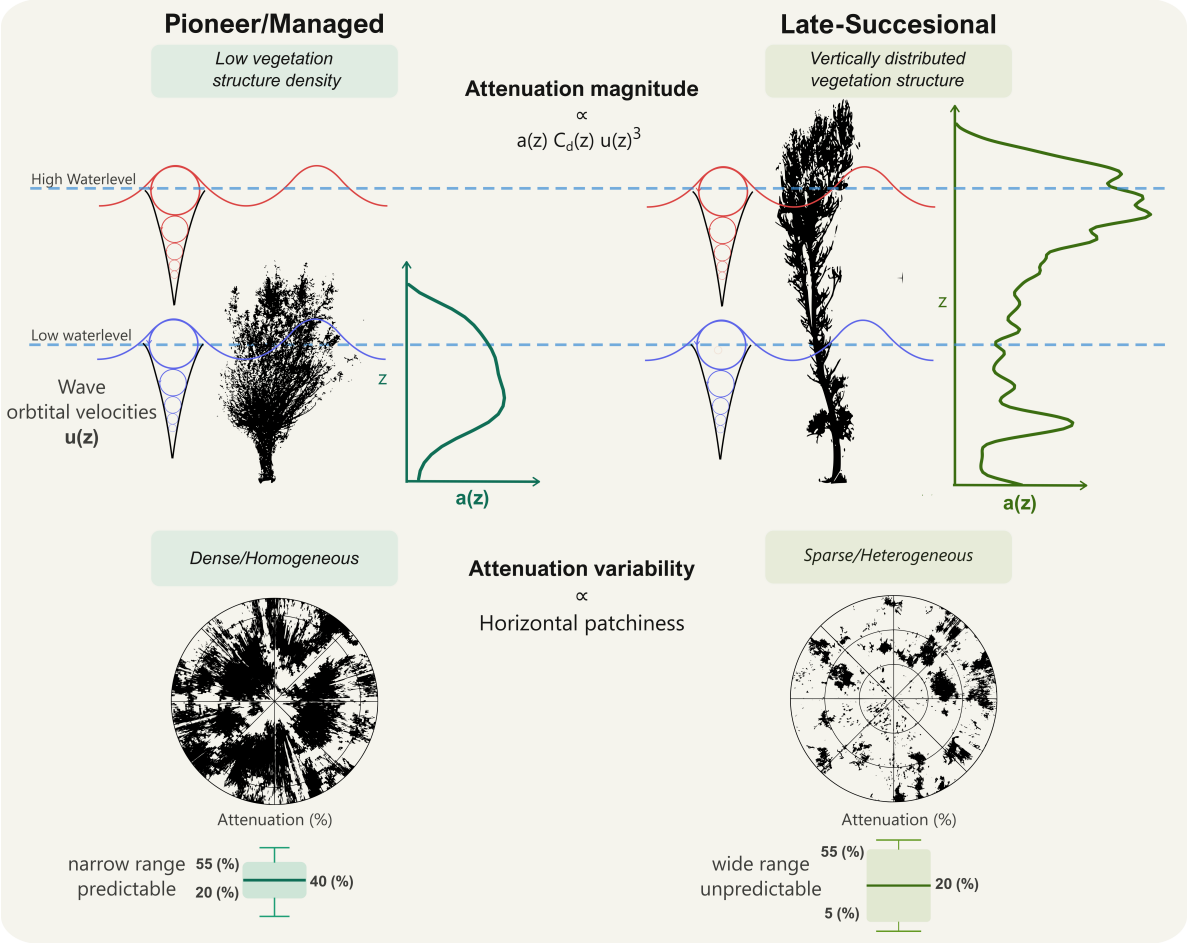

Figure 1: Graphical abstract illustrating the influence of vertical vegetation structure and horizontal patchiness on wave attenuation magnitude and variability.

1. Introduction

Increasing flood risk driven by climate change and socio-economic development places growing pressure on flood defence systems worldwide. Climate change is expected to alter river flow regimes across Europe, affecting the magnitude, timing, and variability of discharge, with implications for flood risk and ecosystem functioning (Schneider et al. 2013). In low-lying delta regions such as the Netherlands, where around 55% of the land is flood-prone from rivers and the sea (Eijgenraam et al. 2014), maintaining safety standards requires continuous dike reinforcement. Meanwhile, population growth and economic development further increase the potential consequences of flooding and associated long-term costs (Jongman 2018; S. Jonkman et al. 2013). Yet conventional engineering faces growing spatial, environmental, and financial constraints, driving increasing interest in nature-based solutions (NbS) that combine hydraulic safety with ecological and societal benefits (Van Wesenbeeck et al. 2017; Vuik, S. N. Jonkman, et al. 2016; Temmerman, Meire, et al. 2013).

Vegetated foreshores are increasingly recognised as nature-based flood defences because vegetation attenuates waves and currents through drag-induced energy dissipation. Numerous studies have demonstrated the reduction of hydraulic loading on coastal infrastructure in coastal ecosystems such as mangrove forests and salt marshes (Vuik, Borsje, et al. 2019; Gijsman et al. 2021; Temmerman, Horstman, et al. 2023; Möller et al. 2014; Van Loon-Steensma and Kok 2016; Penning et al. 2016). However, the role of riparian vegetation in riverine en-

vironments remains poorly characterised. Recent studies have begun to investigate the flood protection potential of willow forests through flume experiments and field-based analyses, demonstrating that willow forests can contribute to wave attenuation and reduce hydraulic loading on dikes (van Starrenburg, Mancheño, et al. 2026; van Wesenbeeck et al. 2022; Kalloe et al. 2022; Ren et al. 2021). However, most existing studies focus on specific managed stand types, such as pollarded or planted willows. Yet riparian forest structure varies substantially depending on local environmental conditions, species composition, and management practices (Karrenberg et al. 2002; Markus-Michalczyk and Michalczyk 2023). Riparian floodplain forests develop under dynamic hydrological conditions and therefore exhibit large variation in stem density, flexibility, and branching architecture (Markus-Michalczyk and Michalczyk 2023; Markus-Michalczyk and Hanelt 2019). These characteristics directly control vegetation–flow interactions by influencing drag forces and frontal surface area (Tinoco et al. 2020). Consequently, the hydraulic performance of riparian forests is likely to differ between locations and stand types (Augustin et al. 2009; Tang et al. 2022). Despite this structural complexity, vegetation structure in wave models is commonly assumed to be constant in space or roughly divided into coarse vertical layers, rather than capturing the full structural variation of real forest stands, as represented in Figure 2 (Kalloe et al. 2022; Suzuki et al. 2012). While these approaches provide first-order estimates of vegetation-induced wave attenuation, they neglect the structural heterogeneity of natural forests, leading to inaccurate predictions (Tinoco et al. 2020).

Detailed structural data for natural riparian floodplain forests remain scarce, limiting the ability to realistically represent vegetation structure in numerical wave models. Terrestrial Laser Scanning (TLS) can provide detailed representation of vegetation structure through high-resolution measurements of forest geometry. TLS allows structural metrics such as frontal surface area distributions to be derived and incorporated more realistically into hydrodynamic models (Straatsma et al. 2008; Jalonen et al. 2015; Antonarakis, Richards, Brasington, and Muller 2010; Malhi et al. 2018; Dunlop et al. 2025). However, TLS measurements in dense riparian forests are affected by occlusion and distance-dependent reductions in point density, which can introduce bias in derived structural metrics (Dassot et al. 2011; Wilkes et al. 2017). Therefore, the reliability of TLS-derived structural profiles is a key methodological consideration that this study addresses before applying them in wave modelling.

This study investigates how structural complexity of riparian floodplain forests influences wave attenuation. It will be analyzed how structurally diverse natural forests differ in hydraulic performance from managed forests, such as pollarded willow stands, and from overly simplified vegetation representations commonly used in wave attenuation models (Figure 2). A TLS-based workflow is developed to derive frontal surface area profiles from point cloud data collected in contrasting floodplain forests in the Netherlands, which are subsequently incorporated into the spectral wave model SWAN. The central research question is: how does variation in vertical vegetation structure influence wave attenuation in diverse riparian forests along Dutch floodplains? Specifically, this study aims to: (1) derive high-resolution vegetation structural profiles from TLS point cloud data for natural and managed riparian stands; (2) assess the reliability of TLS-derived frontal surface area profiles subject to occlusion and variable point density; and (3) quantify the sensitivity of wave attenuation to structural differences between stand types and relative to overly simplified parameterisations.

Figure 2: Conceptual comparison between overly simplified vegetation representations commonly used in wave attenuation modelling, and TLS-derived vegetation structure.

2. Materials and methods

2.1. Study Area

This study was conducted in two riparian forests along contrasting Dutch river systems. The sites were selected to represent distinct forest structures and associated riparian vegetation types, as summarised in Table 1. At both sites, vegetation structure was quantified using a combination of manual field measurements and TLS. Measurements were conducted in eight plots at the Visserijgrienden and six plots at the Millingerwaard (Figure 3B-C).

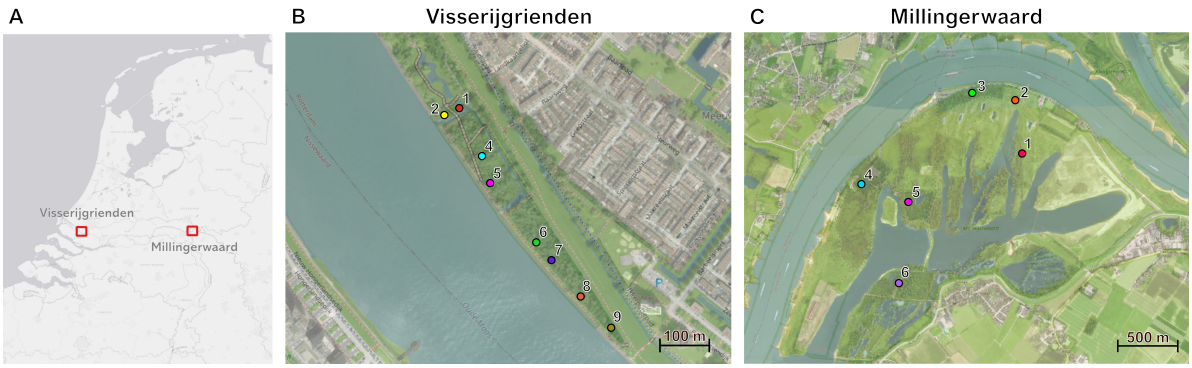

Figure 3: Study area overview. (A) National overview showing the locations of Visserijgrienden (Rhine–Meuse delta) and Millingerwaard (Waal River). Site maps with field-measurement locations for (B) Visserijgrienden and (C) Millingerwaard.

Table 1: Hydrodynamic contrast between the two study sites.

Characteristic	Visserijgrienden	Millingerwaard
River system	Rhine–Meuse delta (Oude Maas)	Rhine distributary (Waal)
Flow regime	Tidal (freshwater)	Discharge-dominated
Dominant driver	Semi-diurnal tide	Upstream Rhine discharge
Water-level variability	∼1.6 m daily range	Event-driven rise
Flood frequency	High (daily)	Low (seasonal/events)
Flood duration	Short (tidal cycles)	Multi-day to multi-week
Flow direction	Bidirectional	Unidirectional
Forest type	Softwood-dominated	Mixed softwood–hardwood

2.1.1 Visserijgrienden

The Visserijgrienden is a riparian wetland located along the Oude Maas near Hoogvliet in South-Holland, within the Rhine–Meuse delta. The site forms part of the Natura 2000 network, covering approximately 2 ha. Due to its deltaic position, the Oude Maas experiences semi-diurnal freshwater tidal fluctuations with a mean tidal range of approximately 1.6 m (Reker et al. 2007). The forest floor lies at approximately +1.0 m NAP, corresponding to about 0.4 m above the mean water level (+0.6 m NAP) of the tidal Oude Maas (Rijkswaterstaat 2026; Actueel Hoogtebestand Nederland 2019). Consequently, the forest is subject to semi-diurnal, short-duration inundation events. During periods of elevated Rhine discharge, water levels may rise further, temporarily increasing inundation depth and duration beyond the regular tidal cycle. Historically, the area was managed for willow coppicing. During the twentieth century, active management declined, allowing the coppiced stands to develop into a mature willow-dominated forest characterised by complex multi-stem and branching architectures (Reker et al. 2007). Present forest structure reflects the combined influence of historical coppicing, natural succession, and tidal hydrodynamics. The site currently contains both actively managed pollarded willow stands and more naturally developed willow forest, resulting in a structurally heterogeneous but willow-dominated forest. The diversity of willow growth forms present at the Visserijgrienden is illustrated in Figure 4.

2.1.2 Millingerwaard

The Millingerwaard is a riparian floodplain located along the Waal River near Nijmegen in the eastern Netherlands, within the downstream Rhine distributary system. The site forms part of the Natura 2000 network (Ministry of Agriculture, Nature and Food Quality 2007). Consisting of approximately 400 ha of mixed riparian forest, pools and grasslands, the area supports a diverse range of plant and animal species (Bulkens et al. 2016). In contrast to the tidal regime at the Visserijgrienden, the hydrodynamics here are fluvially dominated and primarily governed by upstream Rhine discharge variability. Water levels respond to seasonal and event-based discharge fluctuations, resulting in lower-frequency, longer-duration floodplain inundation during high-flow events compared to the Visserijgrienden. The forest floor elevations range between +9.5 and +14.5 m NAP, placing the forest approximately 0.5–5.5 m above the mean water level (+9 m NAP) of the Waal River (Rijkswaterstaat 2026; Actueel Hoogtebestand Nederland 2019). Historically, the Millingerwaard was used for agriculture and clay extraction. Since the early 1990s, the area has undergone large-scale restoration and nature development, re-establishing natural geomorphological dynamics (Bulkens et al.

2016). Sediment deposition, erosion, and grazing now interact to shape vegetation patterns and drive successional dynamics. The vegetation is dominated by willow structures (*Salix spp.*), with additional sub-forest types comprising oak (*Quercus spp.*), elm (*Ulmus spp.*), ash (*Fraxinus excelsior*), alder (*Alnus spp.*) and beech (*Fagus sylvatica*), alongside thorny shrub structures. Stands are spatially heterogeneous, reflecting variation in elevation, flood exposure, and successional stage, resulting in a structurally and compositionally diverse riparian forest (Figure 4).

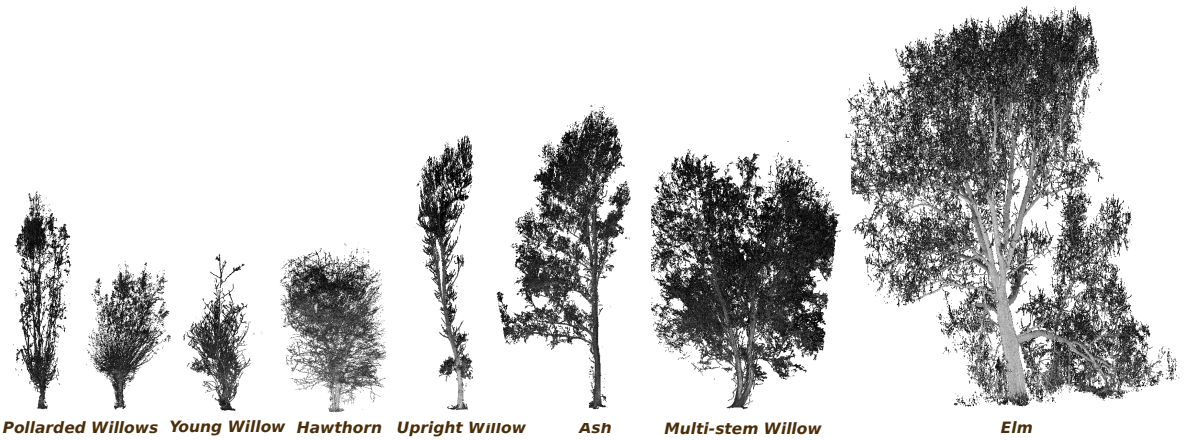

Figure 4: Trees extracted from TLS point clouds, representative of the structural diversity encountered across both study sites.

2.2. Field Measurements and TLS Data Acquisition

Vegetation structure at the Visserijgrienden and Millingerwaard sites was quantified through an integrated approach combining manual field measurements with TLS. TLS surveys were conducted using a Leica P40 static terrestrial laser scanner, positioned at a single scan location at the centre of each circular plot (Figure 5A) and mounted at 1.5 m above ground level. Full-dome scans were acquired spanning a 360° horizontal and 290° vertical field of view at a spatial resolution of 3.1 mm at 10 m distance, yielding high-density point clouds suitable for the extraction of fine-scale vegetation structural metrics. Within each plot, a series of 1×1 m subplots were systematically distributed (Figure 5A), within which vegetation characteristics and species composition were recorded. Nearest-neighbour distances (NND) between trees were measured to characterise local tree spacing patterns.

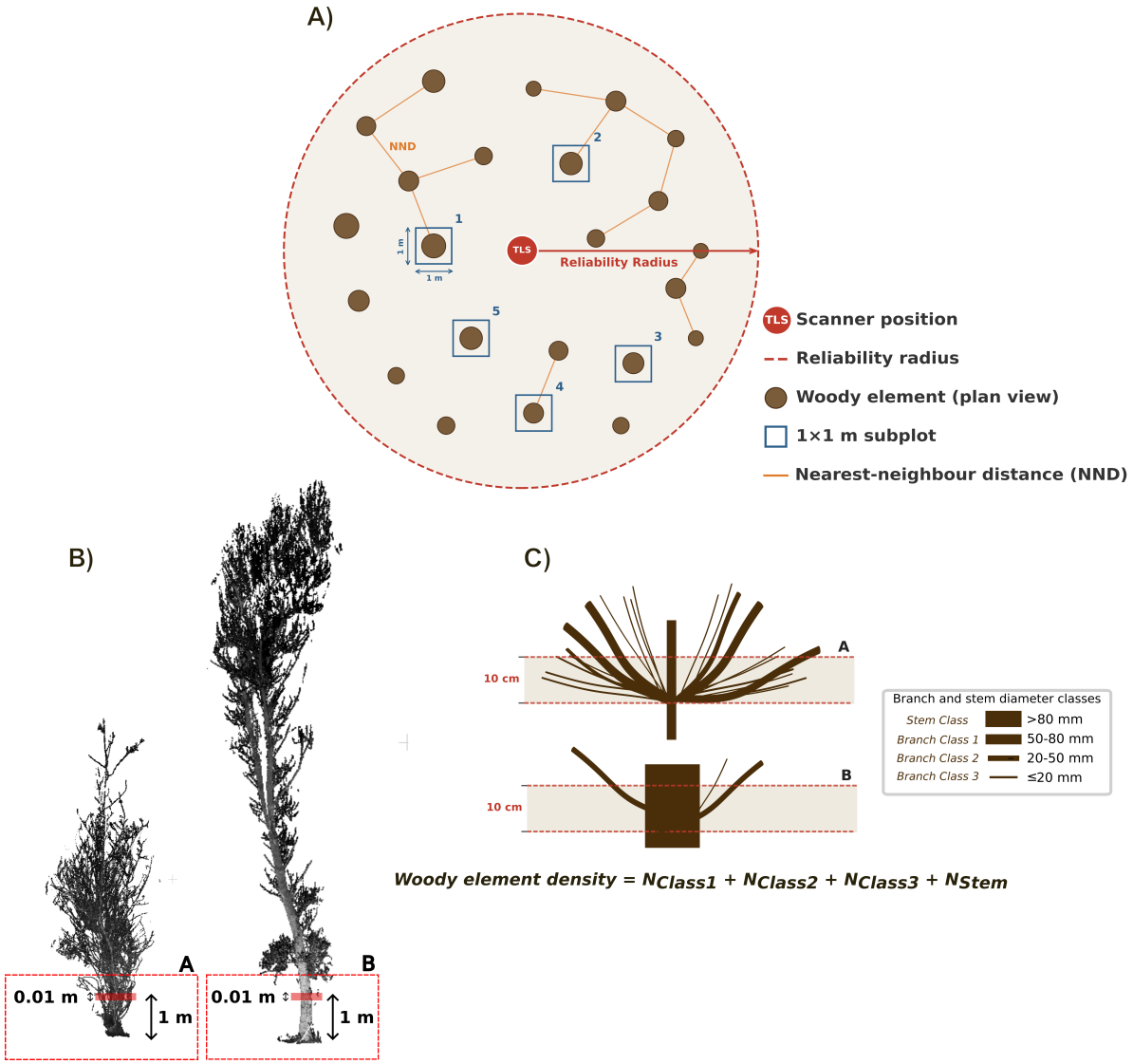

Figure 5: Field-based vegetation structure assessment used to validate TLS-derived structural metrics. (A) TLS scanner position and GPS-referenced layout of 1 × 1 m subplots within a circular plot, with NND recorded between trees. (B) Example of two contrasting TLS-extracted vegetation structures and the extraction of a 10 cm vertical slice at 1.0 m height. (C) Classification of woody elements within the 10 cm slice into stem and branch diameter classes used to derive FSA_{stem}, FSA_{branch}, and the Branchiness Index R.

2.2.1 Hand Measurements

Within each subplot, species identity, woody element density, and stem and branch diameter classes were recorded at 1.0 m above ground level. Woody elements exceeding 80 mm in diameter were classified as stems (Figure 5C), and their diameters were measured. Branch structure was quantified by counting all branches intersecting the subplot and assigning each to one of three diameter classes ($\leq$ 20 mm, 20–50 mm, and 50–80 mm). These classes were based on the study of Kalloe et al. (2022). For each diameter class, a representative branch diameter was measured within the subplot.

GPS coordinates of each subplot centre were recorded to enable spatial alignment with the TLS point cloud. This allowed extraction of a corresponding 10 cm vertical slice at 1.0 m

height from the TLS scan (Figure 5B), enabling direct comparison between field measurements and their TLS-derived counterparts at equivalent locations and heights.

2.3. Forest Structure Characteristics

2.3.1 Woody Element Density

Woody element density was defined as the total number of woody elements intersecting the subplot within a 10 cm vertical slice centred at 1.0 m above ground level (Figure 5C). Woody elements include both stems and branches belonging to the three branch diameter classes.

$$N_{\text{woody}} = N_{\text{stem}} + N_{\text{class1}} + N_{\text{class2}} + N_{\text{class3}} \tag{1}$$

where N_{stem} denotes the number of stems intersecting the slice, and N_{class1}, N_{class2}, and N_{class3} represent the number of branches belonging to the three diameter classes. The resulting value represents the local density of woody elements within the subplot and serves as a structural descriptor of vegetation complexity.

2.3.2 Frontal Surface Area

Frontal surface area (FSA) represents the projected area of woody elements intersecting a vertical plane (Figure 5B-C). Stem-specific frontal surface area was calculated according to Equation 2:

$$FSA_{\text{stem}} = \sum_{i=1}^{n} D_i \cdot h \tag{2}$$

Where D_i denotes the diameter of stem i, n the total number of stems within the subplot, and h the vertical slice thickness. Branch frontal surface area was calculated according to Equation 3:

$$FSA_{\text{branch}} = \sum_{c=1}^{3} N_c \cdot D_c \cdot h \tag{3}$$

Where N_c is the count of branches assigned to diameter class c, and D_c the representative diameter for that class.

2.3.3 Structural Complexity Characterisation

To characterise the complexity of forest stands, a Branchiness Index R (Equation 4) is introduced. Which computes the fractional contribution of branch frontal surface area to total woody frontal surface area at 1 m height at the subplot scale:

$$R = \frac{FSA_{\text{branch}}}{FSA_{\text{stem}} + FSA_{\text{branch}}} \tag{4}$$

Values of R range from 0 to 1, where values approaching 0 indicate stem-dominated structure and values approaching 1 indicate branch-dominated structure.

2.3.4 Nearest-Neighbour Distance

NND served as a measure of local tree spacing within each TLS plot. For each recorded tree, the distance to its closest neighbour was computed from GPS coordinates (Figure 5A). Lower NND values indicate denser tree spacing, whereas higher values reflect more open stands.

2.3.5 Forest Density

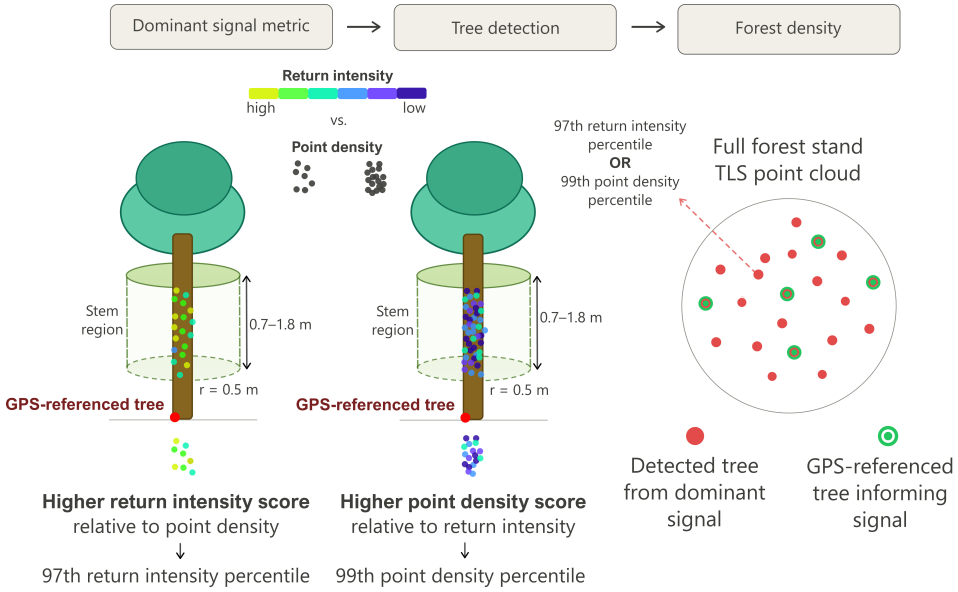

Figure 6: Conceptual workflow for forest density estimation from TLS point clouds. Cylindrical search volumes centred on GPS-referenced trees are used to evaluate two potential signal metrics: return intensity and point density. The metric providing the strongest discrimination between woody elements and surrounding vegetation is selected as the dominant signal metric for tree detection.

Forest density was quantified by classifying TLS points as trees using signal characteristics extracted from cylindrical search volumes centred on GPS-referenced trees (Figure 6). For each GPS point, a cylindrical search volume was defined with a horizontal radius of 0.50 m, following Boucher et al. (2021), to account for the combined effects of GPS positional uncertainty, TLS ranging error, and stem radius. The vertical extent was constrained to 0.7–1.8 m above ground level, isolating the stem region around breast height (DBH $\approx$ 1.3 m) and minimising interference from understory vegetation and foliage (Wardius and Hein 2024).

Within each search volume, two signal metrics were computed: point density and return intensity. This follows a signal detection approach in which point density and return intensity are evaluated to distinguish woody elements from surrounding canopy elements (Tan et al. 2021). For each forest stand, the discriminatory strength of both metrics was evaluated, and the metric yielding the higher support score was selected as the basis for tree detection.

Point density support was quantified from the rate of exponential decay in point density with increasing scanner distance, reflecting occlusion and reduced sampling density with distance from the scanner (Torralba et al. 2022; Lang et al. 2021). Intensity support was quantified from the strength and continuity of the signal, as woody material typically produces a stronger and more consistent return than foliage (Danson et al. 2007; Olsoy et al. 2014).

Where return intensity was the dominant signal, trees were identified using a global 97th percentile intensity threshold applied across the scan. Where point density was the dominant signal, detection was based on the 99th percentile of point density calculated in 2 m radial intervals, accounting for the distance-dependent decline in point sampling density. Detection performance was evaluated by comparing TLS-classified trees with GPS-referenced trees, enabling assessment of classification reliability.

2.4. TLS Reliability Assessment

The reliability of each TLS scan was assessed independently to determine a scan-specific maximum reliability distance. This step was necessary because TLS-derived structural metrics, including forest density and frontal surface area, serve as direct inputs to the SWAN wave attenuation model, meaning that unreliable observations could propagate into wave attenuation estimates. The reliability analyses ensured that structural variability between plots was captured in the scan-specific reliability distances, while retaining the full usable range of each scan for subsequent analyses.

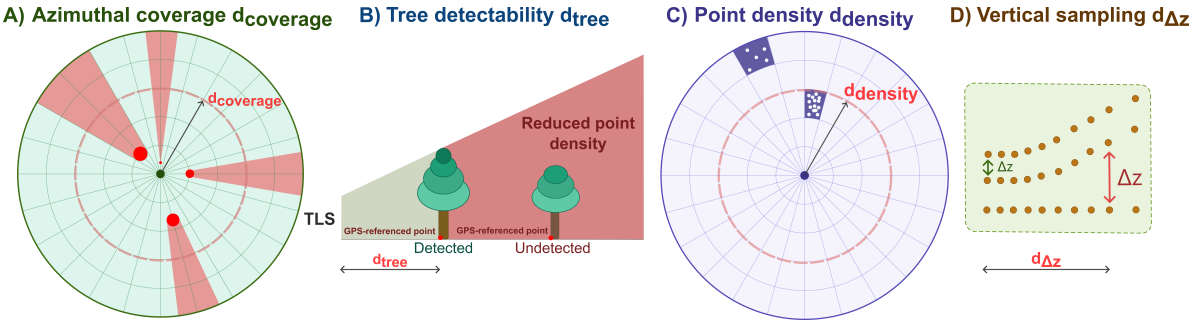

Figure 7: The four TLS reliability criteria used to define the scan-specific reliability distance threshold d_{reliable}: azimuthal coverage d_{coverage}, GPS-referenced tree detectability d_{tree}, point density d_{density}, and vertical sampling adequacy $d_{\Delta z}$. The final reliability distance is taken as the minimum across all four criteria.

2.4.1 Definition of the Reliability Distance

Four criteria were used to define the scan-specific reliability distance d_{reliable}: GPS-referenced tree detectability, azimuthal coverage, point density, and vertical sampling adequacy (Figure 7). The final reliability distance for each scan was defined as the most restrictive distance across all four criteria:

$$d_{\text{reliable}} = \min\left(d_{\text{tree}}, d_{\text{density}}, d_{\text{coverage}}, d_{\Delta z}\right) \tag{5}$$

This threshold defines the maximum distance used to derive structural metrics in each scan, which serve as input to the SWAN wave attenuation model.

2.4.2 GPS-Referenced Tree Detectability

GPS-referenced tree locations were used to evaluate whether the TLS scan captured sufficient returns at known tree positions as a function of scanner distance (Figure 7B). Point density was computed within the cylindrical search volumes defined in Section 2.3.5, and detection was defined as a binary variable:

$$\delta_i(d) = \begin{cases} 1 & \text{if } P_i(d) \geq 10{,}000 \text{ pts/m}^2 \\ 0 & \text{otherwise} \end{cases} \tag{6}$$

Where $P_i(d)$ is the point density within the search volume around GPS-referenced trees i at scanner distance d. The 10,000 pts/m^2 threshold corresponds to an approximate point spacing of 1 cm, identified by Zhao et al. (2023) and Calders et al. (2020) as sufficient for resolving fine-scale woody structure.

The reliability distance d_{tree} was defined as the distance at which the first GPS-referenced tree fell below the detection threshold:

$$d_{\text{tree}} = \max\left\{d \;\middle|\; \delta_i(d) = 1\right\} \tag{7}$$

This distance was interpreted as the onset of unreliable tree detectability with increasing scanner distance due to occlusion and decreasing point density in the TLS scan.

2.4.3 Point Density

Point density was evaluated as a function of scanner distance to assess spatial sampling quality (Figure 7C). The point cloud was subdivided into radial bins of 0.1 m width and azimuthal sectors of 1° resolution ($\Delta r = 0.1$ m, $\Delta\theta = 1°$). Point density within each sector was defined as the number of points divided by the corresponding sector area, accounting for geometric expansion and beam divergence with increasing distance from the scanner (Wilkes et al. 2017).

For each radial bin, the median point density was computed across occupied sectors only ($N > 0$), excluding empty sectors attributable to the absence of vegetation rather than insufficient sampling (Soma et al. 2020). The reliability distance d_{density} was defined as the maximum distance at which the median point density of occupied sectors remained above the 10,000 pts/m^2 threshold defined in Section 2.4.2. This can be expressed as:

$$d_{\text{density}} = \max\left\{d \;\middle|\; \tilde{D}(d) \geq 10{,}000 \text{ pts/m}^2\right\} \tag{8}$$

Where $\tilde{D}(d)$ is the median point density of occupied azimuthal sectors at radial distance d.

2.4.4 Azimuthal Coverage

Azimuthal coverage was defined as the fraction of occupied azimuthal sectors within each radial ring (Figure 7A), calculated as the number of sectors containing at least one return divided by the total number of sectors. This metric identifies directional gaps caused by structural occlusion (Lang et al. 2021; Boucher et al. 2021).

Azimuthal coverage was evaluated using the full point cloud, as the ground surface provides a continuous reference and the absence of ground returns therefore indicates occlusion by vegetation.

The reliability distance d_{coverage} was defined as the maximum distance at which azimuthal coverage remained ≥ 0.9:

$$d_{\text{coverage}} = \max\left\{d \;\middle|\; C(d) \geq 0.9\right\} \tag{9}$$

Where $C(d)$ is the fraction of occupied azimuthal sectors at radial distance d. A coverage below 0.9 indicates that more than 10% of azimuthal sectors lack returns, reflecting substantial occlusion and reduced representativeness of the surrounding vegetation (Boucher et al. 2021).

2.4.5 Vertical Sampling Adequacy

Local vertical sampling adequacy was evaluated using fixed 5×5 cm horizontal bins. Within each bin, inter-point height differences (Δz) were computed as the vertical distance between successive z-coordinates after sorting points by elevation, providing a measure of local vertical resolution within the TLS sampling of vegetation elements (Figure 7D). This fixed binning approach avoids artificial inflation of Δz that arises in the radial–azimuthal framework, where

sector area increases with distance and may encompass multiple neighbouring vegetation elements (Wilkes et al. 2017).

At each radial distance, the 50th and 90th percentiles of Δz were computed across all 5×5 cm bins. Variability in vertical point spacing was quantified as:

$$\Delta z_{90-50}(d) = \Delta z_{90}(d) - \Delta z_{50}(d) \tag{10}$$

Where $\Delta z_{90-50}(r)$ represents the spread between median and upper-range vertical point spacing at distance d.

The reliability distance $d_{\Delta z}$ was defined as the maximum distance at which Δz_{90-50} remained ≤ 0.03 m:

$$d_{\Delta z} = \max \left\{ d \;\middle|\; \Delta z_{90-50}(d) \leq 0.03 \text{ m} \right\} \tag{11}$$

The 0.03 m threshold corresponds to the point spacing identified by Wilkes et al. (2017) as sufficient to resolve fine woody branches in complex canopy structures.

2.5. Frontal Surface Area Extraction and Vertical Profile Derivation

Frontal surface area (FSA) was reconstructed from TLS point clouds within the scan-specific reliability distance to derive vegetation inputs for the SWAN wave attenuation model. Two geometric reconstruction approaches were evaluated and validated against field-measured frontal surface area. $a(z)$ profiles were derived at the stand, subplot, and individual tree scale using the validated reconstruction method.

2.5.1 Alpha-Shape and Voxel-Based Methods

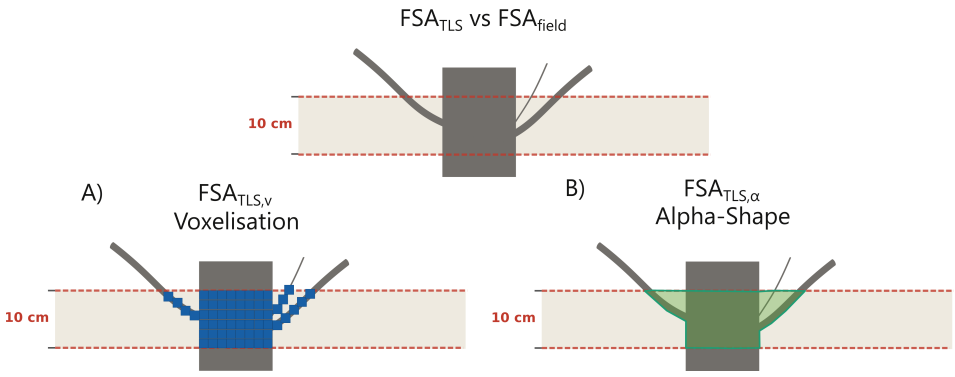

Figure 8: Frontal surface area estimation from TLS point clouds. Field frontal surface area (FSA_{field}) was measured within a 10 cm vertical slice. The corresponding slice was extracted from the GPS-referenced tree in the TLS point cloud and reconstructed using (A) voxelisation and (B) the alpha-shape approach to obtain FSA_{TLS}.

Frontal surface area was estimated using two geometric reconstruction approaches: the voxelisation method (Figure 8A) and the alpha-shape method Figure (8B). For both methods, point clouds were projected onto a vertical plane, with the projection direction selected to maximize the frontal surface area, consistent with the field measurements.

For the alpha-shape approach, a two-dimensional alpha-shape (concave hull) was fitted to the projected points. The parameter α controls the concavity of the boundary polygon, with lower values producing tighter fits to the point distribution.

The voxel-based method discretized the projected point cloud into cubic voxels of edge length v. Voxels containing at least one point were considered occupied, and frontal surface area was derived from the total projected area of the occupied voxels.

Both methods were applied to the GPS-referenced trees for which field measurements were available, using the same height range and spatial extent as used in the field measurements.

2.5.2 Validation

The alpha-shape parameter (α) and voxel size (v) were systematically varied to identify the parameter setting minimizing the median absolute error (MAE) between the TLS-derived and field-measured frontal surface area:

$$MAE = \text{median}\left(|FSA_{TLS} - FSA_{field}|\right) \tag{12}$$

Method performance was evaluated through 1:1 comparisons between TLS-derived and field-measured FSA, using median bias, regression slope relative to the 1:1 line, and the coefficient of determination (R^2).

The analysis was first conducted using all available validation trees, then repeated constrained to the reliability distance to assess the sensitivity of the error metrics. The optimal reconstruction method and parameter setting were selected by minimizing MAE and the deviation of the regression slope from unity.

2.5.3 Stand-Level $a(z)$ Profile – Radial Band Method

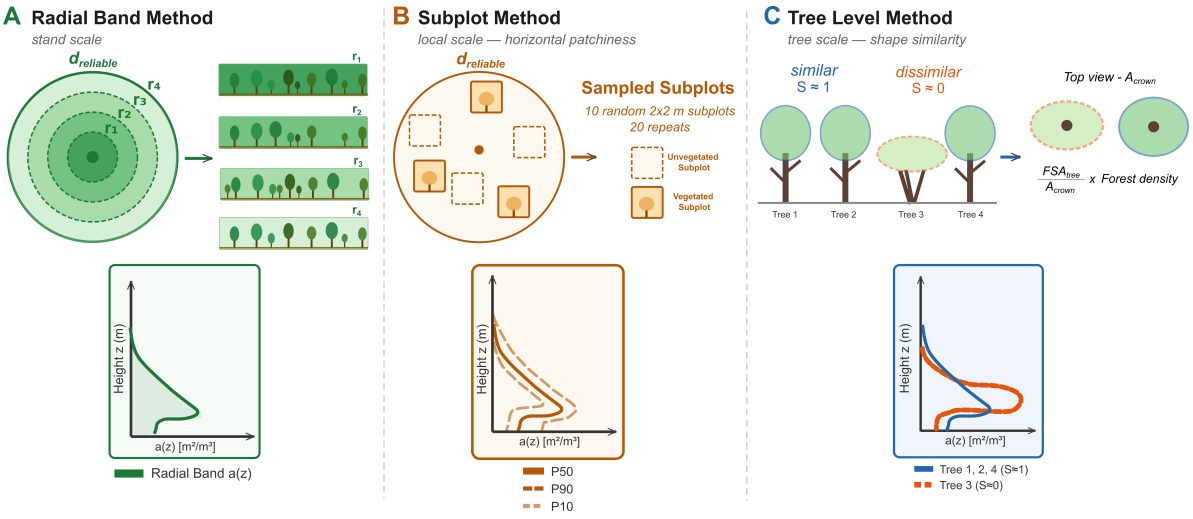

Figure 9: Overview of the three TLS-based approaches used to derive vertical frontal surface area density profiles $a(z)$ at different spatial scales within the reliability distance. (A) Radial band method (stand scale), where the TLS scan domain is subdivided into concentric radial bands to reconstruct a stand-level $a(z)$ profile. (B) Subplot method (local scale), where multiple randomly sampled 2×2 m subplots are extracted to characterise horizontal patchiness and derive percentile $a(z)$ profiles (P10, P50, P90). (C) Tree-level method (tree scale), where individual trees are isolated to derive tree-specific $a(z)$ profiles and evaluate vertical shape similarity. Tree-level profiles are normalised by crown area (A_{crown}) and scaled by forest density to enable comparison with stand-level profiles.

Following the selection of the optimal reconstruction method and parameters, $a(z)$ profiles were derived for each TLS scan. Ground points were removed prior to analysis. The

circular scan domain, extending from the scanner to the scan-specific reliability distance, was subdivided into concentric radial bands of 1 m width to reduce underestimation caused by occlusion from foreground vegetation (Figure 9A). For each radial band r, frontal surface area was computed in vertical increments of $\Delta z = 0.25$ m. Contributions from all bands were summed per height layer:

$$FSA_{\text{layer}}(z) = \sum_{r=1}^{N} FSA_r(z) \tag{13}$$

Where $FSA_r(z)$ is the frontal surface area in radial band r at height z, and N is the total number of bands within the reliability distance. Normalising by ground area and layer thickness yielded the vertical frontal surface area density profile:

$$a(z) = \frac{FSA_{\text{layer}}(z)}{A_{\text{ground}}\Delta z} \tag{14}$$

where A_{ground} is the circular ground area within the reliability distance. The resulting $a(z)$ profile served as the stand-level vegetation input for SWAN.

2.5.4 Subplot-Level $a(z)$ Profiles

To characterise within-stand structural variability, vertical frontal surface area density profiles were derived from randomly sampled subplots. In each sampling repeat, 10 non-overlapping square subplots of 2×2 m were placed randomly within the reliability distance. This procedure was repeated 20 times, yielding up to 200 subplot realizations per scan (Figure 9B). For each subplot, TLS points were extracted and FSA was computed in vertical increments of $\Delta z = 0.25$ m. The resulting subplot profiles $a_i(z)$ were aligned to the lowest detected point within each subplot and pooled across all samples. The 10th, median, and 90th percentile profiles were then computed per height level:

$$a_{P_k}(z) = P_k\left(\{a_i(z)\}_{i=1}^{N}\right), \quad k \in \{10, 50, 90\} \tag{15}$$

The resulting $a_{\text{P10}}(z)$, $a_{\text{P50}}(z)$, and $a_{\text{P90}}(z)$ profiles represent sparse, median, and dense vegetation conditions within the forest stand, and were used alongside the radial band profile as alternative $a(z)$ inputs for SWAN.

2.5.5 Tree-Level $a(z)$ Profiles

To verify the physical plausibility of the selected reconstruction parameters, $a(z)$ profiles were derived for 5 individual trees per forest stand. For each tree, TLS points were extracted and FSA was computed per vertical increment of $\Delta z = 0.25$ m (Figure 9C). The crown area in top view (A_{crown}) was estimated from a 2D convex hull of the projected points, and FSA was normalised to yield:

$$a(z) = \frac{FSA(z)}{A_{\text{crown}}\,\Delta z} \tag{16}$$

To enable comparison, individual tree profiles were upscaled to stand level by multiplying by the forest density. The resulting stand-level estimate was compared in magnitude against the radial band $a(z)$ profile and the subplot $a_{\text{P50}}(z)$ profile, providing an independent consistency check on the $a(z)$ profile derivation methods (Figure 9).

2.6. Forest Stand Structural Characterisation

The $a(z)$ profiles derived at stand, subplot, and tree scales may differ substantially between sites and scales, resulting in corresponding variability in SWAN-predicted wave attenuation. To interpret these differences, two structural metrics were derived: forest patchiness, describing the contrast between vegetated and open areas within the stand, and tree shape similarity, describing the consistency of vertical tree structure among individual trees.

2.6.1 Horizontal Forest Patchiness

Horizontal patchiness was quantified from the subplot sampling approach (Figure 9B). For each subplot i, total frontal surface area was obtained by integrating the vertical $a_i(z)$ profile over height:

$$FSA_{\text{total},i} = \sum_z a_i(z)\,\Delta z \tag{17}$$

Within each sampling repeat, the contrast between densely and sparsely vegetated subplots was quantified as the difference between the 90th and 10th percentile of $FSA_{\text{total},i}$ across the 10 subplots:

$$\Delta FSA_{\text{repeat}} = P90\left(FSA_{\text{total},i}\right) - P10\left(FSA_{\text{total},i}\right) \tag{18}$$

This procedure was repeated 20 times, and the stand-level patchiness metric was taken as the mean across repeats.

$$\overline{\Delta FSA} = \frac{1}{20}\sum_{k=1}^{20} \Delta FSA_{\text{repeat},k} \tag{19}$$

A high value indicates strong contrast between dense and sparse vegetation patches, whereas a low value indicates a spatially homogeneous stand.

2.6.2 Tree Shape Similarity

Tree shape similarity quantified the consistency of vertical tree structure among five individual trees within a stand. For each tree, the $a(z)$ profile was derived as described in Section 2.5.5 and normalised to unit integral:

$$p(z) = \frac{a(z)}{\int a(z)\,dz} \tag{20}$$

This normalisation removes differences in tree size, retaining only the vertical distribution of frontal area. For every pair of trees i, j, the L_1 distance was computed:

$$D_{ij} = \int \left|p_i(z) - p_j(z)\right|\,dz \tag{21}$$

where $D_{ij} = 0$ indicates identical vertical profiles and $D_{ij} = 2$ indicates completely dissimilar profiles. Pairwise similarity was obtained by rescaling the metric to $S_{ij} \in [0, 1]$ (Equation 22), where 1 indicates identical vertical structure.

$$S_{ij} = 1 - 0.5 D_{ij} \tag{22}$$

Similarity was computed for all pairs of sampled trees, and stand-level tree shape similarity was defined as the mean similarity.

2.7. Wave Attenuation Modelling

Wave attenuation by vegetation was represented using a drag-based formulation, in which energy dissipation results from the work performed by wave orbital velocities on submerged vegetation, as described by the drag force of the Morison equation (Morison et al. 1950). Dissipation is expressed as a function of vegetation structure and a bulk drag coefficient C_d, following the vegetation drag formulation of Dalrymple et al. (1984), later extended to spectral wave models by Mendez and Losada (2004). The formulation was further adapted by Suzuki et al. (2012) to account for vertically varying vegetation structure through the frontal surface area density profile $a(z)$. This formulation is implemented in the phase-averaged spectral wave model SWAN and was used to estimate wave attenuation through the structurally diverse floodplain forests characterised in this study using TLS-derived $a(z)$ profiles as vegetation input.

2.7.1 Model Setup and Boundary Conditions

Simulations were performed in a one-dimensional stationary domain replicating the large-scale flume experiments of van Wesenbeeck et al. (2022), including the deep-water section, foreshore ramp, and elevated platform above the flume floor. The vegetated section was positioned at the same location as in the flume experiments, with a forest width of 40 m. To assess the effect of forest width on wave attenuation, the vegetated zone was additionally extended to 100 m and 250 m, while keeping the upstream geometry and vegetation start location fixed.

The computational grid was discretised at a spatial resolution of 1.0 m. Wind growth, whitecapping, refraction, diffraction, quadruplets, triads, turbulence dissipation, and depth-induced breaking were disabled to isolate vegetation-induced dissipation. Bottom friction was included using a roughness constant of 0.07 m^2 s^{-3}. Irregular waves were imposed at the offshore boundary using a JONSWAP spectrum with directional spreading of $\pm 90^\circ$ and a directional resolution of 2°, discretised over 0.05–1.0 Hz using 60 frequency bins. Significant wave heights H_s of 0.5, 1.0, and 1.5 m were combined with peak periods T_p of 3, 4, and 6 s, representing wind-generated river wave conditions and young, developing wave spectra typical of Dutch floodplain environments (van Wesenbeeck et al. 2022). The resulting fictitious deep-water wave steepness $S_{op} = \frac{H_s}{gT_p^2/2\pi}$ ranged between 0.02 and 0.06, which is consistent with the parameter space of the flume experiments of van Wesenbeeck et al. (2022), thereby providing a validated physical basis for the selected wave conditions. Five water levels of 1.6, 3.0, 4.0, 4.5, and 9.1 m were selected to span the probability distribution of inundation depths at the study sites (Figure 10). Wave attenuation was evaluated at a fixed location downstream of the forest edge. The full simulation matrix is summarised in Table 2.

Table 2: Simulation matrix combining hydraulic forcing, forest width, and vegetation scenarios.

Parameter	Values	Cases
Water level h (m)	1.6, 3.0, 4.0, 4.5, 9.1	5
Significant wave height H_s (m)	0.5, 1.0, 1.5	3
Peak period T_p (s)	3, 4, 6	3
Forest width W (m)	40, 100, 250	3
Vegetation scenarios	14 stands $\times$ 4 $a(z)$ profiles	56
Total simulations		7,560

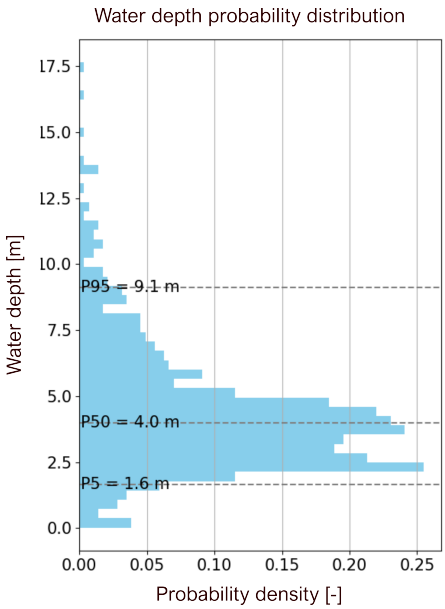

Figure 10: Water level exceedance probability distribution at the study sites derived from Hydra-NL hydraulic boundary condition statistics (Rijkswaterstaat 2017). Selected percentiles (P5, P50, P95) are indicated.

2.7.2 Vegetation Representation and Drag Coefficient

In the standard SWAN vegetation module, dissipation per vertical layer scales with the product $b_v N_v$, representing frontal area density per unit volume (Suzuki et al. 2012; Mendez and Losada 2004). Following Kalloe et al. (2022), this product was replaced directly by the TLS-derived vertical frontal area density profile $a(z)$, discretised into layers of 0.25 m thickness, enabling direct use of the measured vegetation geometry without simplification to cylindrical stems. Vegetation-induced dissipation is represented as a function of the interaction between submerged frontal surface area density, the drag coefficient, and the wave orbital velocity field, effectively proportional to $a(z)\, C_d(z)\, u(z)^3$ integrated over the vertical vegetation profile.

The bulk drag coefficient C_D was parameterised as a function of the Keulegan–Carpenter number (Keulegan and Carpenter 1958), evaluated per vertical layer as:

$$KC(z) = \frac{u_{\max}(z)\, T_p}{D(z)} \tag{23}$$

Where $u_{\max}(z)$ is the maximum horizontal orbital velocity amplitude at elevation z, T_p is the peak period, and $D(z)$ is a representative vegetation diameter. $D(z)$ was prescribed as piecewise constant, with separate representative diameters for the stem and canopy zones. The C_D–KC relationship was adopted from van Wesenbeeck et al. (2022) and Kalloe et al. (2022), fitted to large-scale flume experiments on pollarded willow trees:

$$C_D = \begin{cases} -0.53 \ln(KC) + 3.41, & KC \leq 120 \\ 0.7, & KC > 120 \end{cases} \tag{24}$$

This parameterisation reflects the emperically observed decrease in C_D with increasing KC for woody vegetation under oscillatory flow (Jadhav et al. 2013; van Wesenbeeck et al. 2022). The plateau at $C_D = 0.7$ for high KC accounts for mechanical branch bending and swaying, which reduces the effective drag compared to rigid structures (van Wesenbeeck et al. 2022; van Starrenburg, van Ijzerloo, et al. 2025).

3. Results: Forest Structure, TLS Reliability and Wave Attenuation

3.1. Forest Stand Characterisation and Forest Density Estimation

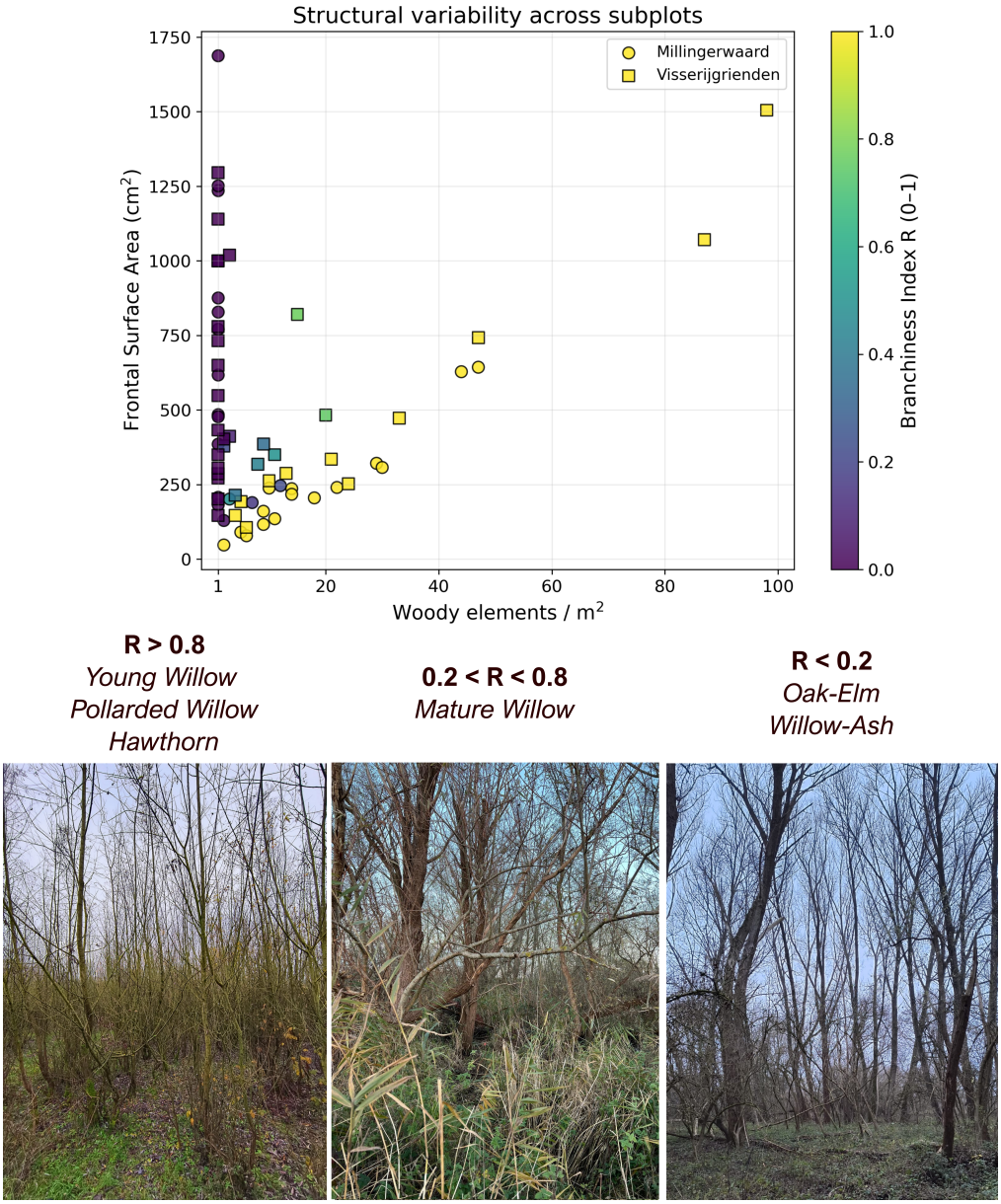

Figure 11: Relationship between frontal surface area (FSA) and woody element density across 1×1 m subplots. Points are coloured by the Branchiness Index (R); photographs illustrate representative forest stands across the R range.

Six stand types were identified across the 14 forest stands at two study sites. Millingerwaard comprised Young Willow, Hawthorn, Mature Willow, Willow–Ash, and Oak–Elm stands, while Visserijgrienden was represented by Pollarded Willow and Mature Willow stands. Mature Willow occurred at both sites and was treated as a single pooled stand type ($n = 8$), where n represents the number of individual forest stands included in this category.

Stand types differed systematically in subplot-scale complexity at 1 m height, as characterised by the Branchiness Index R. Frontal surface area (FSA) at this height showed contrasting relationships with woody element density across stand types (Figure 11). Oak–

Elm and Willow–Ash exhibited consistently low Branchiness Index values ($R \approx 0$–0.2) and showed no relationship between FSA and woody element density, indicating that FSA was primarily controlled by stem size rather than the number of woody elements, reflecting a stem-dominated vegetation structure at 1 m height. In contrast, Pollarded Willow, Hawthorn, and Young Willow showed high Branchiness Index values ($R \approx 0.8$–1.0) and displayed a clear positive relationship between FSA and woody element density, reflecting branch-dominated vegetation structure in which increasing numbers of branches directly increase FSA. Mature Willow stands spanned the widest range of R values ($R \approx 0.2$–0.8), occupying an intermediate position between these two structural regimes and showing both stem- and branch-controlled characteristics, consistent with their structurally heterogeneous and irregular form.

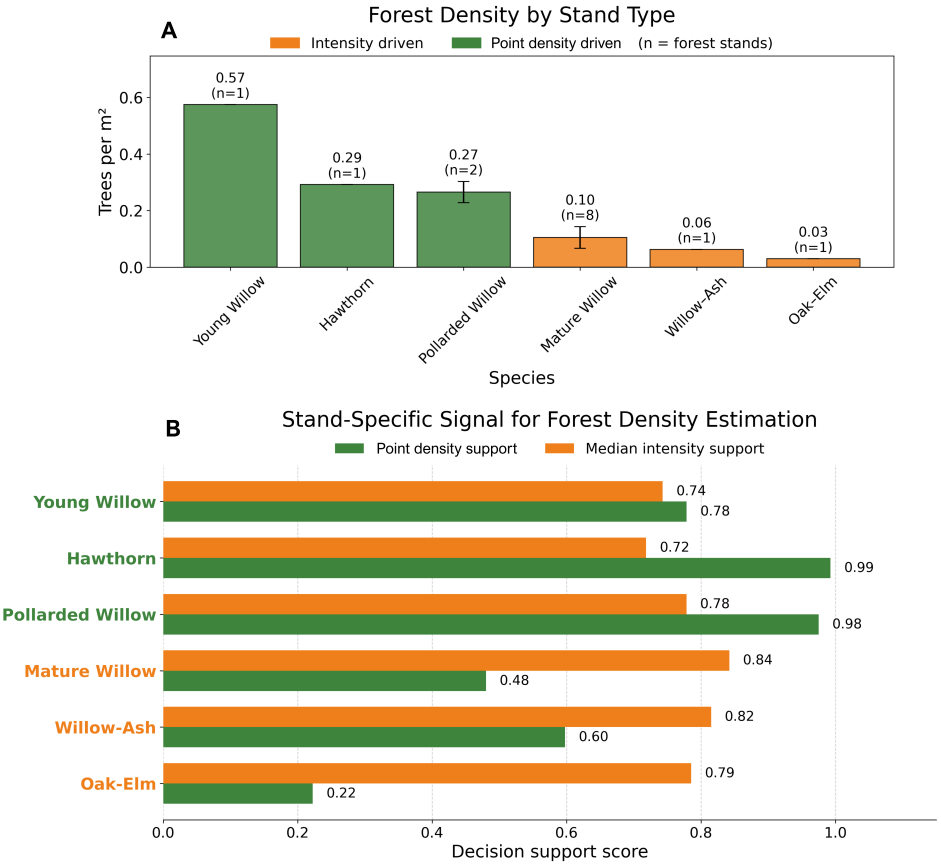

Figure 12: TLS-based forest density estimation across stand types. (A) Decision support scores for point density and median return intensity within the stands. (B) TLS-derived forest density (trees/m^2) per stand type, coloured by dominant detection method. Error bars indicate the standard deviation across forest stands within a stand type when $n > 1$.

The dominant TLS detection signal differed systematically between stand types (Figure 12B). Stands characterised by branchy structure at 1 m height (Young Willow, Hawthorn, Pollarded Willow) showed stronger detection support for point density than for return intensity, with decision support scores of 0.74, 0.72, and 0.78, respectively. Tree detection in these branch-dominated stands was therefore based on the 99th percentile of point density in 2 m radial intervals. In contrast, stands characterised by more open, stem-dominated structure (Oak–Elm, Willow–Ash, Mature Willow) showed stronger discriminatory support for return intensity. This reflects the dominance of larger woody surface areas in these stands, which produce stronger and more consistent return intensity signals than the smaller branch elements typical of the branchy stands. Tree detection in these stands was therefore based on

the global 97th percentile of return intensity. Examples of the resulting detection are shown in Figure 13A–B. In the Pollarded Willow stand, reliable detection was limited to distances of approximately 6 m, as point density declined rapidly with scanner distance within the dense branching canopy (Figure 13A). In the Oak–Elm stand, the stronger and more persistent intensity signal from large woody stems allowed tree detection at distances up to approximately 25 m, reflecting both the larger woody surface area of stems and the more open stand structure (Figure 13B).

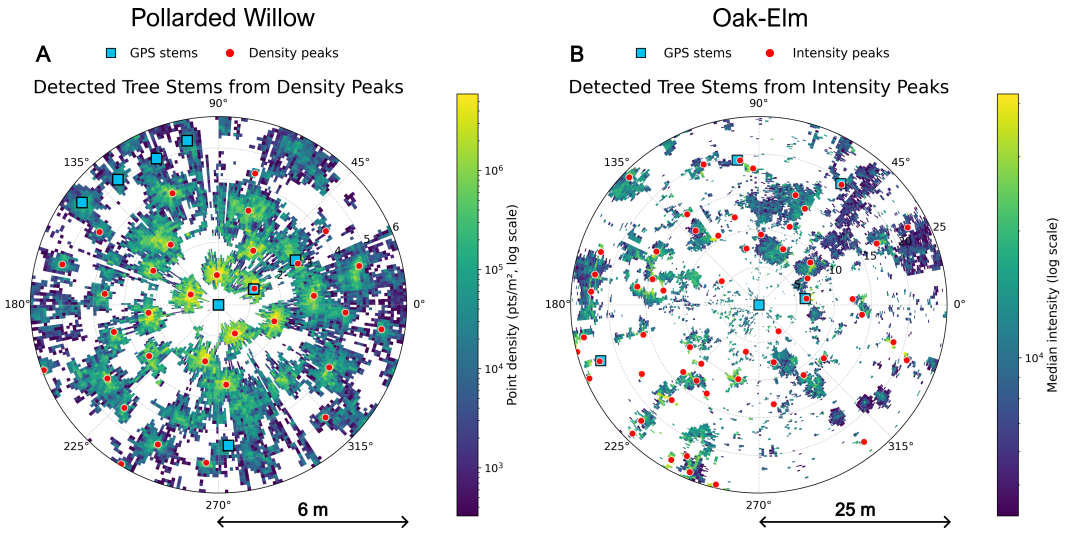

Figure 13: Examples of TLS-based tree detection. (A) Point density driven tree detection in a Pollarded Willow stand. Colour indicates point density (points/m^2, log scale). (B) Intensity-driven tree detection in an Oak–Elm stand. Colour indicates median return intensity; red dots indicate detected tree stems and blue squares indicate GPS-referenced trees.

TLS-derived forest density reflected the structural differences between stand types (Figure 12B). Highest densities occurred in pioneer and managed stands, with Young Willow (0.57 trees/m^2) and Hawthorn (0.29 trees/m^2) showing the largest values. Pollarded Willow exhibited similarly high density (0.27 trees/m^2), reflecting regular spacing resulting from pollarding management. Mature Willow stands showed intermediate densities (0.10 trees/m^2), consistent with their structural diversity. In contrast, the lowest densities occurred in Oak–Elm (0.03 trees/m^2) and Willow–Ash (0.06 trees/m^2), representing mature forests characterised by large stems and wider tree spacing. Together, these patterns reveal a structural gradient from dense, branch-dominated stands to open forests dominated by individual stems. This gradient aligns with patterns observed in other riparian floodplains, where dense willow and shrub stands contrast with the more open structure of mature forests (Fehérváry and Kiss 2021).

3.2. TLS Reliability Assessment

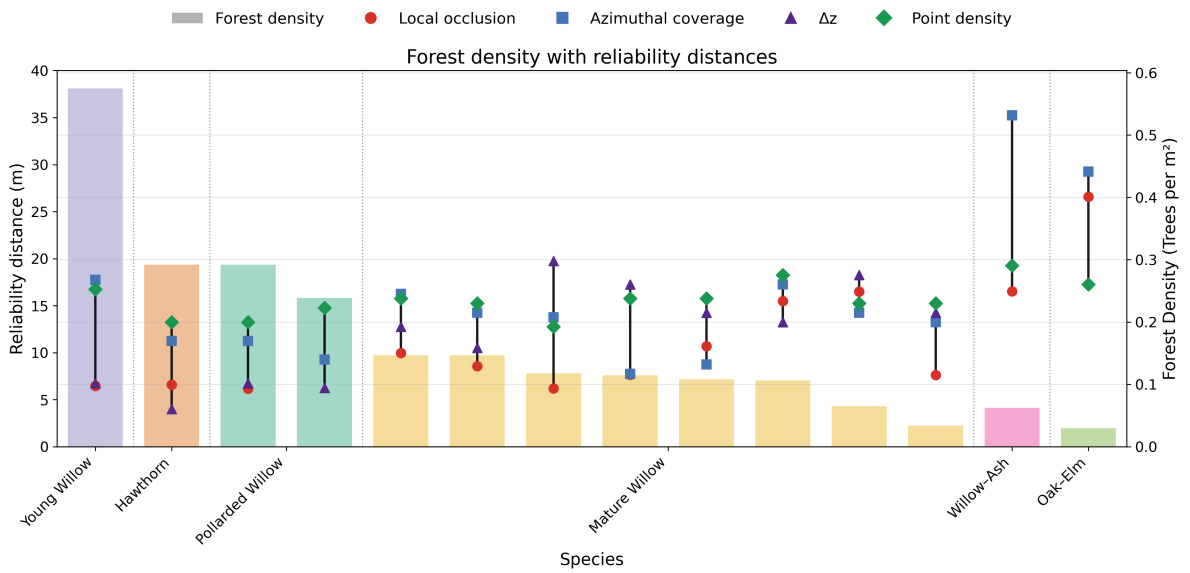

Figure 14: Final reliability distance (d_{reliable}) as a function of TLS-derived forest density across all scans. Bars indicate forest density (trees/m^2) for each stand. Markers represent the reliability distance estimated from the four criteria, with marker shape and colour indicating the criterion. The final reliability distance d_{reliable} is defined as the minimum across the four criteria.

The final reliability distance, defined as the minimum across all reliability criteria, varied systematically with stand structure across the surveyed forests (Figure 14). Scan-specific reliability distances d_{reliable} ranged from approximately 4 to 16 m across the 14 scans. Shortest reliability distances occurred in dense, branch-dominated stands, including Young Willow (6 m), Hawthorn (4 m), and Pollarded Willow (6 m), reflecting strong occlusion at short ranges. In contrast, sparse, stem-dominated stands showed the largest reliability distances, with Oak–Elm reaching 16 m and Willow–Ash 12 m, where the more open forest structure allowed reliable detection at greater distances. Mature Willow exhibited intermediate reliability distances of approximately 8 m, consistent with its structural diversity.

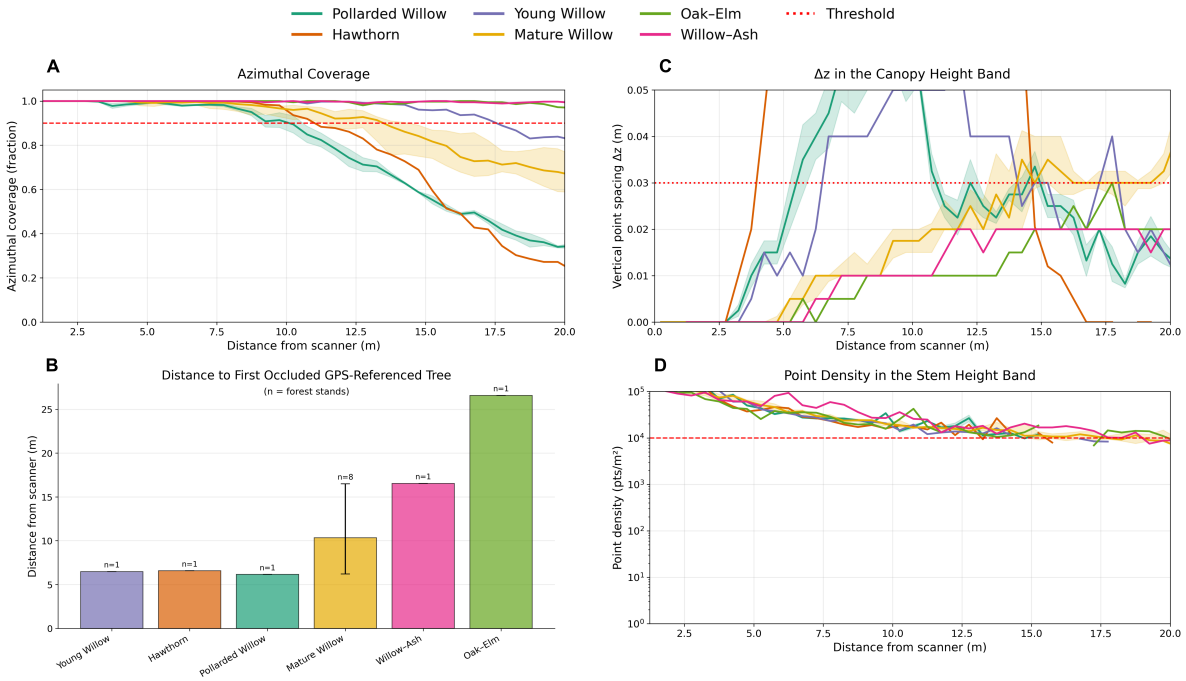

Figure 15: Stand-type-dependent behaviour of TLS reliability criteria as a function of scanner distance. Lines represent median values across scans per stand type and shaded areas indicate interquartile ranges (Q25–Q75). (A) Azimuthal coverage fraction; dashed red line indicates the 0.9 reliability threshold. (B) GPS-referenced tree detectability (distance to first undetected tree). (C) Point density in the stem height band (0.7–1.8 m; log scale); dashed red line indicates the 10,000 pts m^{-2} reliability threshold. (D) Vertical point spacing Δz_{90-50} in the canopy height band (>1.8 m); dashed red line indicates the 0.03 m reliability threshold.

The individual reliability criteria showed clear dependence on forest structure (Figure 15). Vertical sampling adequacy (Δz) exhibited the strongest stand-type dependence, with dense, branch-dominated stands (Hawthorn, Young Willow, Pollarded Willow) exceeding the Δz_{90-50} threshold at substantially shorter distances than the more open Oak–Elm and Willow–Ash stands (Figure 15C). This reflects the ground-based TLS acquisition geometry, where dense branching structures rapidly occlude the upper canopy and reduce vertical sampling quality with distance. The apparent decrease in Δz_{90-50} at larger distances reflects reduced bin occupancy rather than improved vertical resolution. Figure 16A illustrates the spatial increase in vertical point spacing with scanner distance for a representative Hawthorn scan.

Azimuthal coverage and GPS-referenced tree detectability (representing local occlusion) showed a similar structural response, declining most rapidly in the dense stands while remaining above the threshold over larger distances in the more open forests (Figure 15A–B). Both criteria closely correspond to forest density, as denser stands block and occlude more directions with increasing distance from the scanner.

In contrast, point density showed the weakest stand-type dependence, with the stem height band (0.7–1.8 m) reaching the 10,000 pts/m^2 threshold at broadly similar distances across stands (Figure 15D). The corresponding radial decay in point density is illustrated in Figure 16B.

Together, these patterns demonstrate that branching complexity and forest density strongly constrain the spatial extent over which reliable TLS-derived structural metrics can be obtained.

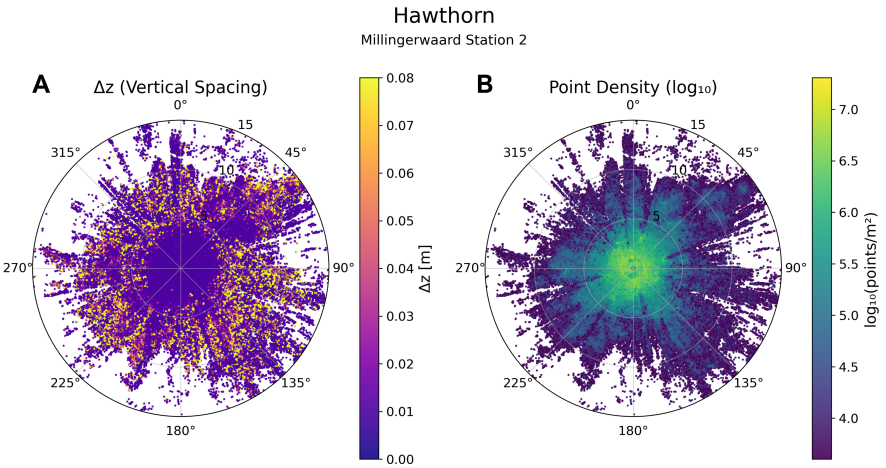

Figure 16: Polar representation of distance-dependent TLS sampling characteristics for an example Hawthorn scan. (A) Vertical point spacing Δz (m), illustrating the increase in vertical sampling distance with increasing distance from the scanner. (B) Point density (pts/m^2, log scale), illustrating the rapid radial decay in point density with distance from the scanner.

3.3. FSA Reconstruction and $a(z)$ Profile Derivation

3.3.1 Method Selection

Voxel-based reconstruction outperformed the alpha-shape method across all validation trees at both study sites combined (Figure 17). Validation and parameter optimisation were restricted to trees located within the scan-specific reliability distance, as trees beyond this distance would introduce resolution-related biases that are not representative of the scan domain used for vegetation parameterisation in the model. The voxel method yielded a slope of 0.95, $R^2 = 0.98$, and a median bias of -0.3%, compared to a slope of 0.70, $R^2 = 0.79$, and a median bias of -2.7% for the alpha-shape method. The alpha-shape approach showed greater sensitivity to parameter selection, reflected by the wider parameter range shown in the colour bar of Figure 17. Based on this validation, voxelisation was selected for all subsequent FSA reconstruction.

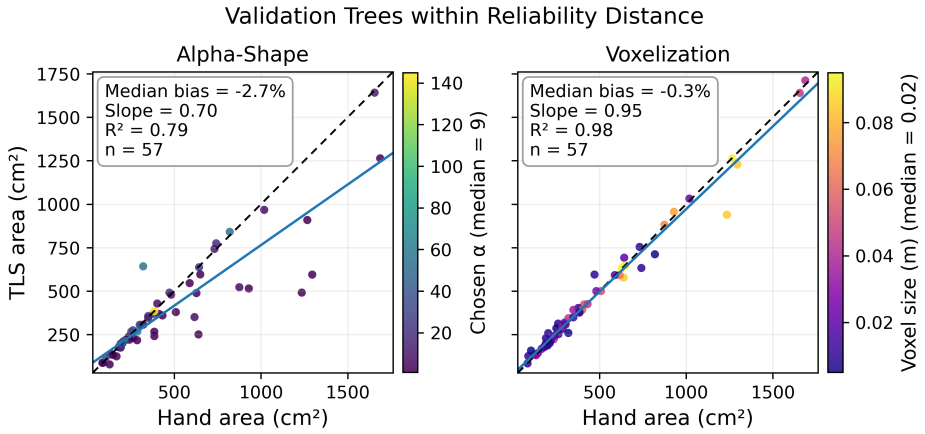

Figure 17: Validation of TLS-derived FSA against hand measurements for alpha-shape and voxel-based reconstruction methods across all validation trees at both study sites ($n = 57$). Only trees within the scan-specific reliability distance were included. Colour indicates the optimised reconstruction parameter. Dashed line shows the 1:1 reference; solid line shows the fitted regression.

3.3.2 Stand-Type-Specific Voxel Parameterisation

Optimal voxel sizes varied substantially among stand types, ranging from 0.01 to 0.09 m across all validation trees with a median of 0.02 m (Figure 17). This reflects differences in vegetation structure across the studied stands. To account for these structural differences, stands were grouped into three structural classes based on their Branchiness Index, enabling stand-type-specific voxel parameterisation (Figure 18A-B-C). Voxel sizes within each structural group were then determined by minimising MAE between TLS-derived and field-measured FSA within the reliability distance.

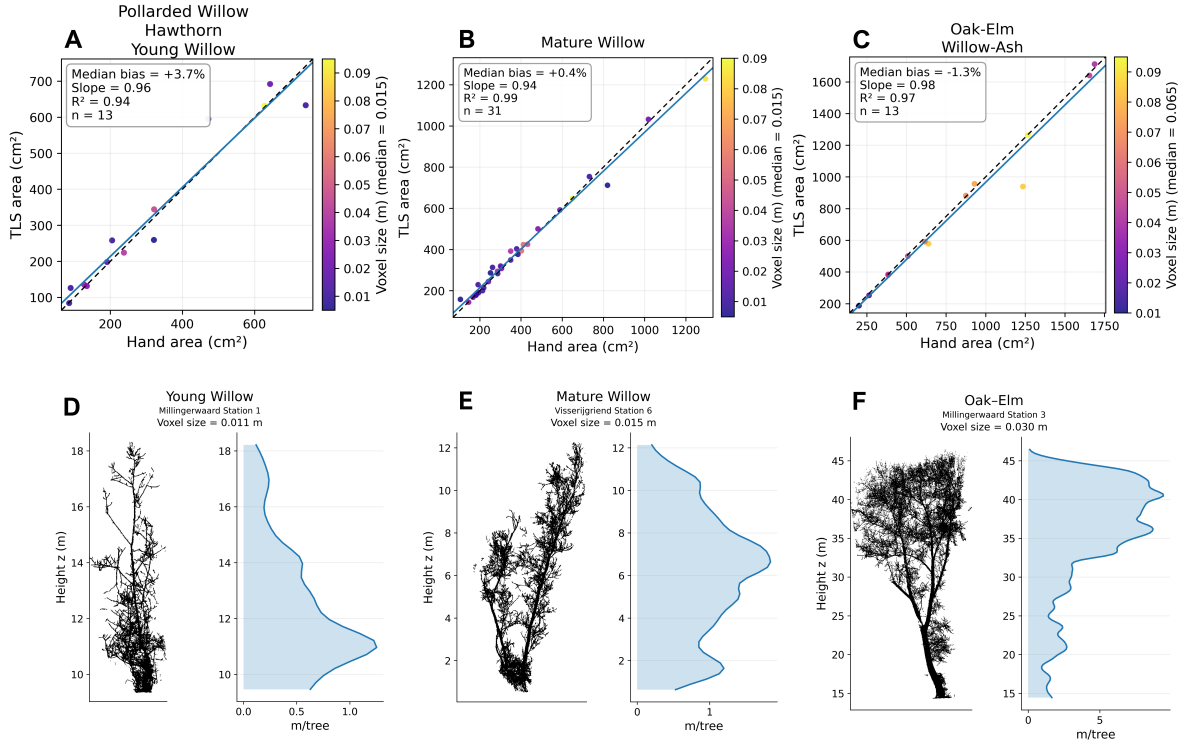

Figure 18: (A–C) Iterative voxelisation results used to determine the optimal voxel size for each structural group. (D–F) Representative TLS reconstructions of individual trees using the selected voxel sizes, demonstrating that the chosen resolution captures structural elements without systematic under- or overestimation of frontal surface area.

Branch-dominated stands (Hawthorn, Young Willow, Pollarded Willow) were assigned a voxel size of 0.011 m, corresponding to the fine diameter scale of branches and slightly above the minimum TLS point spacing (0.01 m), ensuring continuous reconstruction without gaps caused by the scan resolution (Figure 18A). Mature Willow, representing structurally heterogeneous stands, retained the iterative optimum of 0.015 m, reflecting the presence of both fine branches and larger woody elements (Figure 18B). Stem-dominated stands (Oak–Elm, Willow–Ash) were assigned a voxel size of 0.03 m, representing the smallest value that did not result in overestimation of stem frontal surface area upon visual inspection (Figure 18C). All parameter assignments were verified by visual inspection of reconstructed point clouds for five representative trees per stand type (Figure 18D-E-F).

3.4. Vertical Frontal Surface Area Density Profiles and Stand Structural Characterisation

3.4.1 Stand-Level $a(z)$ Profiles

Vertical frontal surface area density profiles $a(z)$ differed substantially among stand types, reflecting differences in vegetation structure and canopy height (Figure 19). Hawthorn, Young Willow, and Pollarded Willow exhibited concentrated frontal surface area in the lower vegetation layer, with peak $a(z)$ values occurring below approximately 5–6 m height, reflecting their dense, branch-dominated structure. In contrast, Willow–Ash and Oak–Elm stands showed broader vertical distributions of frontal surface area, reflecting the presence of larger stems and taller trees. Mature Willow exhibited an intermediate structure, with greater frontal surface area than the Oak–Elm and Willow–Ash stands, extending vertically up to approximately 20 m.

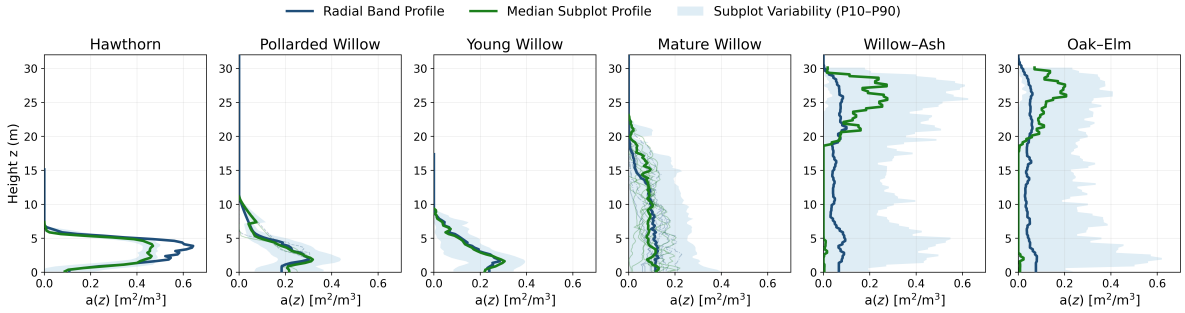

Figure 19: Vertical frontal surface area density profiles $a(z)$ derived from the radial band method (blue) and subplot median P50 (green), with subplot P10–P90 envelope (light blue) indicating within-stand spatial variability. Profiles are shown for the six stand types analysed in this study.

Subplot-derived P10–P90 envelopes revealed clear differences in within-stand structural variability. Hawthorn, Young Willow, and Pollarded Willow showed relatively narrow envelopes, indicating limited subplot variability and relatively homogeneous vegetation structure. In contrast, Mature Willow, Willow–Ash, and Oak–Elm exhibited substantially wider P10–P90 envelopes, reflecting greater horizontal patchiness and structural heterogeneity within the stand. Consistent with this pattern, the radial band profile and subplot median (P50) agreed closely in the structurally homogeneous stands. In contrast, divergence between the two profiles occurred in the lower-density Willow–Ash and Oak–Elm stands. Here, the subplot method captures horizontal patchiness through empty or sparsely vegetated subplots, while the radial band method yields a spatially averaged stand profile.

3.4.2 Stand Structural Characterisation

Stand patchiness and tree shape variability differed systematically between stand types (Figure 20B), providing a physical basis for the between-stand differences in $a(z)$ profile variability observed in Figure 19.

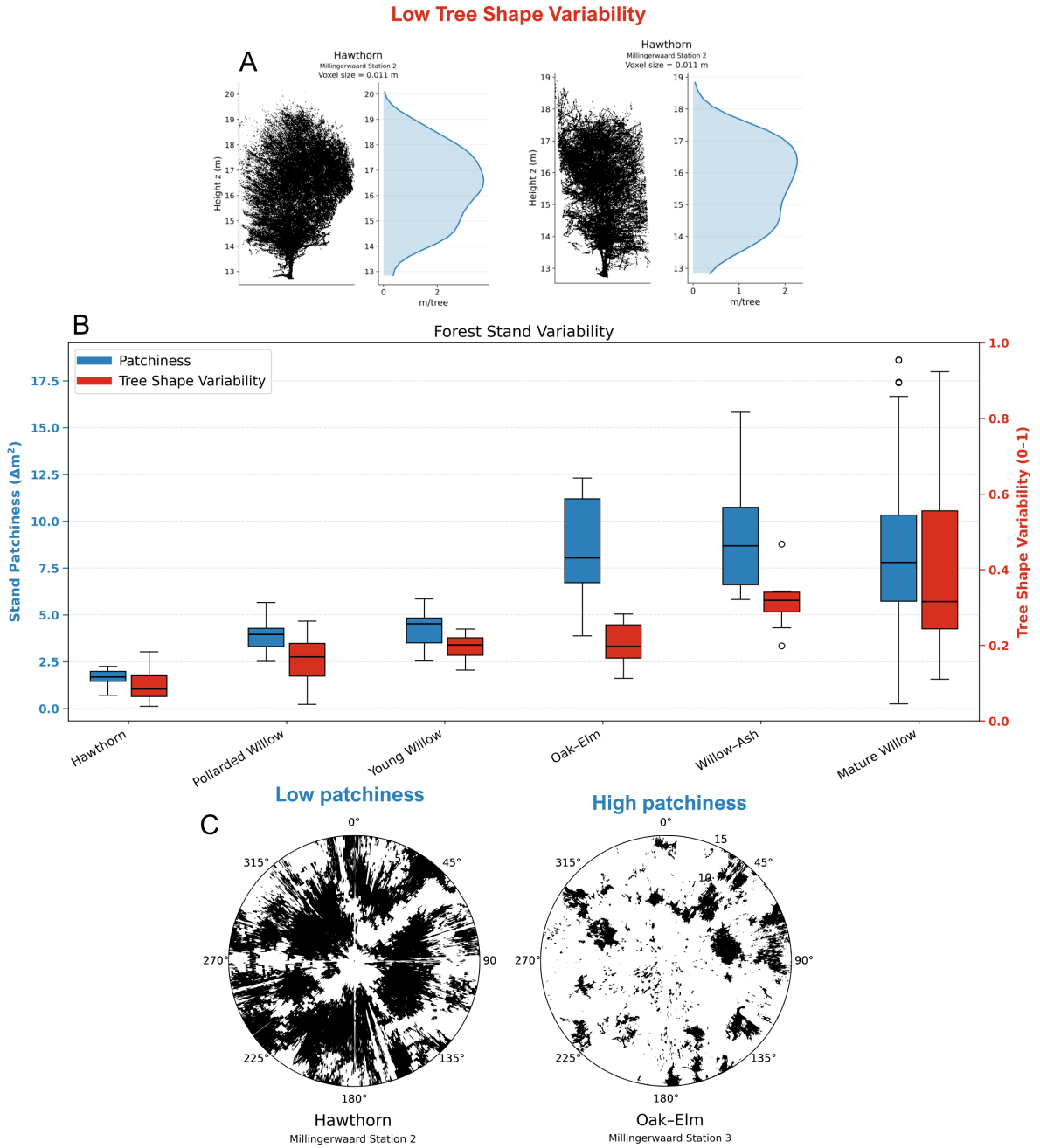

Figure 20: Stand structural characterisation across six stand types. (B) Stand patchiness (Δm^2 of the subplots (blue)) and tree shape variability (scale 0–1 where low indicates similar vertical tree structure (red)) per stand type, derived from subplot sampling and pairwise tree profile comparison. (A) Example TLS point cloud of individual Hawthorn trees illustrating low tree shape variability. (C) Polar point density map of a Hawthorn and Oak-Elm scan, illustrating low and high stand patchiness

Horizontal forest patchiness, quantified as the mean difference between the P90 and P10 subplot frontal surface area ($\overline{\Delta FSA}$), differed substantially among stand types. Hawthorn,

Young Willow, and Pollarded Willow exhibited the lowest patchiness values ($\approx 1 - 5\ \Delta m^2$), indicating relatively homogeneous vegetation structure, whereas Oak–Elm, Willow–Ash, and Mature Willow showed substantially higher patchiness values ($\approx 6 - 12\ \Delta m^2$), indicating pronounced horizontal heterogeneity and the presence of vegetation gaps within the stand (Figure 20C). This pattern is consistent with the previously observed forest density values. Consequently, homogeneous stands produce relatively narrow subplot $a(z)$ envelopes, whereas patchy stands exhibit a substantially wider range of $a(z)$ values across subplots. In these sparser stands, subplot sampling frequently falls between stems, causing the subplot P50 to approach zero near stem height. When vegetation is encountered, it more often consists of crown material, resulting in higher $a(z)$ values above the stem zone. Therefore, the radial band profile provides a more representative stand-averaged vegetation distribution, whereas the subplot P50 reflects the most probable local vegetation condition within the patchy stand structure.

Hawthorn, Young Willow, and Pollarded Willow exhibited low variability in vertical tree structure, with individual trees displaying similar $a(z)$ profiles (Figure 20A). In contrast, Mature Willow exhibited the highest tree shape variability (Figure 20B), indicating substantial differences in vertical frontal surface area distribution among individual trees, consistent with the structurally diverse vegetation structure of mature willow stands.

The between-stand differences in $a(z)$ profile shape and magnitude were subsequently propagated into the SWAN wave attenuation model as alternative vegetation input scenarios, with the profiles representing a range of vegetation configurations used to evaluate the sensitivity of simulated wave attenuation to within-stand structural variability.

3.5. SWAN Wave Attenuation Response

The TLS-derived $a(z)$ profiles were implemented in SWAN to evaluate how between-stand differences in vegetation structure translate into wave attenuation across a range of hydraulic conditions and forest widths. The P10, P50, P90 and radial band profiles served as alternative vegetation input scenarios, propagating the structural variability characterised in Section 3.4 directly into the attenuation estimates.

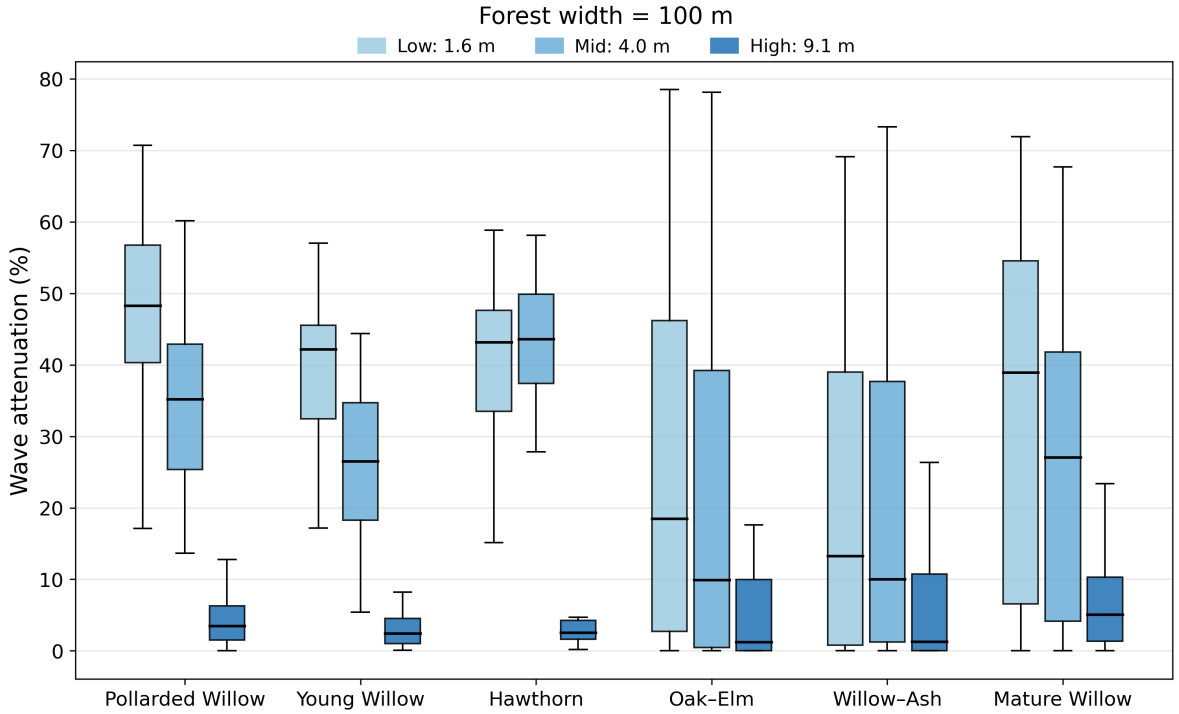

Figure 21: Simulated wave attenuation across forest stand types for a forest width of 100 m under three water levels (low: 1.6 m, mid: 4.0 m, high: 9.1 m). Boxplots represent attenuation variability resulting from vegetation structural scenarios derived from TLS-based $a(z)$ profiles (P10, P50, P90 and radial band). The spread of each boxplot reflects the influence of within-stand structural variability on wave attenuation.

Wave attenuation varied substantially between stand types and water levels at a forest width of 100 m (Figure 21). Hawthorn, Young Willow, and Pollarded Willow produced the highest attenuation at low water level (≈45%), consistent with their high frontal surface area density concentrated in the lower vegetation layers where orbital velocities are greatest. As water level increased, attenuation decreased markedly for these stands because the wave-active layer shifted above the height range of maximum frontal surface area density. This demonstrates that dense low-canopy vegetation provides strong attenuation under low water level conditions but becomes less effective as water levels rise and wave motion interacts with sparser upper canopy layers. Hawthorn maintained relatively consistent attenuation across low and mid water levels (≈43%), reflecting its compact but dense vertical structure that remains largely within the wave-active layer.

In contrast, patchy and more heterogeneous forests produced substantially larger attenuation variability. Oak–Elm and Willow–Ash produced lower median attenuation (≈18% and 12% respectively at low water level) but exhibited the widest attenuation ranges, with lower bounds approaching zero. This reflects the patchiness-driven P10 $a(z)$ profiles of these stands, in which the most probable local vegetation condition corresponds to inter-stem open

space, producing near-zero wave dissipation. Where vegetation is intercepted, however, their vertically persistent frontal surface area can locally generate strong attenuation approaching ∼80%. This indicates that horizontal vegetation patchiness strongly controls the reliability of wave attenuation, producing either negligible dissipation or strong attenuation depending on whether waves encounter vegetation clusters or structural gaps. Mature Willow exhibited relatively high attenuation at low (∼40%) and mid (∼25%) water levels, exceeding the median attenuation of Oak–Elm and Willow–Ash, but with a large spread in attenuation outcomes. This variability reflects the high dissimilarity in individual tree structure and the pronounced horizontal patchiness within this stand type.

Overall, these results show that vegetation structure governs both the magnitude and predictability of wave attenuation: vertical vegetation structure controls the overall attenuation capacity, whereas horizontal patchiness and tree structural variability determine the variability of attenuation outcomes.

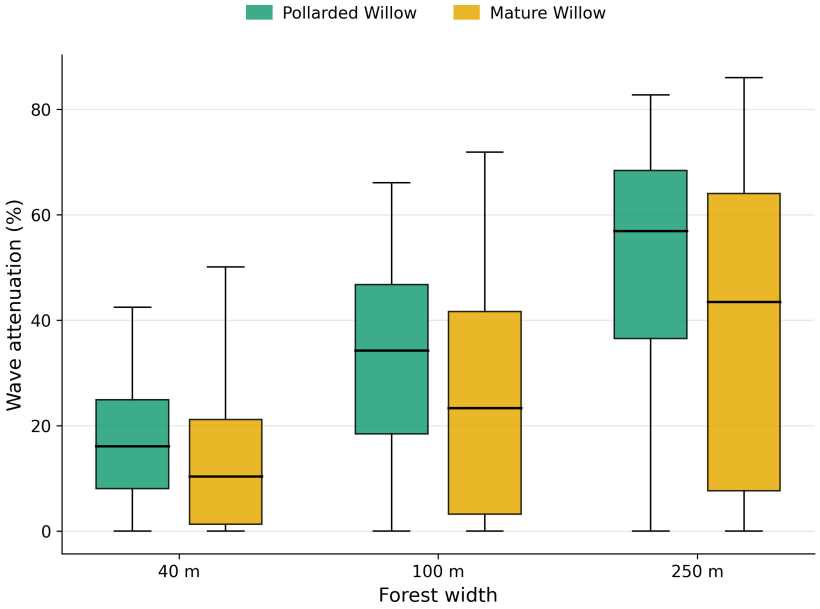

Figure 22: Simulated wave attenuation as a function of forest width (40, 100, and 250 m) for two riparian forest stand types: Pollarded Willow and Mature Willow. Boxplots summarise attenuation outcomes across vegetation structural scenarios and hydraulic conditions.

Wave attenuation increased with forest width across all hydraulic conditions and species. Median attenuation increased from approximately 15% at 40 m to 30% at 100 m and 50% at 250 m. However, the variability of attenuation outcomes differed strongly between stand types (Figure 22).

Pollarded Willow showed relatively limited variability across forest widths, reflecting its dense and structurally consistent vegetation profile. The resulting wave attenuation therefore increases predictably with forest width, as waves progressively lose energy along the vegetated transect.

In contrast, Mature Willow exhibited substantially larger variability in attenuation that increased with forest width. This reflects the greater within-stand heterogeneity of this stand type. As forest width increases, differences between the structural scenarios accumulate along the wave propagation path, resulting in an increasing spread in attenuation outcomes.

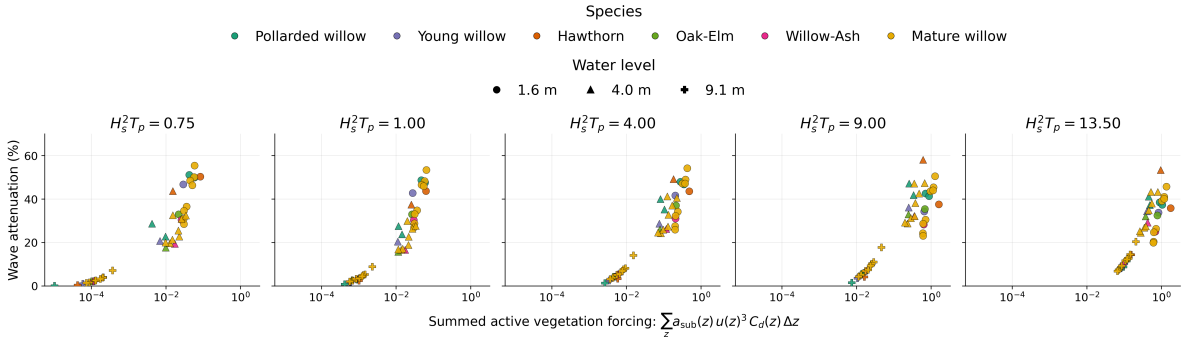

Figure 23: Relationship between summed active vegetation forcing and simulated wave attenuation for a forest width of 100 m using radial band $a(z)$ profiles. Each panel represents a different wave condition (H_sT_p). Points show simulations across forest stand types and water levels.

Across all vegetation and hydraulic scenarios, wave attenuation increased systematically with the summed active vegetation drag forcing term $\sum_z a_{\mathrm{sub}}(z)\,u(z)^3\,C_d(z)\,\Delta z$ (Figure 23). Lower values of vegetation forcing occur on the left-hand side of the panels and correspond to simulations with low attenuation near the bottom of the plots. These conditions occur when a smaller portion of the vegetation structure interacts with wave orbital motion. For example, higher water levels reduce the fraction of vegetation located within the wave-active layer, resulting in lower vegetation drag forcing and attenuation. Accordingly, simulations for the highest water level (cross symbols) are concentrated toward the lower-left region of the forcing–attenuation space. Conversely, as water levels decrease, a larger fraction of the vegetation structure falls within the wave-active layer and interacts with wave orbital motion. Increasing wave height and peak period strengthen orbital velocities and extend them deeper into the water column. Together, these processes increase vegetation drag forcing and shift simulations toward higher forcing values and greater attenuation.

Despite this overall trend, stand types exhibit different attenuation responses across the forcing range. At lower forcing values, Mature Willow produces the highest attenuation among the stand types. In contrast, at higher forcing values Hawthorn produces the highest attenuation. Despite stand-specific attenuation patterns, the overall relationship demonstrates that wave attenuation is governed by the interaction between vertical vegetation structure $a(z)$, the orbital velocity profile $u(z)$, and the drag coefficient $C_d(z)$, which together determine the effective vegetation drag forcing experienced by the waves.

4. Discussion

4.1. Vegetation Structure as a Control on Wave Attenuation

Field evidence on the wave attenuation capacity of natural forests remains limited, and vegetation in hydraulic models is still commonly represented using simplified geometry. Such representations frequently neglect vertical structural variability and spatial heterogeneity within natural stands, which may lead to inaccurate predictions of flood risk reduction (Gijón Mancheño et al. 2024). This limitation is particularly relevant given the growing interest in nature-based flood defence solutions, where vegetated foreshores are increasingly considered as complementary protection for levees and dikes but require reliable estimates of wave attenuation. Recent studies have begun to address these simplified representations by using TLS to derive vertically resolved vegetation structure metrics such as frontal surface area profiles (Dunlop et al. 2025; Kalloe et al. 2022). Experimental studies further demonstrated that frontal surface area is the

primary structural predictor of wave attenuation in pollarded willow forests (van Wesenbeeck et al. 2022; Kalloe et al. 2022), where vegetation structure was derived from representative trees. However, these approaches do not capture spatial variability in forest structure within natural stands. Building on this work, van Starrenburg, Mancheño, et al. (2026) compared pollarded, plantation, and naturally developed willow forests using plot-scale measurements and branching models, but these analyses remained restricted to limited plots within a single floodplain system. Consequently, the influence of structural variability within natural riparian forests on wave attenuation remains poorly understood. The present study addresses this gap by quantifying wave attenuation across structurally diverse floodplain forests, showing that attenuation capacity is strongly condition-dependent and governed by both the vertical distribution and spatial organisation of submerged frontal surface area.

Across all investigated hydraulic scenarios, vegetation structure emerged as the primary control on wave attenuation. Wave dissipation scales with the summed vegetation forcing, $\sum_z a(z)\, u(z)^3\, C_d(z)\, \Delta z$, meaning attenuation is maximised when vegetation frontal area is concentrated within the depth range where orbital velocities are highest. Because orbital velocity profiles vary with water level and wave forcing, the part of the vegetation layer that contributes most to wave attenuation shifts accordingly. Attenuation capacity is therefore an emergent outcome of the interaction between vegetation structure and hydrodynamic forcing. In structurally complex natural forests, this interaction produces scenario-dependent wave attenuation that simplified or uniform vegetation representations cannot capture.

4.2. Patchiness and Attenuation Uncertainty

While vertical structure determines attenuation magnitude, horizontal patchiness governs attenuation uncertainty. Vegetation profiles revealed substantial variability in local frontal surface area within structurally heterogeneous stands. In sparse stands such as Oak–Elm, the 10th-percentile vegetation profiles frequently approached zero at stem height, reflecting the spacing between stems. When these profiles were implemented in the wave model, attenuation outcomes ranged from near-zero to strong dissipation ($\approx 80\%$) within the same stand type. This behaviour highlights a limitation of bulk vegetation parameterisations commonly used in wave–vegetation interaction modelling. Sparse vegetation is typically represented by uniformly scaling a representative frontal surface area profile $a(z)$, implicitly assuming that vegetation structure is spatially continuous along the forest transect. For example, global mangrove modelling by Wesenbeeck et al. (2025) represented sparse and dense forests by applying a fixed $\pm 20\%$ deviation to the total frontal surface area while maintaining a uniform vegetation profile along the transect. The results of this study show that sparsity in natural riparian forests instead forms a spatial mosaic of dense vegetation clusters and open gaps. Consequently, attenuation depends on whether waves interact with dense vegetation patches or propagate through open gaps. Representing vegetation with a single reduced structural profile can therefore mask the large variability in attenuation potential observed within heterogeneous stands.

4.3. Advancing TLS-Based Structural Quantification

Previous TLS-based vegetation studies have highlighted the importance of sufficient sampling to represent structural variability. For example, Dunlop et al. (2025) suggested that approximately 35–45 trees are required to obtain a convergent stand-average structure in heterogeneous mangrove forests, effectively smoothing local variability into a representative vegetation profile. The results of the present study indicate that such stand-average profiles can be misleading in structurally patchy riparian forests. In sparse stands, the 10th-percentile (P10)

frontal surface area profile frequently approached zero at stem height, reflecting the presence of inter-stem gaps. By deriving percentile envelopes (P10–P90) from multiple spatial subplots, the framework adopted here captures the full range of structural conditions within a stand and enables attenuation uncertainty to be quantified, rather than relying on a single representative vegetation structure. In addition to representing structural variability, the TLS workflow developed in this study aims to improve the reconstruction of vegetation geometry. Previous studies commonly applied fixed geometric parameters, such as an $\alpha = 0.01$ alpha-shape parameter (Kalloe et al. 2022; Dunlop et al. 2025), whereas this study uses structure-dependent voxel reconstruction evaluated against field measurements. By matching voxel size to the physical dimensions of vegetation elements, the reconstruction better represents vegetation geometry, a scale dependency also reported in TLS vegetation studies (Antonarakis, Richards, Brasington, and Muller 2010; Jalonen et al. 2015).

In addition, the radial-band sampling approach divides the point cloud into concentric slices with equal distance to the scanner. This ensures that points within each band are sampled at comparable scanner distances, reducing distance-dependent sampling bias compared to rectangular slicing approaches where point distance varies across the sampling unit (Dunlop et al. 2025). Finally, instead of applying a uniform scan radius (e.g., the 10 m threshold used by Dunlop et al. (2025)), the reliability framework introduced here determines a stand-specific reliability distance based on tree detectability, azimuthal coverage, point density, and vertical sampling adequacy. This approach prevents both underestimation of vegetation structure in dense stands and unnecessary exclusion of valid data in more open forests.

4.4. Limitations and Future Research

Several limitations should be acknowledged. Although reliability thresholds were applied, single-scan TLS acquisitions remain sensitive to occlusion effects, particularly in dense vegetation where line-of-sight limitations restrict sampling of vegetation elements. Multi-scan acquisitions could reduce these limitations and provide a more complete structural representation of complex stands, although further research is needed to determine whether this improved structural representation translates into more accurate attenuation predictions. In addition, frontal surface area validation was limited to measurements at a single reference height, leaving uncertainty in the reconstruction of upper-canopy structure, where branching complexity increases. Furthermore, the reliability framework used in this study defined the usable TLS range as the minimum distance across four reliability criteria (tree detectability, azimuthal coverage, point density, and vertical resolution ΔZ). As a result, the most restrictive criterion determines the final reliability distance, making this a conservative estimate of the spatial domain used for structural reconstruction. While this approach ensures that derived vegetation profiles are based on well-sampled regions of the point cloud, it may exclude parts of the scan that still contain usable structural information. Future work could therefore explore whether including a larger portion of the TLS scan influences reconstructed vegetation profiles and whether such differences propagate into wave attenuation predictions.

The modelling framework also treated percentile vegetation profiles as alternative stand scenarios rather than representing the spatial sequence of dense and sparse vegetation patches along a transect. In reality, waves travelling through heterogeneous forests interact with a series of local structural conditions rather than a single vegetation profile. An additional implication of this approach is that the lower-percentile wave attenuation can remain close to zero even as forest width increases, because the lower-percentile vegetation profiles represent persistent structural gaps. In reality, however, the probability that waves propagate entirely through open gaps decreases with increasing forest width, as waves are increasingly likely to

intersect vegetation patches along their path. Consequently, the attenuation variance predicted here likely represents an upper bound, with real forests expected to exhibit decreasing variability as forest width increases, consistent with observations from mangrove wave attenuation studies (Wesenbeeck et al. 2025). Future work should therefore explore stochastic or two-dimensional modelling approaches in which subplot-derived vegetation profiles are distributed spatially across the computational grid, rather than representing the forest with a single percentile profile (e.g., P10 or P90). This would allow wave attenuation in spatially heterogeneous forests to be represented more realistically.

Finally, the drag formulation used in this study was derived from flume experiments conducted on pollarded willows (van Wesenbeeck et al. 2022; Kalloe et al. 2022). While this allowed the influence of vegetation geometry to be isolated, species-specific mechanical properties such as stem rigidity and reconfiguration may influence effective drag coefficients in natural forests. Future work should therefore integrate TLS-derived vegetation geometry with species-specific mechanical parameters to improve vegetation–wave interaction models (van Starrenburg, van Ijzerloo, et al. 2025).

4.5. Implications for Nature-Based Flood Defence Design

The findings of this study have important implications for the use of riparian forests as nature-based flood defences. Vegetation structure influences both the magnitude and variability of wave attenuation. Homogeneous stands with dense lower-canopy structure produced relatively consistent attenuation responses, whereas heterogeneous stands showed substantially wider attenuation ranges. Waves can propagate through longitudinal inter-stem gaps, allowing wave energy to persist over longer distances within structurally heterogeneous forests. This behaviour provides a mechanistic explanation for the finding reported by van Starrenburg, Mancheño, et al. (2026) that structurally diverse natural forests may require substantially greater width than managed pollard forests to achieve comparable wave reduction. Part of this variability may also reflect differences in forest development and management history. Managed riparian forests often consist of relatively uniform pioneer species or pollarded stands that maintain dense, low-canopy structure through regular cutting. In contrast, older, naturally developing floodplain forests typically exhibit mixed-species composition and greater structural heterogeneity, which can produce a wider range of local vegetation configurations and therefore more variable attenuation responses.

From a management perspective, this highlights a trade-off between hydraulic efficiency and ecological complexity, as managed pollarded or young pioneer forests may provide more predictable attenuation, while naturally developed forests offer greater structural diversity and ecological value. Management practices that control vegetation development therefore directly influence forest structure and, consequently, the hydraulic performance of riparian forests used for wave attenuation. In many regulated floodplains vegetation is periodically removed or cut to maintain conveyance capacity, which can promote the continued regeneration of pioneer vegetation and prevent forests from developing into more structurally complex stands (Rowiński et al. 2018). Such management decisions should therefore be considered when evaluating riparian forests as nature-based flood defences.

By linking reliability-filtered TLS-derived vegetation structure to depth-dependent wave attenuation modelling, this study provides a quantitative framework for evaluating how structural variability in riparian forests influences wave attenuation and flood protection potential.

5. Conclusion

This study shows that vertical vegetation structure and horizontal patchiness govern wave attenuation in riparian floodplain forests in fundamentally different ways. Vertical structure determines attenuation magnitude, while horizontal patchiness determines its variability.

Pioneer and managed stands, with dense low-canopy structure and limited patchiness, produced a median attenuation of approximately 40%, with attenuation typically ranging from approximately 20–55% over a forest width of 100 m, and exhibited relatively consistent attenuation responses. Late-successional stands, with vertically distributed structure and pronounced patchiness, produced a lower median attenuation of approximately 20%, with substantially greater variability in attenuation outcomes, ranging from approximately 5–55%. Critically, these differences were condition-dependent: as water level and wave forcing increase, the part of the vegetation profile contributing most to drag shifts. Wave attenuation is therefore not a fixed property of forest structure but emerges from the interaction between vegetation geometry and hydrodynamic forcing.

Horizontal patchiness introduced attenuation uncertainty that uniform vegetation representations cannot capture. In heterogeneous stands, waves propagating through the spaces between stems can persist with little dissipation, meaning that structurally diverse forests may require substantially greater width than managed stands to achieve comparable and reliable wave reduction.

TLS-derived frontal surface area profiles enabled a more realistic representation of vegetation structure than simplified vegetation parameterisations. Restricting analysis to scan-specific reliability domains and applying structure-dependent voxel reconstruction reduced bias in derived profiles and enabled robust structural comparison across structurally contrasting forest stands.

Together, these findings provide a quantitative framework for evaluating structurally diverse riparian forests as nature-based flood defences. Realistic flood risk assessments therefore require vegetation representations that account for both vertical vegetation structure and variability within forest stands, rather than uniform vegetation parameterisations. Simplifying forests to a single homogeneous vegetation layer produces a single deterministic attenuation estimate, whereas incorporating structural variability captures the range of wave attenuation responses observed in natural forests.

A. Field Measurement Data

The tables in this appendix summarise the manual field measurements used to validate TLS-derived frontal surface area (FSA) estimates and to characterise subplot-scale woody structure. Measurements were conducted within 1 × 1 m subplots at the two study sites, Visserijgrienden and Millingerwaard, and included stem circumference, branch counts by diameter class, and derived frontal surface area values.

FSA was calculated as the projected width of woody elements intersecting a vertical slice of 10 cm thickness. Stem diameters were derived from measured circumferences assuming circular cross-sections. For branch measurements, counts were grouped into diameter classes, and measured diameters were used as described in the individual table notes. Differences in vegetation structure, such as pollarded willows, multi-stem trees, fallen stems, and resprouted branches, are reflected in the structure of the tables presented in this appendix.

These measurements were also used for the evaluation of structural relationships between woody element density and frontal surface area (Figure 34a). Furthermore, the hand measurements served as validation and parameter calibration data for the comparison with frontal surface area reconstructed from TLS data (Figure 17).

A.1. Millingerwaard

Table 3: Summary of hand measurements for five 1 × 1 m subplots in plot 1 (right side), Millingerwaard. Branch counts are grouped by diameter classes (D1 50–80 mm, D2 20–50 mm, D3 < 20 mm). Frontal surface area (FSA) is calculated for a vertical slice thickness of 10 cm.

		D1 (50–80 mm)		D2 (20–50 mm)		D3 (< 20 mm)	
Subplot ID	Species	#D1	D_{max} (mm)	#D2	D_{max} (mm)	#D3	FSA at 1.0 m (cm^2)
T1	Young Willow	–	–	2	30	27	321.0
T2	Young Willow	–	–	1	35	10	135.0
T3	Young Willow	–	–	–	–	30	307.0
T4	Young Willow	–	–	2	23	16	205.0
T5	Young Willow	2	75	2	43	43	643.1

Elliptical branch diameter (T5) was converted using $d_{\text{eff}} = \sqrt{d_1 d_2}$ prior to FSA computation.

Table 4: Summary of hand measurements for five 1 × 1 m subplots in plot 1 (left side), Millingerwaard. Branch counts are grouped by diameter classes (D1 50–80 mm, D2 20–50 mm, D3 < 20 mm). Frontal surface area (FSA) is calculated for a vertical slice thickness of 10 cm.

		D1 (50–80 mm)		D2 (20–50 mm)		D3 (< 20 mm)	
Subplot ID	Species	#D1	D_{max} (mm)	#D2	D_{max} (mm)	#D3	FSA at 1.0 m (cm^2)
T1	Young Willow	–	–	1	36	8	116.0
T2	Young Willow	1	62	3	28	10	236.0
T3	Young Willow	1	52	1	45	12	217.0
T4	Young Willow	–	–	1	30	21	240.0
T5	Young Willow	1	51	1	39	7	160.0

Table 6: Summary of hand measurements for five 1 × 1 m subplots in plot 3, Millingerwaard. Stem circumference and derived frontal surface area (FSA) were measured at two heights. FSA is calculated for a vertical slice thickness of 10 cm.

Subplot ID	Species	Stem circ. at 0.7 m (cm)	FSA at 0.7 m (cm^2)	Stem circ. at 1.0 m (cm)	FSA at 1.0 m (cm^2)
T1	Oak	292	929.9	275	875.3
T2	Oak	256	814.9	242	770.3
T3	Elm	398	1267.2	388	1235.1
T4	Elm	520	1655.2	530	1687.4
T5	Elm	367	1168.0	393	1251.3

Table 8: Summary of hand measurements for seven 1 × 1 m subplots in plot 5, Millingerwaard. Stem circumference and derived frontal surface area (FSA) were measured at two heights. FSA is calculated for a vertical slice thickness of 10 cm.

Subplot ID	Species	Stem circ. at 0.7 m (cm)	FSA at 0.7 m (cm^2)	Stem circ. at 1.0 m (cm)	#D3	FSA at 1.0 m (cm^2)
T1	Mature Willow	57	181.4	50	6	189.2
T2	Mature Willow	60	191.0	57	–	181.4
T3	Mature Willow	71	226.0	65	–	206.9
T4	Mature Willow	57	181.4	60	11	246.0
T5	Mature Willow	43	136.9	39	1	129.1

D3 branches were only present in the 1.0 m FSA.

A.2. Visserijgrienden

Table 9: Summary of hand measurements for five 1 × 1 m subplots in plot 1, Visserijgrienden. Stem circumference was measured at 0.7 m height and used to derive stem diameter and frontal surface area (FSA). FSA is calculated for a vertical slice thickness of 10 cm.

Subplot ID	Species	Stem circ. at 0.7 m (cm)	Stem diam. at 0.7 (cm)	FSA at 0.7 m (cm^2)
T1	Pollarded Willow	27.0	8.6	85.9
T2	Pollarded Willow	40.1	12.8	127.7
T3	Pollarded Willow	60.0	19.1	191.0
T4	Pollarded Willow	46.0	14.7	146.5
T5	Pollarded Willow	78.0	24.8	248.4

Table 10: Summary of hand measurements for five 1 × 1 m subplots in plot 1, Visserijgrienden. Branch counts were recorded at the height of the first branch (H_1) and grouped by diameter classes (D1 50–80 mm, D2 20–50 mm, D3 < 20 mm). Frontal surface area (FSA) is calculated for a vertical slice thickness of 10 cm.

		D1 (50–80 mm)		D2 (20–50 mm)	D3 (< 20 mm)	
Subplot ID	Species	#D1	D_{max} (mm)	#D2	#D3	FSA at H_1 (cm^2)
T1	Pollarded Willow	110	1	4	28	472.0
T2	Pollarded Willow	120	2	6	39	742.0
T3	Pollarded Willow	125	5	8	85	1505.0
T4	Pollarded Willow	90	–	5	16	335.0
T5	Pollarded Willow	120	1	6	80	1071.0

Table 11: Summary of hand measurements for five 1 × 1 m subplots in plot 1, Visserijgrienden. Circumference of the main knot was measured. FSA is calculated for a vertical slice thickness of 10 cm.

Subplot ID	Species	Knot circ. (cm)	Knot diam. (cm)	FSA at knot (cm^2)
T1	Pollarded Willow	60	19.1	191.0
T2	Pollarded Willow	101	32.2	321.5
T3	Pollarded Willow	128	40.8	407.5
T4	Pollarded Willow	58	18.5	184.6
T5	Pollarded Willow	130	41.4	413.8

Table 12: Summary of hand measurements for five 1 × 1 m subplots in plot 4, Visserijgrienden. Branch counts are grouped by diameter classes (D1 50–80 mm, D2 20–50 mm, D3 < 20 mm). Frontal surface area (FSA) is calculated for a vertical slice thickness of 10 cm.

		D1 (50–80 mm)		D2 (20–50 mm)	D3 (< 20 mm)	Stem	
Subplot ID	Species	#D1	D_{max} (mm)	#D2	#D3	Circ. at 1.0 m (cm)	FSA at 1.0 m (cm^2)
T1	Hawthorn	1	72	4	5	–	262.0
T2	Hawthorn	–	–	–	–	46	146.0
T3	Hawthorn	2	76	1	10	–	287.0
T4	Mature Willow	–	–	–	–	63	201.0
T5	Robinia	–	–	–	–	204	650.0

Table 15: Summary of hand measurements for four 1 × 1 m subplots in plot 7, Visserijgrienden. Branch counts are grouped by diameter classes (D1 50–80 mm, D2 20–50 mm, D3 < 20 mm). Frontal surface area (FSA) is calculated for a vertical slice thickness of 10 cm.

		D1 (50–80 mm)		D2 (20–50 mm)	D3 (< 20 mm)	Stem	
Subplot ID	Species	#D1	D_{max} (mm)	#D2	#D3	Circ. at 1.0 m (cm)	FSA at 1.0 m (cm^2)
T1	Mature Willow	–	–	–	–	230	732
T2	Fallen Willow	2	77	1	2	–	192
T3	Young Willow	1	56	–	5	–	106
T4	Mature Willow	–	–	–	–	90	286

Table 16: Summary of hand measurements for fallen trees T5 and T6 in 1 × 1 m subplots of plot 7, Visserijgrienden. Frontal surface area (FSA) is calculated for a 10 cm slice.

Tree ID	Species	Height (m)	Element	Diameters (cm)	FSA (cm^2)
T6	Mature Willow	0.4	Fallen stem	36.9	369.4
T6	Mature Willow	0.4	Resprouted branches	12.7	167.3a
T6	Mature Willow	1.0	Fallen stem	24.2	241.9
T6	Mature Willow	1.0	Resprouted branches	5.9, 3.8, 3.5, 1.4	146.0
T5	Fallen Willow	1.0	Fallen stem	19.4	194.1

For T6 at 0.4 m, the branch FSA includes four additional D3 branches.

B. Additional Forest Structural Characterisation

Following the derivation of vertically resolved frontal surface area density profiles a(z), additional structural metrics were quantified within the reliability distance, besides the tree shape similarity and the horizontal patchiness.

B.1. Horizontal structural variability

Horizontal structural variability was quantified within the stem height band (0.7–1.8 m). Vegetation cover was calculated from a top-view projection as the fraction of occupied vegetation area relative to the total circular ground area defined by the reliability distance (Figure 24). To assess spatial heterogeneity, the circular domain was subdivided into four equal-area quadrants. Vegetation cover was calculated separately for each quadrant, and the coefficient of variation (CV) of quadrant-level vegetation cover was used as an indicator of horizontal structural heterogeneity.

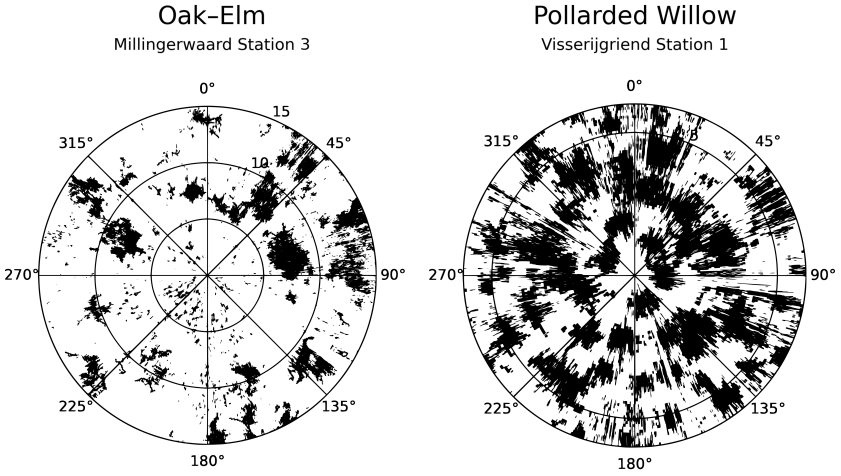

Figure 24: Example top-view projections of vegetation within the stem height band (0.7–1.8 m) for an Oak–Elm and a Pollarded Willow plot, illustrating contrasting horizontal vegetation cover and spatial variability.

Vegetation cover fraction and spatial variability (CV across quadrants) exhibited a clear inverse relationship across forest plots (Figure 25). Plots dominated by Oak–Elm and Willow–Ash showed low vegetation cover (≤ 0.10) combined with high spatial variability (CV $\geq$ 0.55). These plots occupy the upper-left region of the cover–variability space, indicating sparse and heterogeneous spatial distributions of vegetation within the stem height band. This pattern is illustrated in Figure 24, which shows the contrasting horizontal vegetation distributions of an Oak–Elm and a Pollarded Willow plot.

In contrast, Pollarded Willow, Young Willow, and Hawthorn plots exhibited substantially higher vegetation cover (0.45–0.52) and low spatial variability (CV $\approx$ 0.08–0.13). These plots cluster in the lower-right region of the figure, reflecting dense and spatially homogeneous vegetation cover.

Mature Willow plots occupied intermediate positions, with vegetation cover fractions between 0.15 and 0.38 and CV values ranging from 0.15 to 0.40. This indicates moderate vegetation cover combined with intermediate levels of spatial heterogeneity, reflecting the diverse structures found in mature willow stands, including fallen stems, resprouted trunks, and branching vegetation.

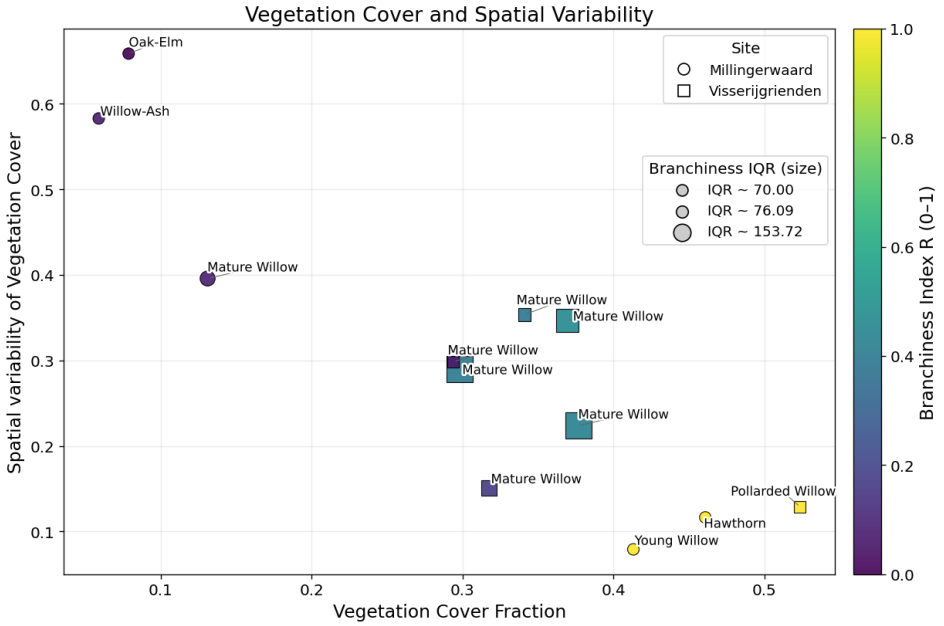

Figure 25: Vegetation cover fraction (0.7–1.8 m stem height band) versus horizontal spatial variability (coefficient of variation of quadrant-level vegetation cover) for all forest stands within their reliability distance. Marker colour indicates the mean Branchiness Index and marker size represents branchiness variability (IQR).

Across all plots, vegetation cover fraction and spatial variability were strongly negatively related, indicating a structural gradient from sparse and heterogeneous vegetation (Oak–Elm and Willow–Ash) to dense and homogeneous vegetation (Pollarded Willow, Young Willow, and Hawthorn). Together, these TLS-derived metrics clearly differentiate forest structural patterns within the reliability distance.

B.2. Vertical structural variability

Vertical variability of forest structure was evaluated using the computed $a(z)$ profiles. The cumulative $a(z)$ distribution was used to derive characteristic height percentiles z_{10}, z_{50}, and z_{90}, defined as the heights at which 10%, 50%, and 90% of the cumulative frontal surface area density were reached.

The difference between z_{90} and z_{10} ($z_{90}-z_{10}$) was defined as the vertical extent, representing the vertical spread of vegetation structure. The median height z_{50} was used to describe whether frontal surface area was concentrated in lower or higher vegetation layers.

Total frontal surface area per unit ground area was obtained by integrating $a(z)$ over height. In addition, frontal surface area within the stem height band (0.7–1.8 m) was computed for the stem-band fraction.

$$\text{Stem-band fraction} = \frac{FSA_{\text{stem}}}{FSA_{\text{total}}}. \tag{25}$$

Together, FSA_{total}, z_{50}, $z_{90} - z_{10}$, and the stem-band fraction provide descriptors of structural magnitude and vertical positioning of vegetation within each TLS plot. Relationships among these metrics were analysed to characterise differences in vertical vegetation structure between plots.

Total frontal surface area showed no consistent relationship with woody element density (Figure 26A). Subplots with contrasting densities achieved similar frontal surface area values.

Plots characterised by large stem sizes, such as Oak–Elm, reached high frontal surface area, whereas plots dominated by smaller stems exhibited lower values.

In contrast, median frontal-area height (z_{50}) decreased with increasing woody element density (Figure 26B), indicating that higher densities correspond to a greater concentration of vegetation in lower layers. Mature willow plots showed a variation in z_{50} for similar woody element densities, reflecting the structural diversity characteristic of mature willow stands.

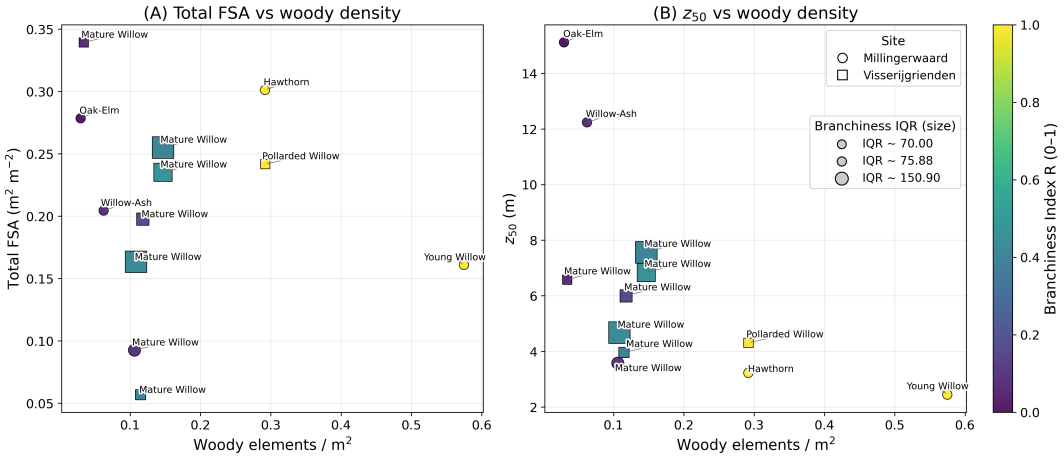

Figure 26: Relationships between woody density and A) structural magnitude and B) vertical positioning.

Together, these results indicate that woody element density influences vertical vegetation structure but does not predict FSA_{total}. The magnitude of frontal area is more dependent on the size of individual woody elements, such as the stem diameter.

Stem-band fraction decreased with increasing vertical extent ($z_{90} - z_{10}$) (Figure 27). Forest stands with larger vertical extents allocated a smaller proportion of frontal area to the stem-height band.

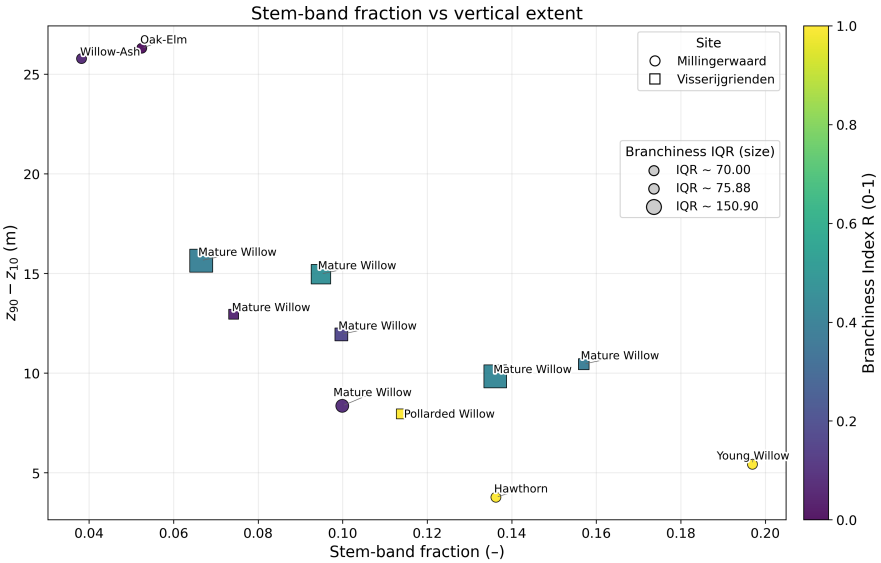

Figure 27: Stem-band fraction as a function of vertical extent ($z_{90} - z_{10}$).

Mature Willow plots spanned the widest range along this gradient, from compact configurations with high stem-band fractions to vertically extended structures with reduced stem-band

contribution. In contrast, Pollarded Willow, Young Willow, and Hawthorn plots clustered at higher stem-band fractions and lower vertical extents, reflecting stronger structural dominance within lower vegetation layers.

These results demonstrate that TLS-derived metrics capture vertical vegetation structure effectively, revealing clear differences in structural magnitude and the vertical concentration of vegetation structure among forest stands.

C. SWAN Model Validation

Model performance was evaluated by reproducing the large-scale flume experiments of van Wesenbeeck et al. (2022). In these experiments, real pollarded willow trees were placed in the flume and wave attenuation across the vegetated section was measured under controlled hydrodynamic conditions. The structural properties of the trees used in the flume were measured and reconstructed as vertical frontal surface area density profiles $a(z)$. To validate the modelling approach used in this study, the SWAN model was configured using the same flume geometry, reconstructed vegetation profiles, and hydrodynamic conditions as used in the van Wesenbeeck et al. (2022) study. The simulated wave attenuation was then compared with the attenuation measured in the flume.

Simulations were performed for the wave conditions listed in Table 19. The test cases correspond to three experimental series representing different vegetation configurations: test series 2 represents a canopy with leaves, test series 3 the same canopy without leaves, and test series 4 a reduced canopy without leaves with approximately 50% branch density. Figure 28 shows the comparison between measured and simulated wave attenuation for test series 2 and 3, while Figure 29 presents the comparison for test series 4.

The SWAN simulations reproduce the magnitude and trends of the measured wave attenuation across the tested conditions. This agreement confirms that the model configuration provides a reliable representation of vegetation-induced wave dissipation. After this validation step, the same modelling setup was used to simulate wave attenuation through the structurally diverse floodplain forests characterised in this study using TLS-derived vegetation structure.

Table 19: Hydrodynamic conditions of validation simulations reproducing the flume experiments of van Wesenbeeck et al. (2022).

Test	Series	$H_{m0,i}$ (m)	T_p (s)	h (m)
T005	2	0.49	2.84	3.0
T006	2	1.01	3.8	3.0
T007	2	0.52	3.7	3.0
T008	2	1.07	5.3	3.0
T013	3	0.46	2.7	3.0
T014	3	0.95	3.7	3.0
T015	3	0.49	3.7	3.0
T016	3	0.99	5.3	3.0
T021	3	1.41	4.8	4.5
T022	3	1.47	6.5	4.5
T023	4	0.49	2.7	3.0
T024	4	0.98	3.6	3.0
T025	4	0.50	3.8	3.0
T026	4	1.03	5.3	3.0
T029	4	1.45	4.9	4.5
T030	4	1.51	6.8	4.5

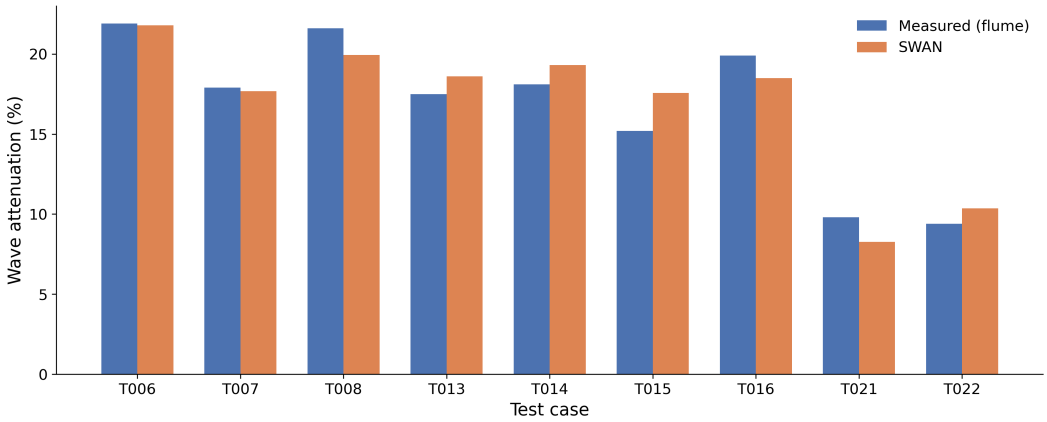

Figure 28: Comparison between measured wave attenuation in the flume experiments and SWAN-simulated attenuation for validation cases from test series 2 (canopy with leaves) and test series 3 (canopy without leaves).

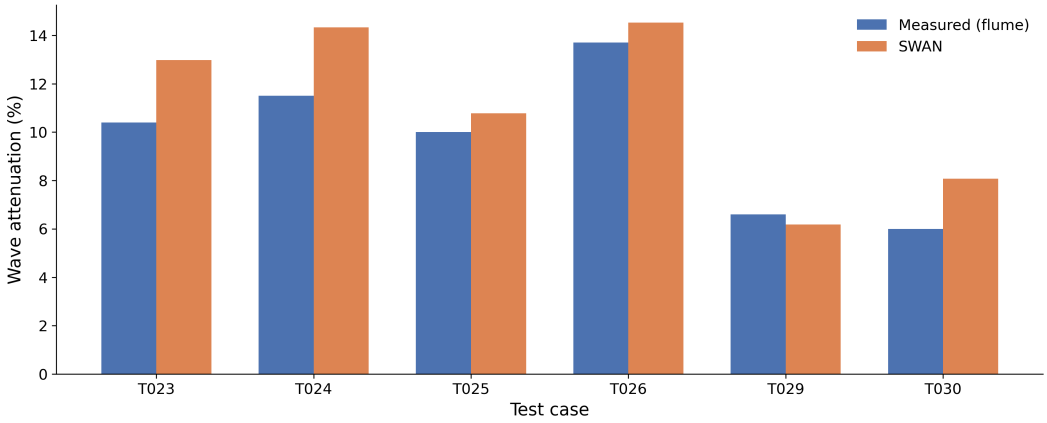

Figure 29: Comparison between measured and SWAN-simulated wave attenuation for validation cases from test series 4 (canopy without leaves, with approximately 50% branch density).

D. Sensitivity Analysis of TLS-Derived Vegetation Profiles

A sensitivity analysis was conducted to evaluate the influence of parameter choices on the derived vertical frontal surface area density profiles $a(z)$. The analysis focused on three methodological components: (1) voxel size used in the voxelisation procedure, (2) radial band width used in the stand-level $a(z)$ reconstruction, and (3) the scan-specific reliability distance defining the spatial extent of the TLS.

Parameter ranges were selected relative to the baseline parameterisation used for each vegetation type. For stands with fine branch structure (young willow, pollarded willow, and hawthorn), the baseline voxel size was $v = 0.011$ m, with sensitivity tests performed using $v = 0.01$ m and $v = 0.025$ m. For mature willow stands, the baseline voxel size was $v = 0.015$ m, with sensitivity evaluated using $v = 0.01$ m and $v = 0.025$ m. For more open stands with larger stem sizes (oak–elm and willow–ash), the baseline voxel size was $v = 0.03$ m, with sensitivity tests using $v = 0.015$ m and $v = 0.05$ m. Radial band width was evaluated using a baseline value of 1 m, with sensitivity tests conducted using 0.5 m and 1.5 m bands. Sensitivity to reliability distance was assessed by scaling the scan-specific reliability distance by factors of 0.8 and 1.2, representing moderate reductions and extensions of the spatial domain used for vegetation reconstruction.

Figures 30A–33 illustrate the sensitivity results for all forest stands. Across all stands, the vertical shape of the $a(z)$ profiles remained largely consistent across parameter settings, while the magnitude of $a(z)$ showed moderate variation. The largest sensitivity was generally observed in denser forest stands (young willow, pollarded willow, and hawthorn), where point density decreases with distance and occlusion effects are strongest. In contrast, more open forest stands such as the oak–elm and willow–ash showed smaller sensitivity ranges due to reduced occlusion.

The sensitivity analysis indicates that voxel size exerts the strongest influence on the magnitude of the reconstructed $a(z)$ profiles (Figures 30A–33A). Across all analysed stands, increasing voxel size consistently increased $a(z)$, while decreasing voxel size reduced the reconstructed frontal surface area. A larger voxel size means that each point is represented by a larger voxel area, resulting in a larger reconstructed frontal surface area.

Increasing radial band width generally resulted in a reduction of $a(z)$ across stands (Figures 30B–33B). Wider bands increase foreground occlusion within the band, resulting in reduced representation of background vegetation. When normalised by the ground area, this leads to lower reconstructed values.

The sensitivity to reliability distance depended on vegetation structure (Figures 30C–33C). In denser stands such as young willow, hawthorn, pollarded willow, and several mature willow stands, increasing the reliability distance generally reduced $a(z)$ (Figure 32C). This suggests that vegetation further from the scanner was less completely represented due to occlusion and lower point density. In contrast, more open stands such as oak–elm and willow–ash showed limited sensitivity to reliability distance, indicating that the selected reliability distance may be conservative in these cases (Figure 33C). Across all stands, decreasing the reliability distance resulted in only minor or no increases in $a(z)$, indicating that the chosen reliability distances capture vegetation structure with representative magnitude and do not strongly bias the profiles toward underestimation.

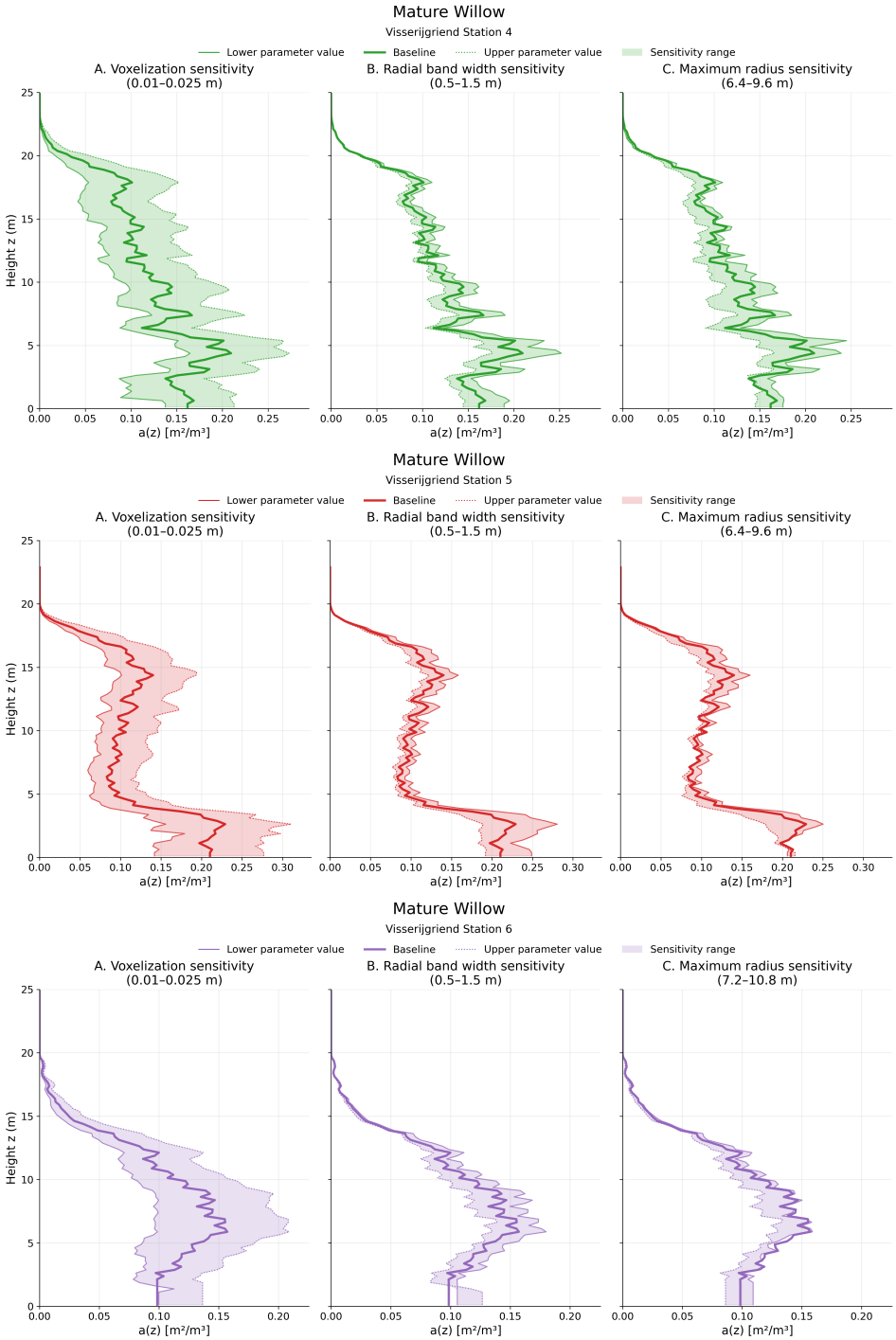

Figure 30: Sensitivity of TLS-derived vertical frontal surface area density profiles $a(z)$ to parameter choices for more complex and dense mature willows. Panels within each station figure show the effect of (A) voxel size, (B) radial band width, and (C) reliability distance on reconstructed $a(z)$ profiles. The solid line represents the baseline parameter configuration used in the main analysis, while thin lines indicate profiles derived using lower and upper parameter values. Shaded regions show the resulting sensitivity range.

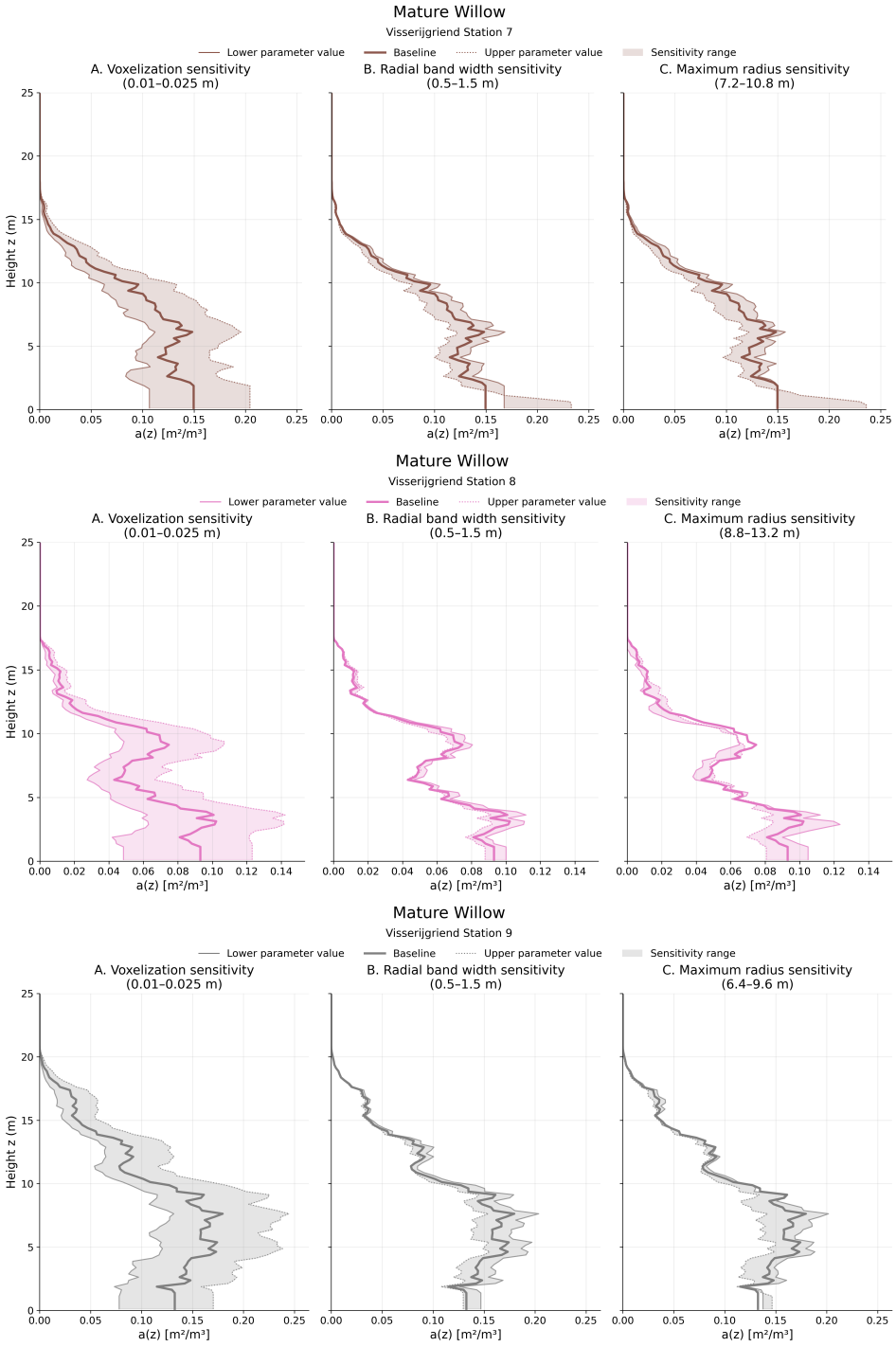

Figure 31: Sensitivity of TLS-derived vertical frontal surface area density profiles $a(z)$ to parameter choices for more complex and dense mature willows. Panels within each station figure show the effect of (A) voxel size, (B) radial band width, and (C) reliability distance on reconstructed $a(z)$ profiles. The solid line represents the baseline parameter configuration used in the main analysis, while thin lines indicate profiles derived using lower and upper parameter values. Shaded regions show the resulting sensitivity range.

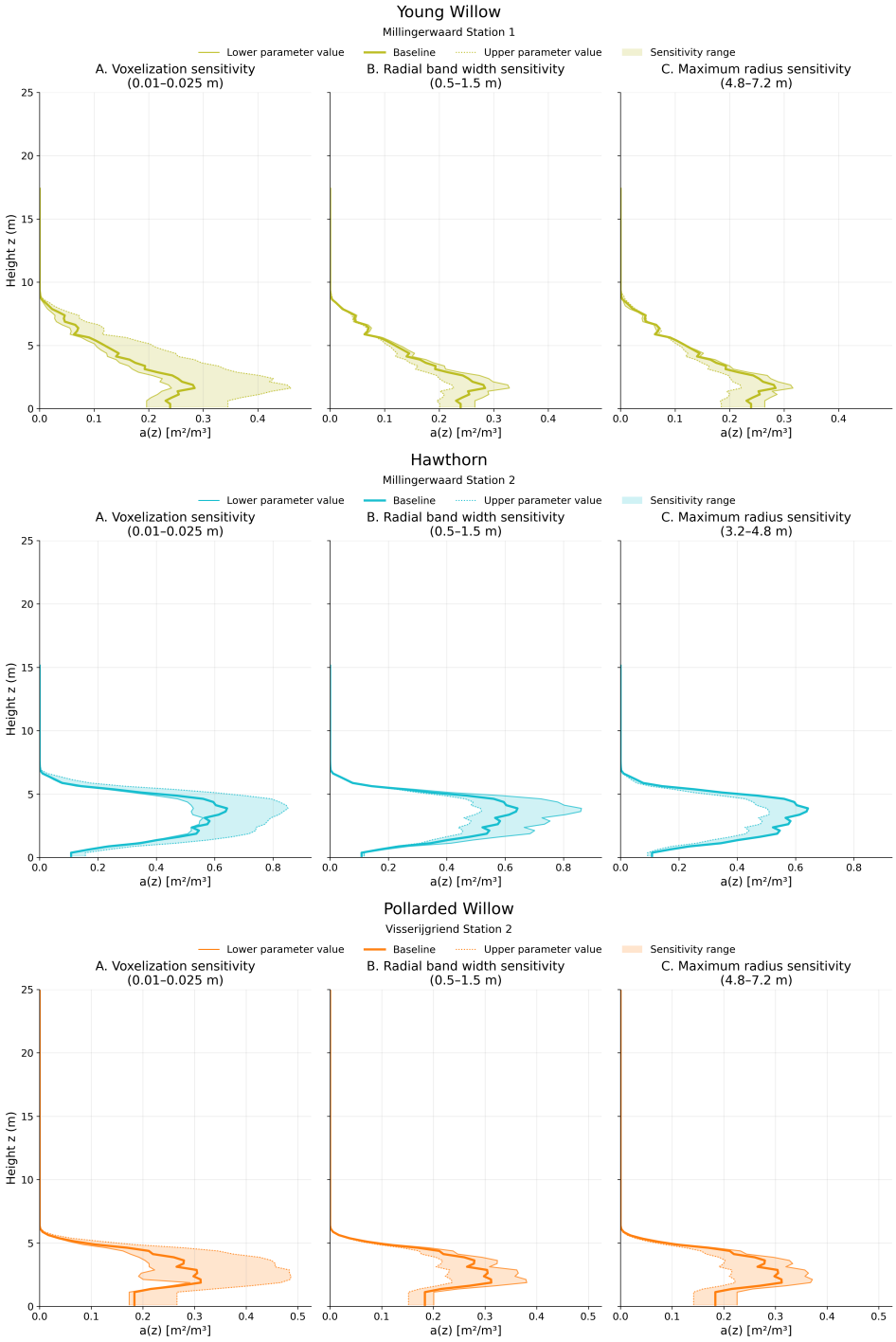

Figure 32: Sensitivity of TLS-derived vertical frontal surface area density profiles $a(z)$ to parameter choices for fine-branch stands (young willow, pollarded willow, and hawthorn). Panels show the effect of (A) voxel size, (B) radial band width, and (C) reliability distance on reconstructed $a(z)$ profiles. The solid line indicates the baseline parameter configuration, while thin lines and shaded regions show the sensitivity range.

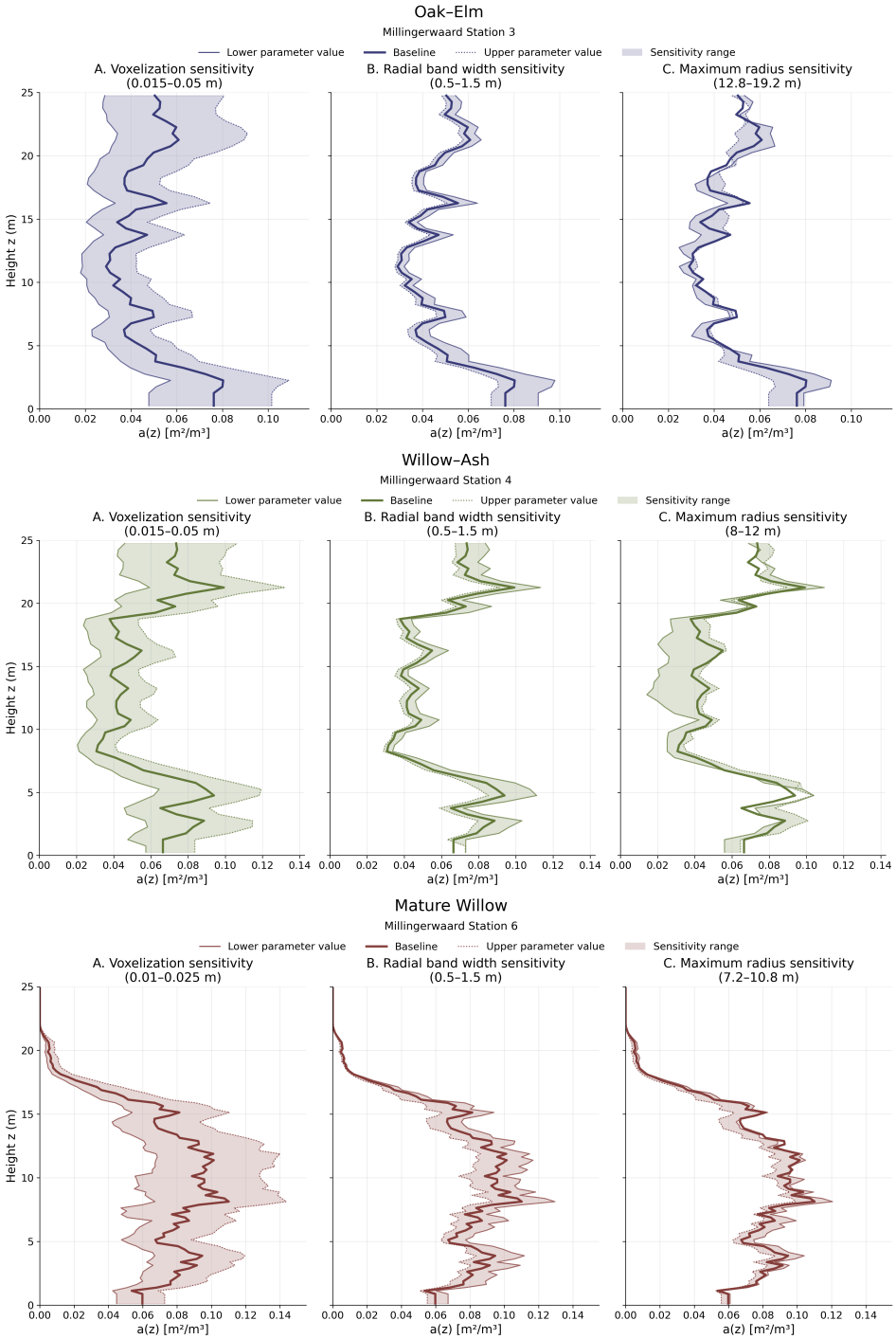

Figure 33: Sensitivity of TLS-derived vertical frontal surface area density profiles $a(z)$ to parameter choices for Oak–Elm, Willow–Ash, and more open mature willow stands. Panels show the effect of (A) voxel size, (B) radial band width, and (C) reliability distance on reconstructed $a(z)$ profiles. The solid line indicates the baseline parameter configuration, while thin lines and shaded regions show the sensitivity range.

E. Structural Classification of Forest Stands

E.1. Forest Structure Classification

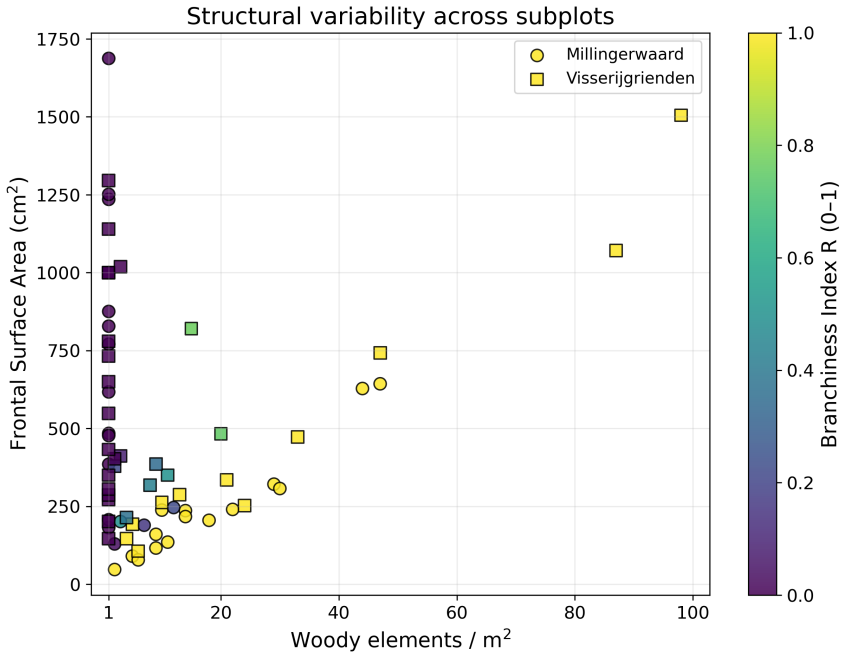

(a) Subplot-level relationship between frontal surface area and woody element density. Each point represents a 1 × 1 m subplot coloured by the Branchiness Index (R).

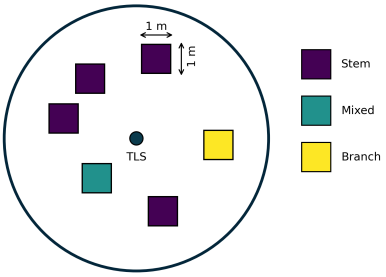

(b) Example of subplot-based structural classification within a forest stand.

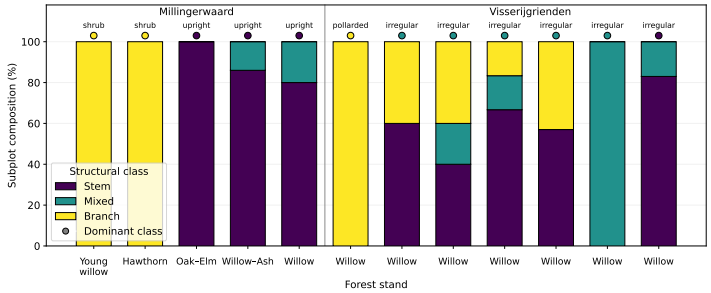

(c) Stand-level structural class composition.

Figure 34: Structural classification of forest plots across subplot and stand scales. (a) Subplot-level variation in frontal surface area (FSA) and woody element density at 1.0 m height. (b) Schematic example of subplot-based structural classification within a TLS plot. (c) Stand-level structural class composition for all forest plots, with structural form annotations (shrub, upright, irregular) indicated above the bars.

An analysis was conducted to investigate whether forest stands could be grouped into discrete structural classes based on the relative contribution of stems and branches to frontal surface area. This classification aimed to simplify the structural diversity observed in the TLS data and to group similar structural patterns observed in both the TLS-derived vegetation metrics and the simulated wave attenuation responses.

However, during the analysis it became evident that such discrete classes obscured important structural variability between forest stands and species. As a result, the classification

was not used in the main analysis of this study. Instead, structural characteristics such as branchiness were used descriptively when interpreting stand structure. The results of the classification analysis are presented here for completeness and to illustrate the structural gradients observed across the study sites. Although the classes were not retained in the final analysis framework, they nevertheless revealed consistent structural similarities between stands with comparable vegetation structure.

Structural class definition The Branchiness Index R quantifies the proportional contribution of branches to the total frontal surface area at 1.0 m height. Based on the distribution of R (Figure 34a), three structural regimes were distinguished:

- **Stem-dominated structure:** $R < 0.2$
- **Mixed structure:** $0.2 \leq R \leq 0.8$
- **Branch-dominated structure:** $R > 0.8$

These classes were used to explore structural variation among subplots and forest stands.

Stand-level classification To evaluate structural composition at the stand scale, the proportion of subplots belonging to each structural class was calculated for each forest stand (Figure 34c). Figure 34b illustrates how structural classes identified at the subplot scale are aggregated to the forest stand scale. A forest stand was assigned a dominant structural class when at least 80% of its subplots fell within the same category. Stands not meeting this threshold were classified as mixed, indicating that the stand contains a combination of stem-, mixed-, and branch-dominated subplots. In addition, the structural form of each forest stand is indicated above the bar plots in Figure 34c, where shrub refers to low-concentration vegetation structure, upright to relatively uniform upright tree structures, and irregular to structurally heterogeneous stands consisting of upright, inclined, and fallen willows.

Structural consistency of vegetation profiles To evaluate whether the structural classes represent distinct vegetation structures, median vertical frontal surface area density profiles $a(z)$ were calculated for the forest stands belonging to each class (Figure 35). Shaded areas indicate the variability within each class.

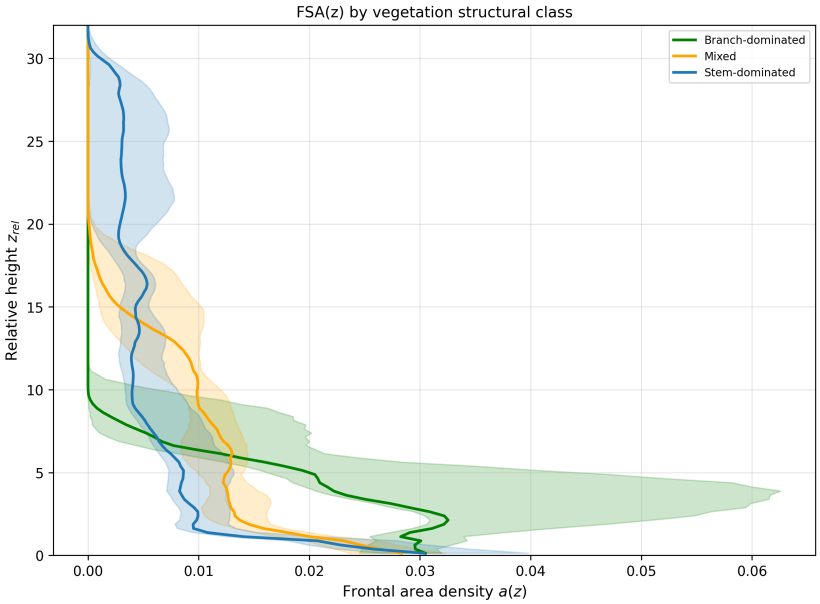

Figure 35: Median vertical frontal area density profiles $FSA(z)$ by vegetation structural class. Solid lines show the class median profile and shaded envelopes denote the interquartile range (25th–75th percentile) across sites within each class.

The profiles show consistent structural differences between the three classes. Branch-dominated subplots exhibit high frontal surface area densities concentrated at low heights, mixed subplots display intermediate profiles, and stem-dominated subplots show relatively low frontal surface area densities throughout the profile. These results indicate that the Branchiness Index corresponds to distinct vertical vegetation structures, supporting the structural interpretation of the classes.

Forest density TLS-derived forest density differed systematically between structural classes (Figure 36). Branch-dominated stands exhibited the highest densities, mixed stands showed intermediate densities, and stem-dominated stands exhibited the lowest densities.

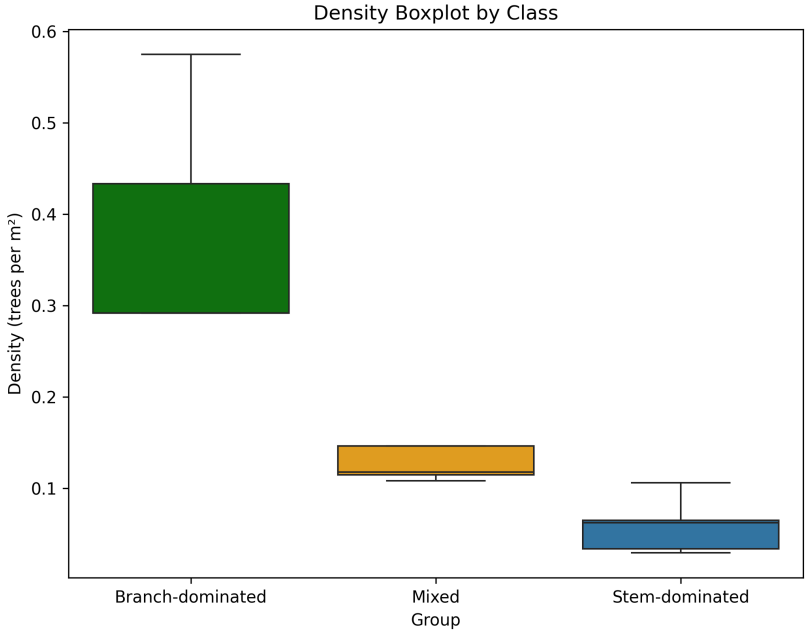

Figure 36: TLS-derived woody element density (trees/m^2) per structural class. Boxes represent the median and interquartile range.

This pattern is consistent with the structural regimes defined by the Branchiness Index: branch-dominated stands are characterised by densely packed woody elements, whereas stem-dominated stands contain fewer, more widely spaced stems. Mixed stands occupy an intermediate position between these two structural extremes.

Reliability distance To further evaluate whether the structural classes correspond to measurable differences in forest structure, the scan-specific reliability distances were compared across branch-, mixed-, and stem-dominated stands (Figure 37).

Reliability distance varied systematically across the structural classes (Figure 37). Branch-dominated stands generally exhibited the smallest reliability distances, reflecting rapid occlusion of the TLS beam within dense and complex vegetation structures. In contrast, stem-dominated stands showed the largest reliability distances, consistent with more open forest structures allowing the laser beam to penetrate further into the stand. Mixed stands occupied an intermediate position between these two structural extremes. These patterns indicate that the structural classes correspond not only to differences in vegetation structure but also to differences in TLS sampling conditions.

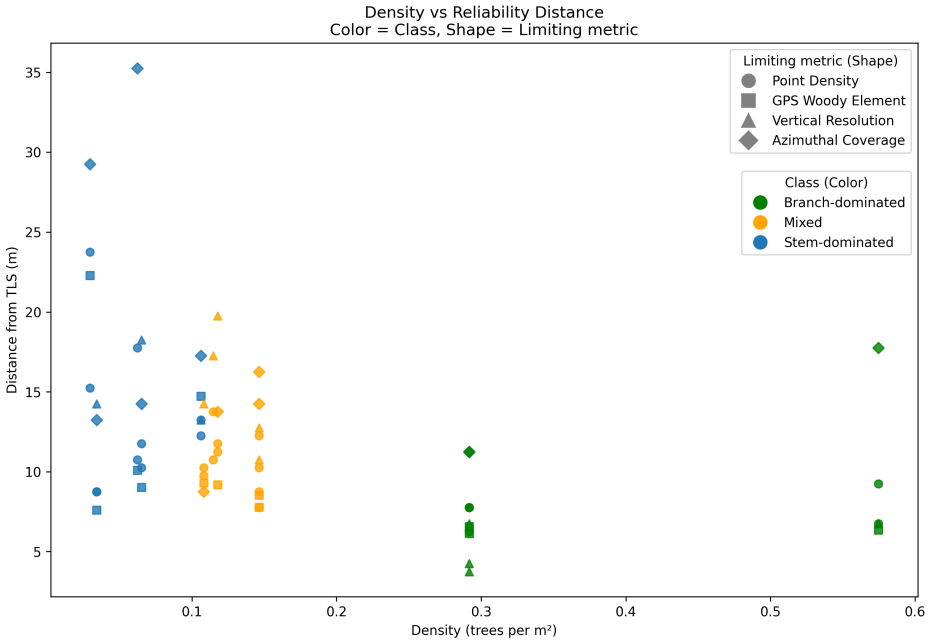

Figure 37: Final reliability distance (d_{reliable}) as a function of TLS-derived woody density.

Interpretation Together, these patterns indicate that the structural classes correspond to consistent differences in vertical vegetation profiles, stand density, and scan reliability conditions. This supports the interpretation that the classes capture meaningful structural gradients in the TLS data.

F. TLS Sampling Resolution Across Scan Stations

To illustrate the spatial sampling characteristics of the TLS data, the vertical sampling resolution (Δz) and point density distribution are shown for all scan stations. Across stations, point density generally decreases with increasing distance from the scanner, while vertical point spacing (Δz) increases due to beam divergence and vegetation occlusion (Figure 38-41). The rate at which these sampling properties change varies between forest types and illustrates the spatial variability in TLS sampling resolution across the study sites.

Young willow, pollarded willow, and hawthorn stands exhibit the fastest decline in point density and the most rapid increase in vertical spacing, consistent with the shorter reliability distances identified for these dense and structurally complex stands (Figure 40). In contrast, oak–elm and willow–ash stands maintain higher point densities and smaller vertical spacing over larger distances, corresponding to the longer reliability distances observed for these more open forest structures (Figure 39). Mature willow stands show intermediate behaviour depending on stand structure.

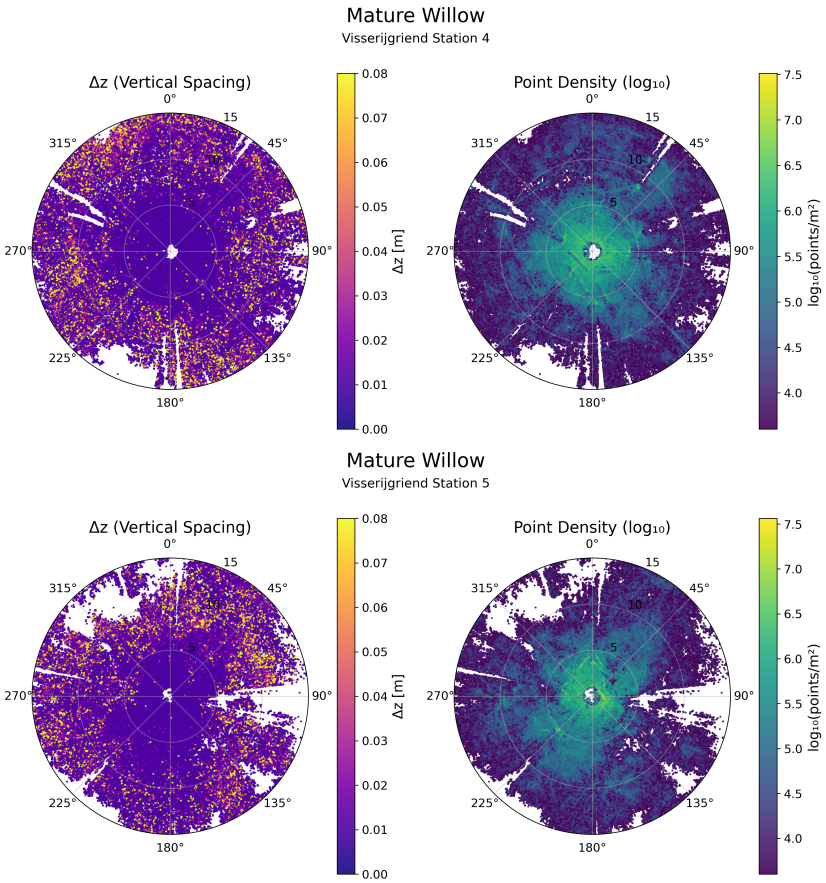

Figure 38: TLS sampling characteristics for mature willow stands. These stands show intermediate behaviour in point density and vertical spacing (Δz), reflecting differences in stand density and structural complexity.

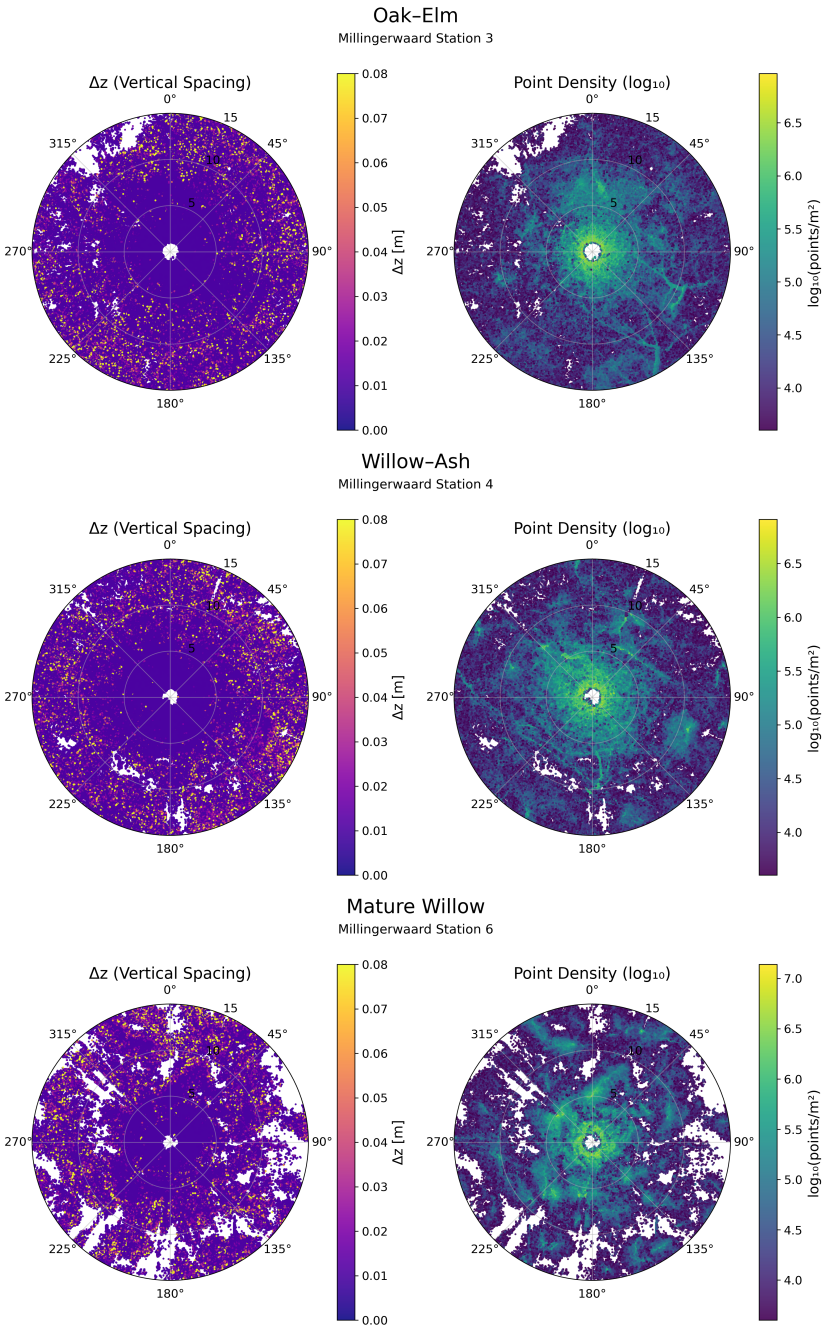

Figure 39: TLS sampling characteristics for open forest stands (Oak–Elm and Willow–Ash). These stands maintain relatively high point densities and small vertical spacing (Δz) over larger distances from the scanner, reflecting the longer reliability distances associated with their more open forest structures.

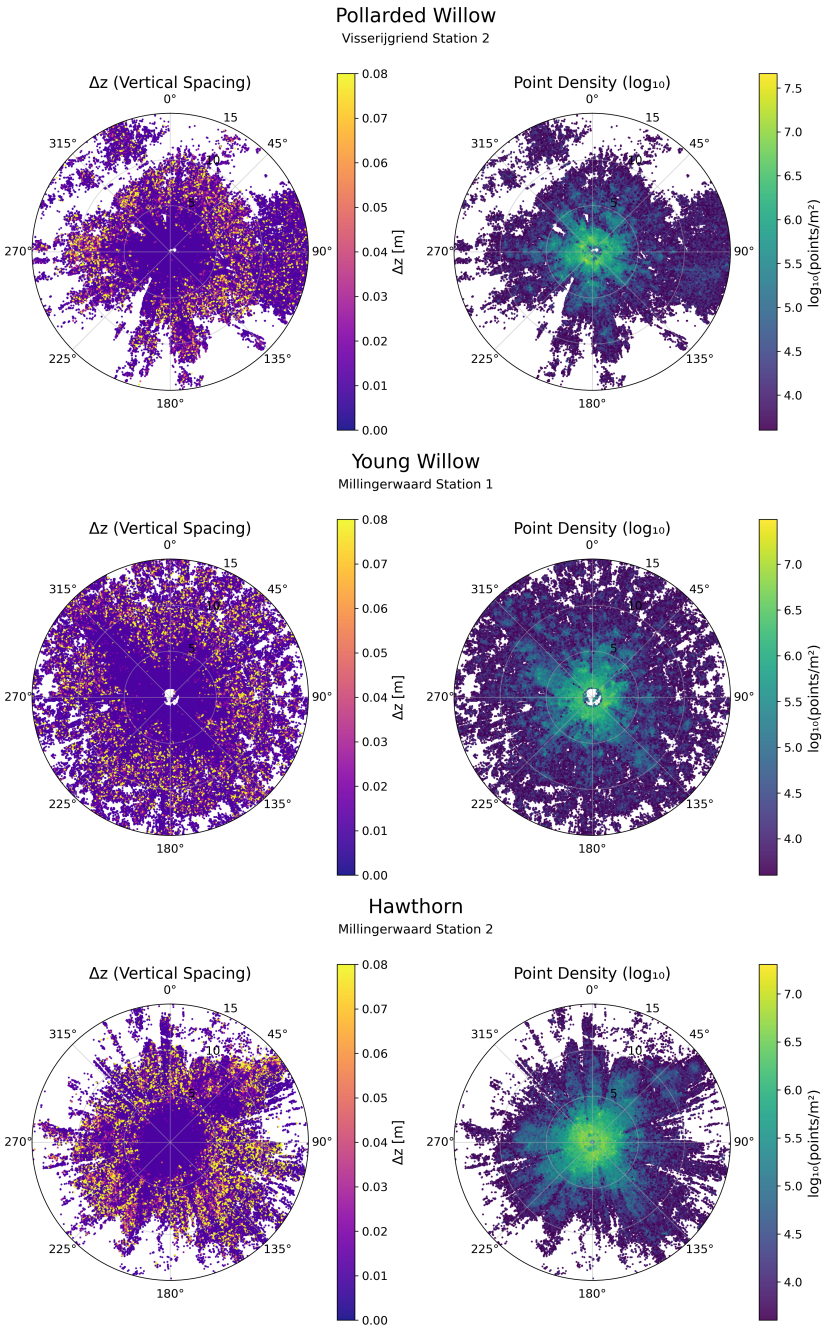

Figure 40: TLS sampling characteristics for dense branch-dominated stands (Young Willow, Pollarded Willow, and Hawthorn). Rapid declines in point density and strong increases in vertical spacing (Δz) with distance indicate fast beam occlusion within dense and structurally complex vegetation, resulting in shorter reliability distances.

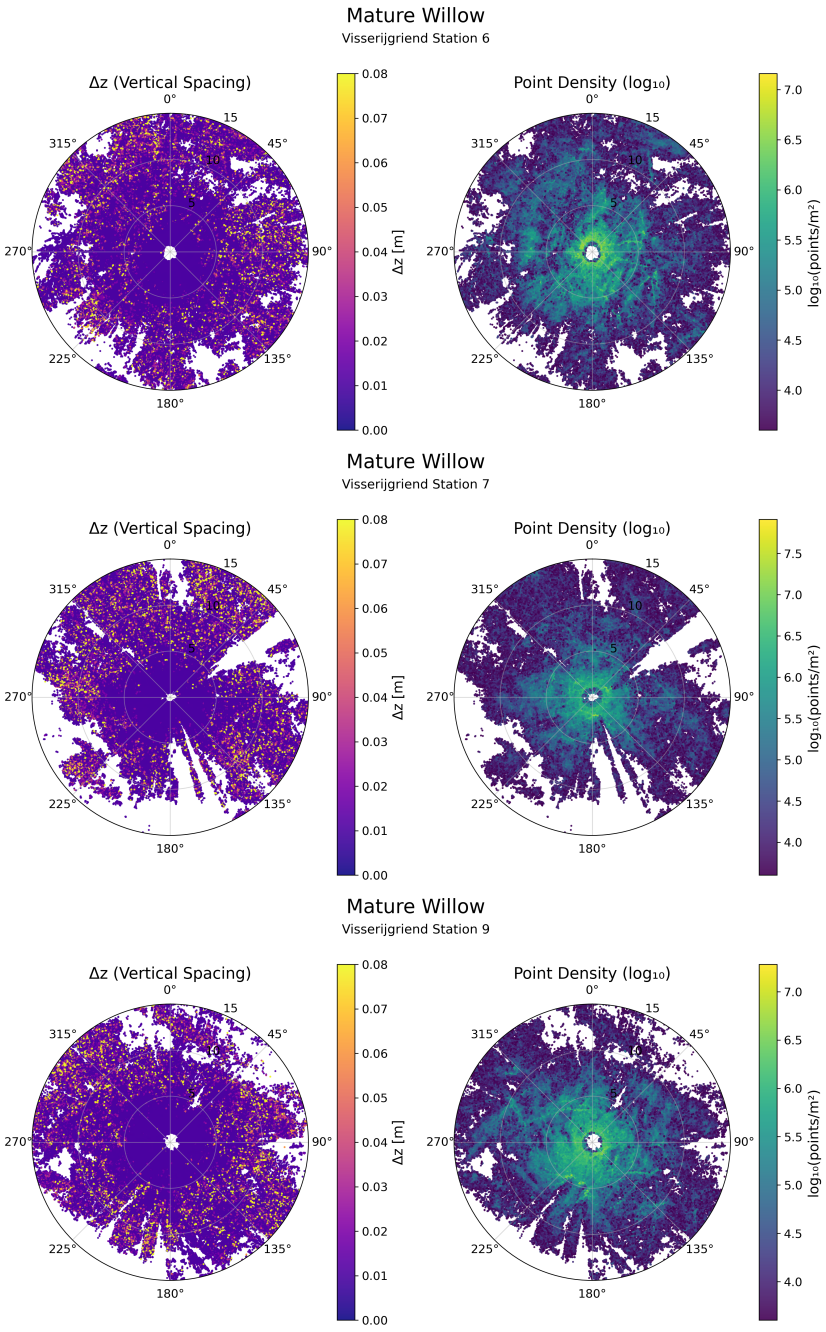

Figure 41: TLS sampling characteristics for mature willow stands. These stands show intermediate behaviour in point density and vertical spacing (Δz), reflecting differences in stand density and structural complexity.

G. Voxelised Tree Representations

To illustrate the structural representation of vegetation within the TLS-derived voxel framework, examples of voxelised individual trees from each forest stand type are presented in this appendix. These visualisations demonstrate how the selected voxel parameters capture the main structural elements of the vegetation without introducing systematic over- or underestimation of woody surfaces (Figure 42-44).

Examples are shown for representative stands including young willow, pollarded willow, hawthorn, mature willow, oak–elm, and willow–ash, illustrating the diversity in vegetation architecture across the study sites.

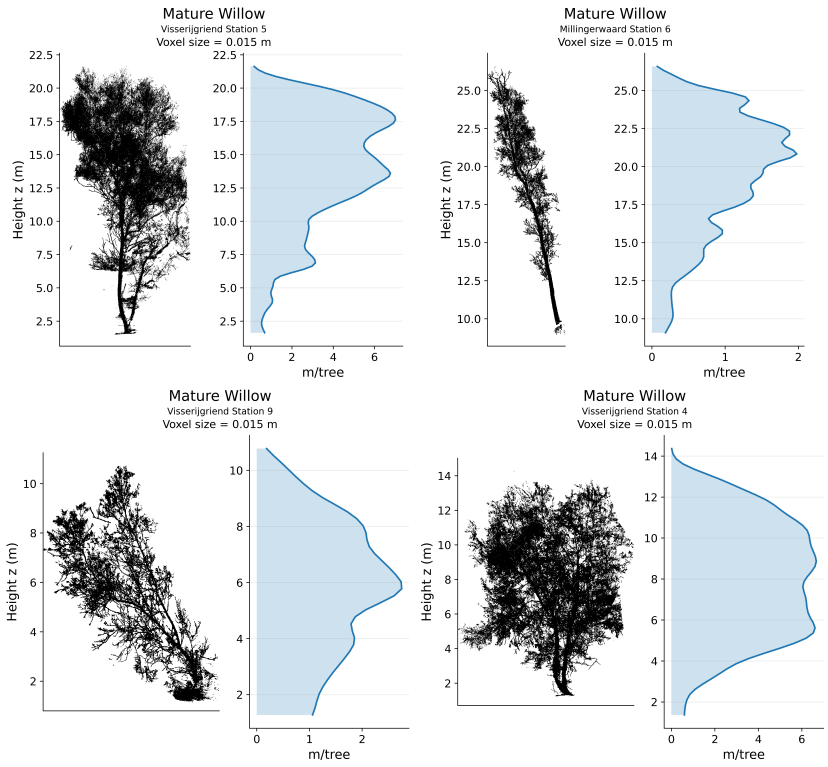

Figure 42: Voxelised representation of vegetation in mature willow stands. These stands exhibit heterogeneous structures with upright and inclined stems, and irregular canopy forms.

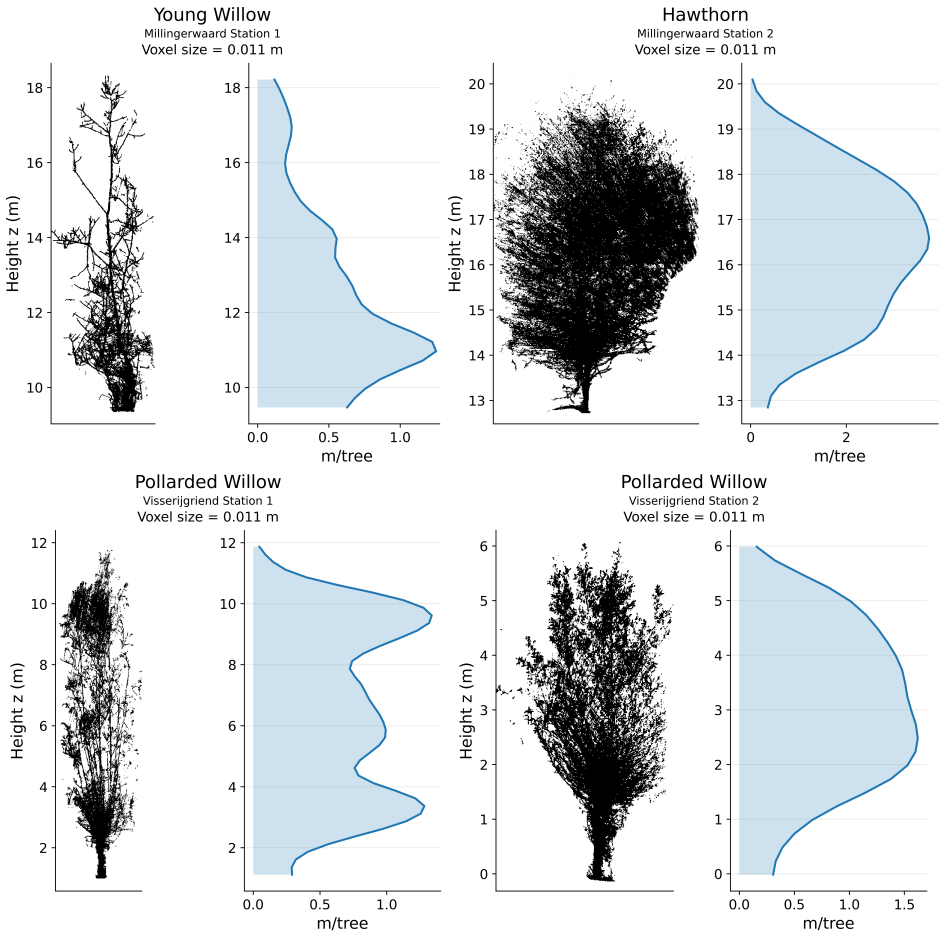

Figure 43: Voxelised representation of vegetation in young willow, pollarded willow, and hawthorn. The voxelisation captures dense branching structures and shrub-like vegetation forms characteristic of these stands.

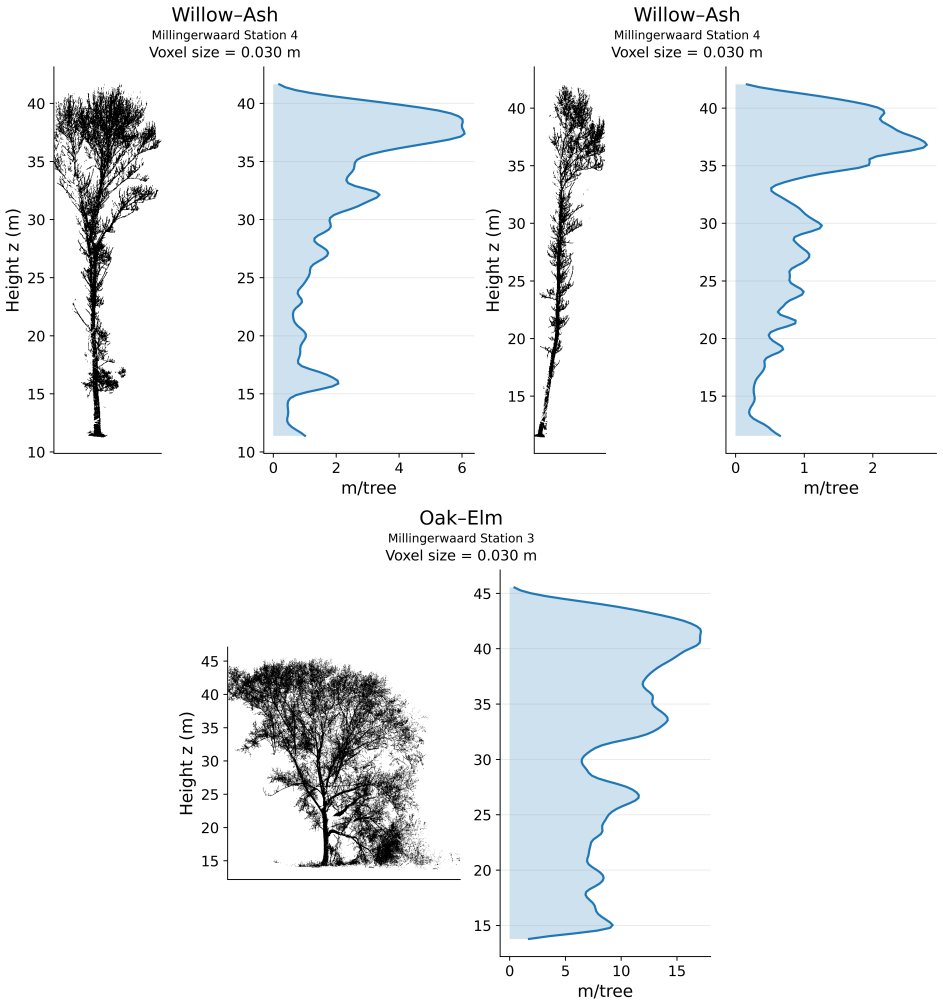

Figure 44: Voxelised representation of vegetation in more open, stem-dominated forest stands, oak–elm and willow–ash. The voxel framework captures larger stems and more widely spaced branching structures typical of these forest types.

H. TLS-Based Tree Detection for Forest Density Estimation

To illustrate the performance of the TLS-based tree detection approach across the full range of vegetation structures, all detection examples are provided in this appendix. While Figure 13 in the main text presents two representative cases, the Figures below show the resulting tree detection for all analysed forest stands (Figures 45–47). These visualisations highlight how the detection algorithm performs under contrasting vegetation structures. The resulting tree detections are subsequently used to derive stand-level forest density, as presented in Figure 12B.

Background colours represent either TLS point density or median return intensity, depending on the detection method used. Detected tree locations are shown as red markers, while blue squares indicate field-measured stem positions used for validation.

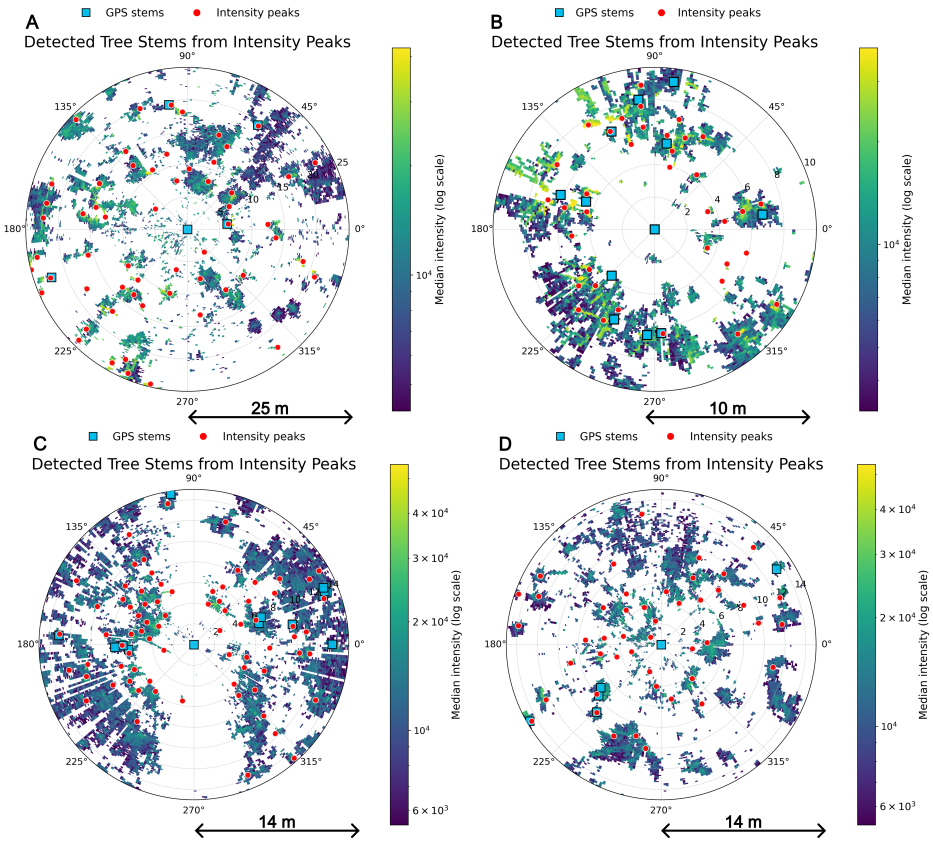

Figure 45: Detected trees from TLS intensity peaks shown in scanner-centred polar coordinates. Background colours represent median TLS return intensity (log scale). Red circles indicate detected intensity peaks corresponding to potential tree locations, while blue squares show field-measured tree positions obtained from GPS. Panels represent different forest stand types: (A) oak–elm stand and (B–D) mature willow stands. Polar coordinates are centred on the TLS scanner, with radial distance indicating horizontal distance from the scanner.

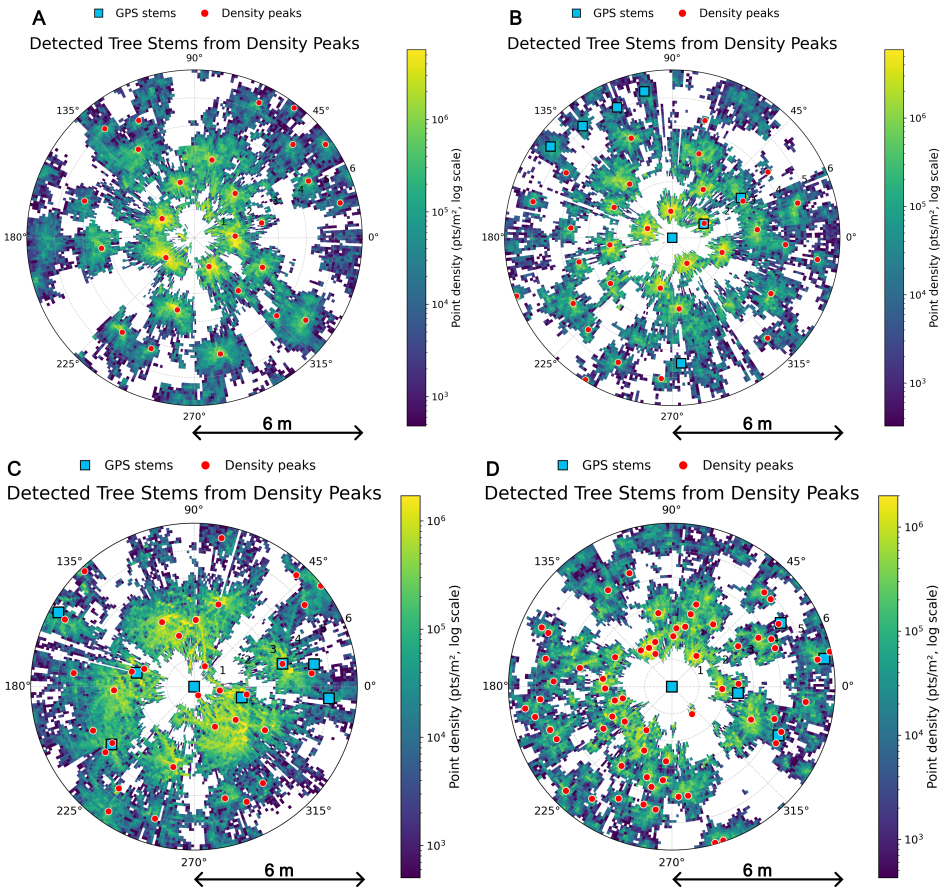

Figure 46: Detected trees from TLS point density peaks shown in scanner-centred polar coordinates. Background colours represent TLS point density (pts/m^2, log scale). Red circles indicate detected point density peaks corresponding to potential tree locations, while blue squares show field-measured tree positions obtained from GPS. Panels represent different forest stand types: (A–B) pollarded willow stands, (C) hawthorn stand, and (D) young willow stand. Polar coordinates are centred on the TLS scanner, with radial distance indicating horizontal distance from the scanner.

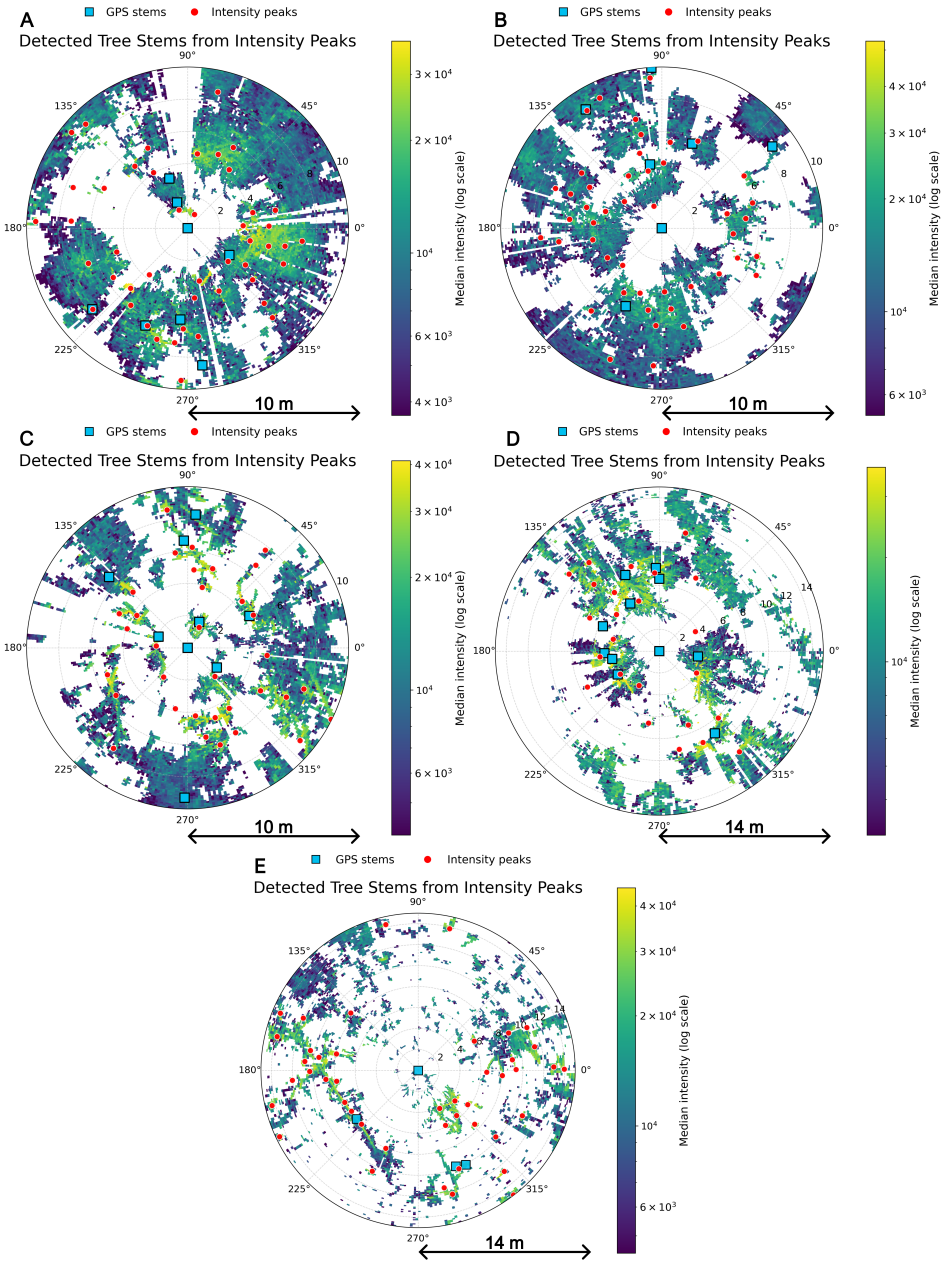

Figure 47: Detected trees from TLS intensity peaks shown in scanner-centred polar coordinates. Background colours represent median TLS return intensity (log scale). Red circles indicate detected intensity peaks corresponding to potential tree locations, while blue squares show field-measured tree positions obtained from GPS. Panels represent different forest stand types: (A–D) mature willow stands and (E) willow–ash mixed stand. Polar coordinates are centred on the TLS scanner, with radial distance indicating horizontal distance from the scanner.

I. Additional TLS Reliability Metrics

In the main analysis, TLS reliability was evaluated using canopy height band vertical resolution (Δz) and stem height band point density, as these metrics provided the most restrictive reliability thresholds across the analysed forest stands (Figure 15C-D). To provide a complete overview of the reliability assessment, the complementary metrics are presented in this appendix. Figure 48 shows the point density within the canopy height band, while Figure 49 presents the vertical point spacing (Δz) within the stem height band.

Point density in the canopy height band remains well above the reliability threshold for most stands across the analysed distances (Figure 48), indicating that canopy-level point density does not constrain reliable TLS observations. In contrast, the stem height band vertical resolution (Δz) only approaches the reliability threshold for the Hawthorn stand (Figure 49).

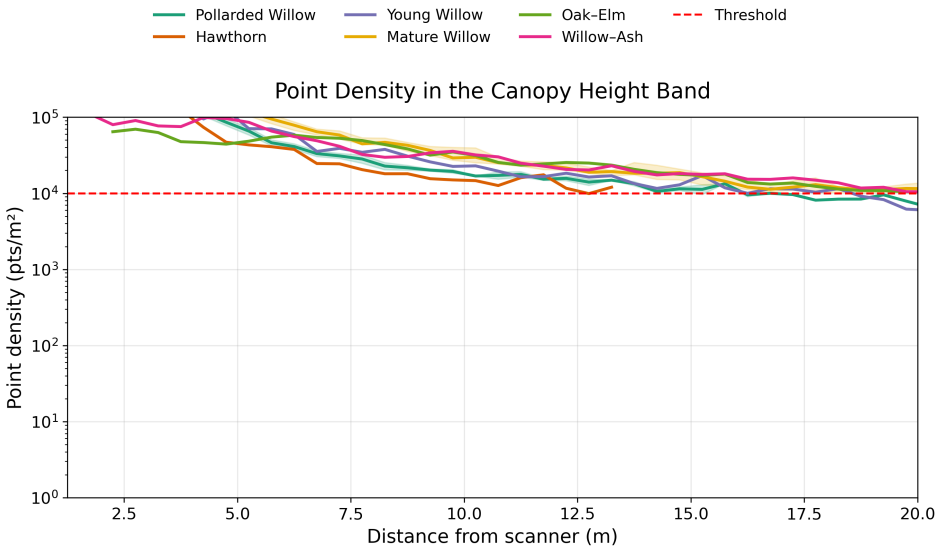

Figure 48: Point density within the canopy height band as a function of distance from the TLS scanner for each forest stand type. The dashed red line indicates the reliability threshold of 10,000 points m^{-2}. All stand types maintain point densities above this threshold over most of the analysed distances, indicating that canopy-level point density does not constrain reliable TLS observations.

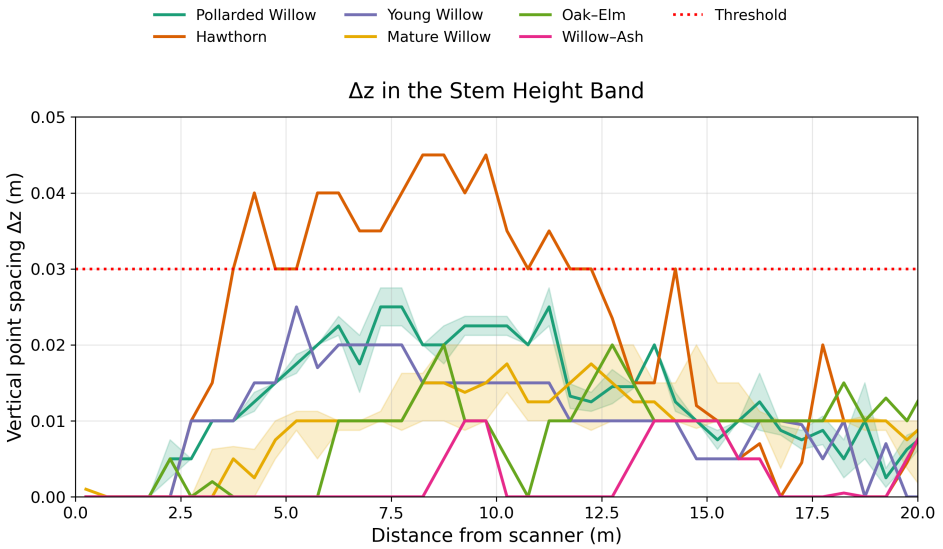

Figure 49: Vertical point spacing (Δz) within the stem height band as a function of distance from the TLS scanner for each forest stand type. The dashed red line indicates the reliability threshold of 0.03 m. The threshold is only approached for the Hawthorn stand, while other stand types remain well below the threshold, indicating sufficient vertical resolution for reliable TLS observations.

References

Actueel Hoogtebestand Nederland (July 24, 2019). *AHN Viewer*. AHN. URL: https://www.ahn.nl/ahn-viewer (visited on 04/06/2026).

Anderson, M. E. and J. M. Smith (Jan. 1, 2014). "Wave Attenuation by Flexible, Idealized Salt Marsh Vegetation". In: *Coastal Engineering* 83, pp. 82–92. ISSN: 0378-3839. DOI: 10.1016/j.coastaleng.2013.10.004. URL: https://www.sciencedirect.com/science/article/pii/S0378383913001609 (visited on 02/22/2026).

Antonarakis, A. S., K. S. Richards, J. Brasington, and M. Bithell (2009). "Leafless Roughness of Complex Tree Morphology Using Terrestrial Lidar". In: *Water Resources Research* 45.10. ISSN: 1944-7973. DOI: 10.1029/2008WR007666. URL: https://onlinelibrary.wiley.com/doi/abs/10.1029/2008WR007666 (visited on 07/10/2025).

Antonarakis, A. S., K. S. Richards, J. Brasington, and E. Muller (2010). "Determining Leaf Area Index and Leafy Tree Roughness Using Terrestrial Laser Scanning". In: *Water Resources Research* 46.6. ISSN: 1944-7973. DOI: 10.1029/2009WR008318. URL: https://onlinelibrary.wiley.com/doi/abs/10.1029/2009WR008318 (visited on 07/10/2025).

Augustin, Lauren N., Jennifer L. Irish, and Patrick Lynett (Mar. 1, 2009). "Laboratory and Numerical Studies of Wave Damping by Emergent and Near-Emergent Wetland Vegetation". In: *Coastal Engineering* 56.3, pp. 332–340. ISSN: 0378-3839. DOI: 10.1016/j.coastaleng.2008.09.004. URL: https://www.sciencedirect.com/science/article/pii/S037838390800152X (visited on 08/06/2025).

Baker, Scott, Enda Murphy, Andrew Cornett, and Paul Knox (June 8, 2022). "Experimental Study of Wave Attenuation Across an Artificial Salt Marsh". In: *Frontiers in Built Environment* 8. ISSN: 2297-3362. DOI: 10.3389/fbuil.2022.893664. URL: https://www.frontiersin.org/journals/built-environment/articles/10.3389/fbuil.2022.893664/full (visited on 09/14/2025).

Béland, Martin, Dennis D. Baldocchi, Jean-Luc Widlowski, Richard A. Fournier, and Michel M. Verstraete (Jan. 15, 2014). "On Seeing the Wood from the Leaves and the Role of Voxel Size in Determining Leaf Area Distribution of Forests with Terrestrial LiDAR". In: *Agricultural and Forest Meteorology* 184, pp. 82–97. ISSN: 0168-1923. DOI: 10.1016/j.agrformet.2013.09.005. URL: https://www.sciencedirect.com/science/article/pii/S0168192313002608 (visited on 07/12/2025).

Béland, Martin, Jean-Luc Widlowski, Richard A. Fournier, Jean-François Côté, and Michel M. Verstraete (Sept. 15, 2011). "Estimating Leaf Area Distribution in Savanna Trees from Terrestrial LiDAR Measurements". In: *Agricultural and Forest Meteorology* 151.9, pp. 1252–1266. ISSN: 0168-1923. DOI: 10.1016/j.agrformet.2011.05.004. URL: https://www.sciencedirect.com/science/article/pii/S0168192311001481 (visited on 07/12/2025).

Booij, N., R. C. Ris, and L. H. Holthuijsen (1999). "A Third-Generation Wave Model for Coastal Regions: 1. Model Description and Validation". In: *Journal of Geophysical Research: Oceans* 104.C4, pp. 7649–7666. ISSN: 2156-2202. DOI: 10.1029/98JC02622. URL: https://onlinelibrary.wiley.com/doi/abs/10.1029/98JC02622 (visited on 02/22/2026).

Boucher, Peter B, Ian Paynter, David A Orwig, Ilan Valencius, and Crystal Schaaf (Nov. 2, 2021). "Sampling Forests with Terrestrial Laser Scanning". In: *Annals of Botany* 128.6, pp. 689–708. ISSN: 0305-7364. DOI: 10.1093/aob/mcab073. URL: https://doi.org/10.1093/aob/mcab073 (visited on 11/05/2025).

Breugem, W. A. and L. H. Holthuijsen (May 1, 2007). "Generalized Shallow Water Wave Growth from Lake George". In: *Journal of Waterway, Port, Coastal, and Ocean Engineering* 133.3, pp. 173–182. DOI: 10.1061/(ASCE)0733-950X(2007)133:3(173). URL:

https://ascelibrary.org/doi/10.1061/%28ASCE%290733-950X%282007%29133%3A3%28173%29 (visited on 04/07/2026).

Bulkens, Maartje, Hamzah Muzaini, and Claudio Minca (May 3, 2016). "Dutch New Nature: (Re)Landscaping the Millingerwaard". In: *Journal of Environmental Planning and Management* 59.5, pp. 808–825. ISSN: 0964-0568. DOI: 10.1080/09640568.2015.1040872. URL: https://www.tandfonline.com/doi/citedby/10.1080/09640568.2015.1040872 (visited on 03/21/2026).

Calders, Kim, Jennifer Adams, John Armston, Harm Bartholomeus, Sebastien Bauwens, Lisa Patrick Bentley, Jerome Chave, F. Mark Danson, Miro Demol, Mathias Disney, Rachel Gaulton, Sruthi M. Krishna Moorthy, Shaun R. Levick, Ninni Saarinen, Crystal Schaaf, Atticus Stovall, Louise Terryn, Phil Wilkes, and Hans Verbeeck (Dec. 15, 2020). "Terrestrial Laser Scanning in Forest Ecology: Expanding the Horizon". In: *Remote Sensing of Environment* 251, p. 112102. ISSN: 0034-4257. DOI: 10.1016/j.rse.2020.112102. URL: https://www.sciencedirect.com/science/article/pii/S0034425720304752 (visited on 07/04/2025).

Dalrymple, Robert A., James T. Kirby, and Paul A. Hwang (Feb. 1, 1984). "Wave Diffraction Due to Areas of Energy Dissipation". In: *Journal of Waterway, Port, Coastal, and Ocean Engineering* 110.1, pp. 67–79. DOI: 10.1061/(ASCE)0733-950X(1984)110:1(67). URL: https://ascelibrary.org/doi/10.1061/%28ASCE%290733-950X%281984%29110%3A1%2867%29 (visited on 03/01/2026).

Danson, F. Mark, David Hetherington, Felix Morsdorf, Benjamin Koetz, and Britta Allgower (Jan. 2007). "Forest Canopy Gap Fraction From Terrestrial Laser Scanning". In: *IEEE Geoscience and Remote Sensing Letters* 4.1, pp. 157–160. ISSN: 1558-0571. DOI: 10.1109/LGRS.2006.887064. URL: https://ieeexplore.ieee.org/abstract/document/4063287 (visited on 07/12/2025).

Dassot, Mathieu, Thiéry Constant, and Meriem Fournier (Aug. 1, 2011). "The Use of Terrestrial LiDAR Technology in Forest Science: Application Fields, Benefits and Challenges". In: *Annals of Forest Science* 68.5, pp. 959–974. ISSN: 1297-966X. DOI: 10.1007/s13595-011-0102-2. URL: https://doi.org/10.1007/s13595-011-0102-2 (visited on 07/13/2025).

De Bruijn, M. (2020). "Wave Attenuation Due to Vegetation: Duursche Waarden (Case Study)". In: URL: https://repository.tudelft.nl/record/uuid:44174e17-e11f-44bc-826d-3dfa3740b87b (visited on 07/09/2025).

Dempwolff, León-Carlos, Gregor Melling, Christian Windt, Oliver Lojek, Tobias Martin, Ingrid Holzwarth, Hans Bihs, and Nils Goseberg (May 10, 2022). "Loads and Effects of Ship-Generated, Drawdown Waves in Confined Waterways - A Review of Current Knowledge and Methods". In: *Journal of Coastal and Hydraulic Structures* 2, pp. 46–46. ISSN: 2667-047X. DOI: 10.48438/jchs.2022.0013. URL: https://journals.open.tudelft.nl/jchs/article/view/5783 (visited on 04/07/2026).

Dunlop, Thomas, Alejandra Gijón Mancheño, William Glamore, Stefan Felder, and Bregje K. van Wesenbeeck (Apr. 30, 2025). "Quantifying Mangrove Forest Attributes Using Terrestrial Laser Scanning". In: *Estuaries and Coasts* 48.4, p. 108. ISSN: 1559-2731. DOI: 10.1007/s12237-025-01533-0. URL: https://doi.org/10.1007/s12237-025-01533-0 (visited on 07/15/2025).

Eijgenraam, Carel, Jarl Kind, Carlijn Bak, Ruud Brekelmans, Dick den Hertog, Matthijs Duits, Kees Roos, Pieter Vermeer, and Wim Kuijken (Feb. 20, 2014). "(PDF) Economically Efficient Standards to Protect the Netherlands Against Flooding". In: *ResearchGate*. DOI: 10.1287/inte.2013.0721. URL: https://www.researchgate.net/publication/273681624_Economically_Efficient_Standards_to_Protect_the_Netherlands_Against_Flooding (visited on 08/07/2025).

Fehérváry, István and Tímea Kiss (Nov. 30, 2021). "Riparian Vegetation Density Mapping of an Extremely Densely Vegetated Confined Floodplain". In: *Hydrology* 8.4, p. 176. ISSN: 2306-5338. DOI: 10.3390/hydrology8040176. URL: https://www.mdpi.com/2306-5338/8/4/176 (visited on 03/31/2026).

Fenton, John D., Boris Huber, Gerhard Klasz, and Norbert Krouzecky (2023). "Ship Waves in Rivers: Environmental Criteria and Analysis Methods for Measurements". In: *River Research and Applications* 39.4, pp. 629–647. ISSN: 1535-1467. DOI: 10.1002/rra.4101. URL: https://onlinelibrary.wiley.com/doi/abs/10.1002/rra.4101 (visited on 04/07/2026).

Foster-Martinez, M. R., J. R. Lacy, M. C. Ferner, and E. A. Variano (June 1, 2018). "Wave Attenuation across a Tidal Marsh in San Francisco Bay". In: *Coastal Engineering* 136, pp. 26–40. ISSN: 0378-3839. DOI: 10.1016/j.coastaleng.2018.02.001. URL: https://www.sciencedirect.com/science/article/pii/S0378383917305525 (visited on 08/06/2025).

Gijón Mancheño, A., V. Vuik, B. K. van Wesenbeeck, S. N. Jonkman, R. van Hespen, J. R. Moll, S. Kazi, I. Urrutia, and M. van Ledden (Apr. 4, 2024). "Integrating Mangrove Growth and Failure in Coastal Flood Protection Designs". In: *Scientific Reports* 14.1, p. 7951. ISSN: 2045-2322. DOI: 10.1038/s41598-024-58705-4. URL: https://www.nature.com/articles/s41598-024-58705-4 (visited on 03/23/2026).

Gijsman, Rik, Erik M. Horstman, Daphne van der Wal, Daniel A. Friess, Andrew Swales, and Kathelijne M. Wijnberg (July 8, 2021). "Nature-Based Engineering: A Review on Reducing Coastal Flood Risk With Mangroves". In: *Frontiers in Marine Science* 8. ISSN: 2296-7745. DOI: 10.3389/fmars.2021.702412. URL: https://www.frontiersin.org/journals/marine-science/articles/10.3389/fmars.2021.702412/full (visited on 03/21/2026).

Hackenberg, Jan, Heinrich Spiecker, Kim Calders, Mathias Disney, and Pasi Raumonen (Nov. 2015). "SimpleTree —An Efficient Open Source Tool to Build Tree Models from TLS Clouds". In: *Forests* 6.11 (11), pp. 4245–4294. ISSN: 1999-4907. DOI: 10.3390/f6114245. URL: https://www.mdpi.com/1999-4907/6/11/4245 (visited on 07/12/2025).

Hilker, Thomas, Martin van Leeuwen, Nicholas C. Coops, Michael A. Wulder, Glenn J. Newnham, David L. B. Jupp, and Darius S. Culvenor (Oct. 1, 2010). "Comparing Canopy Metrics Derived from Terrestrial and Airborne Laser Scanning in a Douglas-fir Dominated Forest Stand". In: *Trees* 24.5, pp. 819–832. ISSN: 1432-2285. DOI: 10.1007/s00468-010-0452-7. URL: https://doi.org/10.1007/s00468-010-0452-7 (visited on 07/11/2025).

Hopkinson, Chris, Laura Chasmer, Colin Young-Pow, and Paul Treitz (Sept. 17, 2003). "(PDF) Assessing Forest Metrics with a Ground-Based Scanning LiDAR." In: *ResearchGate*. DOI: 10.1139/x03-225. URL: https://www.researchgate.net/publication/221960181_Assessing_forest_metrics_with_a_ground-based_scanning_LiDAR (visited on 07/11/2025).

Hosoi, Fumiki and Kenji Omasa (Dec. 2006). "Voxel-Based 3-D Modeling of Individual Trees for Estimating Leaf Area Density Using High-Resolution Portable Scanning Lidar". In: *IEEE Transactions on Geoscience and Remote Sensing* 44.12, pp. 3610–3618. ISSN: 1558-0644. DOI: 10.1109/TGRS.2006.881743. URL: https://ieeexplore.ieee.org/document/4014317/ (visited on 07/12/2025).

Jadhav, Ranjit S., Qin Chen, and Jane M. Smith (July 1, 2013). "Spectral Distribution of Wave Energy Dissipation by Salt Marsh Vegetation". In: *Coastal Engineering* 77, pp. 99–107. ISSN: 0378-3839. DOI: 10.1016/j.coastaleng.2013.02.013. URL: https://www.sciencedirect.com/science/article/pii/S0378383913000537 (visited on 02/22/2026).

Jalonen, Johanna, Juha Järvelä, Juho-Pekka Virtanen, Matti Vaaja, Matti Kurkela, and Hannu Hyyppä (Feb. 2015). "Determining Characteristic Vegetation Areas by Terrestrial

Laser Scanning for Floodplain Flow Modeling". In: *Water* 7.2, pp. 420–437. ISSN: 2073-4441. DOI: 10.3390/w7020420. URL: https://www.mdpi.com/2073-4441/7/2/420 (visited on 09/05/2025).

Järvelä, Juha (Dec. 1, 2002). "Flow Resistance of Flexible and Stiff Vegetation: A Flume Study with Natural Plants". In: *Journal of Hydrology* 269.1, pp. 44–54. ISSN: 0022-1694. DOI: 10.1016/S0022-1694(02)00193-2. URL: https://www.sciencedirect.com/science/article/pii/S0022169402001932 (visited on 07/13/2025).

— (Mar. 2004). "Determination of Flow Resistance Caused by Non-submerged Woody Vegetation". In: *International Journal of River Basin Management* 2.1, pp. 61–70. ISSN: 1571-5124, 1814-2060. DOI: 10.1080/15715124.2004.9635222. URL: http://www.tandfonline.com/doi/abs/10.1080/15715124.2004.9635222 (visited on 07/11/2025).

Jongman, Brenden (May 29, 2018). "Effective Adaptation to Rising Flood Risk". In: *Nature Communications* 9.1, p. 1986. ISSN: 2041-1723. DOI: 10.1038/s41467-018-04396-1. URL: https://www.nature.com/articles/s41467-018-04396-1 (visited on 03/01/2026).

Jonkman, S.N., Marten Hillen, Robert Nicholls, W. Kanning, and Mathijs Ledden (Sept. 30, 2013). "Costs of Adapting Coastal Defences to Sea-Level Rise— New Estimates and Their Implications". In: *Journal of Coastal Research* 290, pp. 1212–1226. DOI: 10.2112/JCOASTRES-D-12-00230.1.

Jupp, David L.B., D.S. Culvenor, J.L. Lovell, G.J. Newnham, A.H. Strahler, and C.E. Woodcock (Feb. 1, 2009). "Estimating Forest LAI Profiles and Structural Parameters Using a Ground-Based Laser Called 'Echidna®". In: *Tree Physiology* 29.2, pp. 171–181. ISSN: 0829-318X. DOI: 10.1093/treephys/tpn022. URL: https://doi.org/10.1093/treephys/tpn022 (visited on 08/07/2025).

Kalloe, Su A., Bas Hofland, José A. A. Antolínez, and Bregje K. Van Wesenbeeck (Mar. 23, 2022). "Quantifying Frontal-Surface Area of Woody Vegetation: A Crucial Parameter for Wave Attenuation". In: *Frontiers in Marine Science* 9, p. 820846. ISSN: 2296-7745. DOI: 10.3389/fmars.2022.820846. URL: https://www.frontiersin.org/articles/10.3389/fmars.2022.820846/full (visited on 07/09/2025).

Karrenberg, S., P. J. Edwards, and J. Kollmann (2002). "The Life History of Salicaceae Living in the Active Zone of Floodplains". In: *Freshwater Biology* 47.4, pp. 733–748. ISSN: 1365-2427. DOI: 10.1046/j.1365-2427.2002.00894.x. URL: https://onlinelibrary.wiley.com/doi/abs/10.1046/j.1365-2427.2002.00894.x (visited on 03/13/2026).

Kelty, Kiernan, Tori Tomiczek, Daniel Thomas Cox, Pedro Lomonaco, and William Mitchell (Jan. 12, 2022). "Prototype-Scale Physical Model of Wave Attenuation Through a Mangrove Forest of Moderate Cross-Shore Thickness: LiDAR-Based Characterization and Reynolds Scaling for Engineering With Nature". In: *Frontiers in Marine Science* 8. ISSN: 2296-7745. DOI: 10.3389/fmars.2021.780946. URL: https://www.frontiersin.org/journals/marine-science/articles/10.3389/fmars.2021.780946/full (visited on 09/15/2025).

Keulegan, Garbis H. and LLoyd H. Carpenter (1958). *Journal of Research of the National Bureau of Standards*. The Bureau. 646 pp. Google Books: n1MXAQAAMAAJ.

Kramer, Koen, Stefan J. Vreugdenhil, and D. C. van der Werf (June 15, 2008). "Effects of Flooding on the Recruitment, Damage and Mortality of Riparian Tree Species: A Field and Simulation Study on the Rhine Floodplain". In: *Forest Ecology and Management* 255.11, pp. 3893–3903. ISSN: 0378-1127. DOI: 10.1016/j.foreco.2008.03.044. URL: https://www.sciencedirect.com/science/article/pii/S0378112708002922 (visited on 09/11/2025).

Kükenbrink, Daniel, Oliver Gardi, Felix Morsdorf, Esther Thürig, Andreas Schellenberger, and Lukas Mathys (Nov. 2, 2021). "Above-Ground Biomass References for Urban Trees from Terrestrial Laser Scanning Data". In: *Annals of Botany* 128.6, pp. 709–724. ISSN:

0305-7364. DOI: 10.1093/aob/mcab002. URL: https://doi.org/10.1093/aob/mcab002 (visited on 09/05/2025).

Lang, Mait, Andres Kuusk, Kersti Vennik, Aive Liibusk, Kristina Türk, and Allan Sims (Jan. 2021). "Horizontal Visibility in Forests". In: *Remote Sensing* 13.21, p. 4455. ISSN: 2072-4292. DOI: 10.3390/rs13214455. URL: https://www.mdpi.com/2072-4292/13/21/4455 (visited on 01/09/2026).

Lara, J. L., M. Maza, B. Ondiviela, J. Trinogga, I. J. Losada, T. J. Bouma, and N. Gordejuela (Jan. 1, 2016). "Large-Scale 3-D Experiments of Wave and Current Interaction with Real Vegetation. Part 1: Guidelines for Physical Modeling". In: *Coastal Engineering* 107, pp. 70–83. ISSN: 0378-3839. DOI: 10.1016/j.coastaleng.2015.09.012. URL: https://www.sciencedirect.com/science/article/pii/S0378383915001696 (visited on 03/08/2026).

Lecerf, A., C. Evangelista, J. Cucherousset, and A. Boiché (May 1, 2016). "Riparian Overstory–Understory Interactions and Their Potential Implications for Forest-Stream Linkages". In: *Forest Ecology and Management* 367, pp. 112–119. ISSN: 0378-1127. DOI: 10.1016/j.foreco.2016.02.031. URL: https://www.sciencedirect.com/science/article/pii/S0378112716300524 (visited on 01/23/2026).

Lightbody, Anne F. and Heidi M. Nepf (2006). "Prediction of Velocity Profiles and Longitudinal Dispersion in Salt Marsh Vegetation". In: *Limnology and Oceanography* 51.1, pp. 218–228. ISSN: 1939-5590. DOI: 10.4319/lo.2006.51.1.0218. URL: https://onlinelibrary.wiley.com/doi/abs/10.4319/lo.2006.51.1.0218 (visited on 09/14/2025).

Makaske, Bart, Gilbert J. Maas, Claus van den Brink, and Henk P. Wolfert (June 2011). "The Influence of Floodplain Vegetation Succession on Hydraulic Roughness: Is Ecosystem Rehabilitation in Dutch Embanked Floodplains Compatible with Flood Safety Standards?" In: *Ambio* 40.4, pp. 370–376. ISSN: 0044-7447. DOI: 10.1007/s13280-010-0120-6. PMID: 21809780. URL: https://www.ncbi.nlm.nih.gov/pmc/articles/PMC3357742/ (visited on 09/05/2025).

Malhi, Yadvinder, Tobias Jackson, Lisa Patrick Bentley, Alvaro Lau, Alexander Shenkin, Martin Herold, Kim Calders, Harm Bartholomeus, and Mathias I. Disney (Feb. 16, 2018). "New Perspectives on the Ecology of Tree Structure and Tree Communities through Terrestrial Laser Scanning". In: *Interface Focus* 8.2, p. 20170052. DOI: 10.1098/rsfs.2017.0052. URL: https://royalsocietypublishing.org/doi/10.1098/rsfs.2017.0052 (visited on 07/11/2025).

Markus-Michalczyk, Heike and Dieter Hanelt (Jan. 1, 2019). "Willow Species Vary in Elevational Occurrence and Morphological Characteristics on the Tidal Freshwater Section of the Elbe Estuary". In: *Ecohydrology & Hydrobiology* 19.1, pp. 14–23. ISSN: 1642-3593. DOI: 10.1016/j.ecohyd.2018.08.006. URL: https://www.sciencedirect.com/science/article/pii/S1642359317301131 (visited on 03/11/2026).

Markus-Michalczyk, Heike and Matthias Michalczyk (Jan. 22, 2023). "Floodplain Forest Restoration as a Nature-Based Solution to Create Climate-Resilient Communities in European Lowland Estuaries". In: *Water* 15.3. ISSN: 2073-4441. DOI: 10.3390/w15030440. URL: https://www.mdpi.com/2073-4441/15/3/440 (visited on 03/13/2026).

Mathes, Thomas, Dominik Seidel, Karl-Heinz Häberle, Hans Pretzsch, and Peter Annighöfer (Jan. 2023). "What Are We Missing? Occlusion in Laser Scanning Point Clouds and Its Impact on the Detection of Single-Tree Morphologies and Stand Structural Variables". In: *Remote Sensing* 15.2 (2), p. 450. ISSN: 2072-4292. DOI: 10.3390/rs15020450. URL: https://www.mdpi.com/2072-4292/15/2/450 (visited on 07/14/2025).

Maza, Maria, Javier L. Lara, and Inigo J. Losada (Apr. 1, 2015). "Tsunami Wave Interaction with Mangrove Forests: A 3-D Numerical Approach". In: *Coastal Engineering* 98, pp. 33–

54. ISSN: 0378-3839. DOI: 10.1016/j.coastaleng.2015.01.002. URL: https://www.sciencedirect.com/science/article/pii/S0378383915000113 (visited on 02/22/2026).

McClain, Charles D., Karen D. Holl, and David M. Wood (2011). "Successional Models as Guides for Restoration of Riparian Forest Understory". In: *Restoration Ecology* 19.2, pp. 280–289. ISSN: 1526-100X. DOI: 10.1111/j.1526-100X.2009.00616.x. URL: https://onlinelibrary.wiley.com/doi/abs/10.1111/j.1526-100X.2009.00616.x (visited on 01/23/2026).

Mendez, Fernando J. and Inigo J. Losada (Apr. 1, 2004). "An Empirical Model to Estimate the Propagation of Random Breaking and Nonbreaking Waves over Vegetation Fields". In: *Coastal Engineering* 51.2, pp. 103–118. ISSN: 0378-3839. DOI: 10.1016/j.coastaleng.2003.11.003. URL: https://www.sciencedirect.com/science/article/pii/S0378383903001182 (visited on 11/24/2025).

Ministry of Agriculture, Nature and Food Quality (2007). *Natura 2000 Area Document: Gelderse Poort (Area 67)*. URL: https://www.natura2000.nl/sites/default/files/documenten/gebieden/038/067_gebiedendocument_Gelderse_Poort.pdf (visited on 03/21/2026).

Möller, Iris, Matthias Kudella, Franziska Rupprecht, Tom Spencer, Maike Paul, Bregje K. van Wesenbeeck, Guido Wolters, Kai Jensen, Tjeerd J. Bouma, Martin Miranda-Lange, and Stefan Schimmels (Oct. 2014). "Wave Attenuation over Coastal Salt Marshes under Storm Surge Conditions". In: *Nature Geoscience* 7.10, pp. 727–731. ISSN: 1752-0908. DOI: 10.1038/ngeo2251. URL: https://www.nature.com/articles/ngeo2251 (visited on 09/16/2025).

Morison, J.R., J.W. Johnson, and S.A. Schaaf (May 1, 1950). "The Force Exerted by Surface Waves on Piles". In: *Journal of Petroleum Technology* 2.05, pp. 149–154. ISSN: 0149-2136. DOI: 10.2118/950149-G. URL: https://doi.org/10.2118/950149-G (visited on 02/22/2026).

Newnham, Glenn J., John D. Armston, Kim Calders, Mathias I. Disney, Jenny L. Lovell, Crystal B. Schaaf, Alan H. Strahler, and F. Mark Danson (Dec. 1, 2015). "Terrestrial Laser Scanning for Plot-Scale Forest Measurement". In: *Current Forestry Reports* 1.4, pp. 239–251. ISSN: 2198-6436. DOI: 10.1007/s40725-015-0025-5. URL: https://doi.org/10.1007/s40725-015-0025-5 (visited on 07/10/2025).

Oettel, Janine, Martin Braun, Markus Sallmannshofer, Maarten de Groot, Silvio Schueler, Charlotte Virgillito, Marjana Westergren, Gregor Božič, Laszlo Nagy, Srdjan Stojnić, and Katharina Lapin (Sept. 15, 2022). "River Distance, Stand Basal Area, and Climatic Conditions Are the Main Drivers Influencing Lying Deadwood in Riparian Forests". In: *Forest Ecology and Management* 520, p. 120415. ISSN: 0378-1127. DOI: 10.1016/j.foreco.2022.120415. URL: https://www.sciencedirect.com/science/article/pii/S0378112722004091 (visited on 09/05/2025).

Olsoy, Peter J., Nancy F. Glenn, Patrick E. Clark, and DeWayne R. Derryberry (Feb. 2014). "Aboveground Total and Green Biomass of Dryland Shrub Derived from Terrestrial Laser Scanning". In: *ISPRS Journal of Photogrammetry and Remote Sensing* 88, pp. 166–173. ISSN: 09242716. DOI: 10.1016/j.isprsjprs.2013.12.006. URL: https://linkinghub.elsevier.com/retrieve/pii/S0924271613003006 (visited on 03/24/2026).

Ozeren, Y., D. G. Wren, and W. Wu (Sept. 1, 2014). "Experimental Investigation of Wave Attenuation through Model and Live Vegetation". In: *Journal of Waterway, Port, Coastal, and Ocean Engineering* 140.5, p. 04014019. DOI: 10.1061/(ASCE)WW.1943-5460.0000251. URL: https://ascelibrary.org/doi/10.1061/%28ASCE%29WW.1943-5460.0000251 (visited on 03/01/2026).

Penning, Ellis, Henk Steetzel, Robbin Van Santen, Marieke De Lange, Sonja Ouwerkerk, Vincent Vuik, Jasper Fiselier, and Jaap Van Thiel De Vries (2016). "Establishing Vegetated

Foreshores to Increase Dike Safety along Lake Shores". In: *E3S Web of Conferences* 7. Ed. by M. Lang, F. Klijn, and P. Samuels, p. 12008. ISSN: 2267-1242. DOI: 10.1051/e3sconf/20160712008. URL: http://www.e3s-conferences.org/10.1051/e3sconf/20160712008 (visited on 07/10/2025).

Quang Bao, Tran (Sept. 26, 2011). "Effect of Mangrove Forest Structures on Wave Attenuation in Coastal Vietnam". In: *Oceanologia* 53.3, pp. 807–818. ISSN: 0078-3234. DOI: 10.5697/oc.53-3.807. URL: https://www.sciencedirect.com/science/article/pii/S0078323411500259 (visited on 09/15/2025).

Raumonen, P., E. Casella, K. Calders, S. Murphy, M. Åkerblom, and M. Kaasalainen (Mar. 11, 2015). "MASSIVE-SCALE TREE MODELLING FROM TLS DATA". In: *ISPRS Annals of the Photogrammetry, Remote Sensing and Spatial Information Sciences* II-3-W4, pp. 189–196. ISSN: 2194-9042. DOI: 10.5194/isprsannals-II-3-W4-189-2015. URL: https://isprs-annals.copernicus.org/articles/II-3-W4/189/2015/isprsannals-II-3-W4-189-2015.html (visited on 07/10/2025).

Reker, Jessica, Gerard Litjens, and Alphons van Winden (June 2007). "hoogvliet, wonen aan een getijdengeul". In.

Ren, Jie, Zengchuan Dong, Dawei Jin, Yue Zhou, Wei Xu, and Biao Sun (Jan. 6, 2021). "Wave-Attenuation Characteristics of Combined-Vegetation Wave Break Forests for Big Rivers with Large Flood Water Level Changes". In: *Water Science and Technology* 83.4, pp. 831–840. ISSN: 0273-1223. DOI: 10.2166/wst.2021.011. URL: https://doi.org/10.2166/wst.2021.011 (visited on 09/04/2025).

Rijkswaterstaat (2017). *Hydra-NL: User Manual for the Hydraulic Boundary Conditions Software*. The Netherlands: Ministry of Infrastructure and the Environment.

— (2026). *Waterbeheer - Rijkswaterstaat Waterinfo*. URL: https://waterinfo.rws.nl/thema/Waterbeheer (visited on 04/06/2026).

Rowiński, Paweł M., Kaisa Västilä, Jochen Aberle, Juha Järvelä, and Monika B. Kalinowska (Dec. 1, 2018). "How Vegetation Can Aid in Coping with River Management Challenges: A Brief Review". In: *Ecohydrology & Hydrobiology*. SI: Ecohydrology for the Circular Economy and Nature-Based Solutions towards Mitigation/Adaptation to Climate Change 18.4, pp. 345–354. ISSN: 1642-3593. DOI: 10.1016/j.ecohyd.2018.07.003. URL: https://www.sciencedirect.com/science/article/pii/S1642359318300454 (visited on 09/13/2025).

Schneider, C., C. L. R. Laizé, M. C. Acreman, and M. Flörke (Jan. 28, 2013). "How Will Climate Change Modify River Flow Regimes in Europe?" In: *Hydrology and Earth System Sciences* 17.1, pp. 325–339. ISSN: 1027-5606. DOI: 10.5194/hess-17-325-2013. URL: https://hess.copernicus.org/articles/17/325/2013/hess-17-325-2013.html (visited on 03/21/2026).

Schnitzler, Annik (Oct. 1994). "Conservation of Biodiversity in Alluvial Hardwood Forests of the Temperate Zone. The Example of the Rhine Valley". In: *Forest Ecology and Management* 68.2–3, pp. 385–398. ISSN: 03781127. DOI: 10.1016/0378-1127(94)90059-0. URL: https://linkinghub.elsevier.com/retrieve/pii/0378112794900590 (visited on 09/05/2025).

Shao, Jie, Wuming Zhang, Nicolas Mellado, Nan Wang, Shuangna Jin, Shangshu Cai, Lei Luo, Thibault Lejemble, and Guangjian Yan (May 1, 2020). "SLAM-aided Forest Plot Mapping Combining Terrestrial and Mobile Laser Scanning". In: *ISPRS Journal of Photogrammetry and Remote Sensing* 163, pp. 214–230. ISSN: 0924-2716. DOI: 10.1016/j.isprsjprs.2020.03.008. URL: https://www.sciencedirect.com/science/article/pii/S0924271620300782 (visited on 04/07/2026).

Soma, Maxime, François Pimont, Denis Allard, Richard Fournier, and Jean-Luc Dupuy (Aug. 1, 2020). "Mitigating Occlusion Effects in Leaf Area Density Estimates from Terrestrial LiDAR through a Specific Kriging Method". In: *Remote Sensing of Environment* 245, p. 111836. ISSN: 0034-4257. DOI: 10.1016/j.rse.2020.111836. URL: https://www.sciencedirect.com/science/article/pii/S0034425720302066 (visited on 07/14/2025).

Stoker, J.M. (2004). "Voxels as a Representation of Multiple-Return Lidar Data". In.

Straatsma, M. W., J. J. Warmink, and H. Middelkoop (Mar. 1, 2008). "Two Novel Methods for Field Measurements of Hydrodynamic Density of Floodplain Vegetation Using Terrestrial Laser Scanning and Digital Parallel Photography". In: *International Journal of Remote Sensing* 29.5, pp. 1595–1617. ISSN: 0143-1161. DOI: 10.1080/01431160701736455. URL: https://doi.org/10.1080/01431160701736455 (visited on 09/05/2025).

Suzuki, Tomohiro, Marcel Zijlema, Bastiaan Burger, Martijn C. Meijer, and Siddharth Narayan (Jan. 1, 2012). "Wave Dissipation by Vegetation with Layer Schematization in SWAN". In: *Coastal Engineering* 59.1, pp. 64–71. ISSN: 0378-3839. DOI: 10.1016/j.coastaleng.2011.07.006. URL: https://www.sciencedirect.com/science/article/pii/S0378383911001347 (visited on 02/22/2026).

Tan, Kai, Weiguo Zhang, Zhen Dong, Xiaolong Cheng, and Xiaojun Cheng (Aug. 2021). "Leaf and Wood Separation for Individual Trees Using the Intensity and Density Data of Terrestrial Laser Scanners". In: *IEEE Transactions on Geoscience and Remote Sensing* 59.8, pp. 7038–7050. ISSN: 1558-0644. DOI: 10.1109/TGRS.2020.3032167. URL: https://ieeexplore.ieee.org/abstract/document/9246255 (visited on 12/02/2025).

Tang, Xiaochun, Philip L. -F. Liu, Pengzhi Lin, Yun Jiang, and Yu-Hsi Lin (Aug. 1, 2022). "An Empirical Model for Predicting Wave Attenuation inside Vegetation Domain". In: *Ocean Engineering* 257, p. 111636. ISSN: 0029-8018. DOI: 10.1016/j.oceaneng.2022.111636. URL: https://www.sciencedirect.com/science/article/pii/S0029801822009970 (visited on 09/15/2025).

Temmerman, Stijn, Erik M. Horstman, Ken W. Krauss, Julia C. Mullarney, Ignace Pelckmans, and Ken Schoutens (Jan. 16, 2023). "Marshes and Mangroves as Nature-Based Coastal Storm Buffers". In: *Annual Review of Marine Science* 15 (Volume 15, 2023), pp. 95–118. ISSN: 1941-1405, 1941-0611. DOI: 10.1146/annurev-marine-040422-092951. URL: https://www.annualreviews.org/content/journals/10.1146/annurev-marine-040422-092951 (visited on 03/14/2026).

Temmerman, Stijn, Patrick Meire, Tjeerd J. Bouma, Peter M. J. Herman, Tom Ysebaert, and Huib J. De Vriend (Dec. 2013). "Ecosystem-Based Coastal Defence in the Face of Global Change". In: *Nature* 504.7478, pp. 79–83. ISSN: 1476-4687. DOI: 10.1038/nature12859. URL: https://www.nature.com/articles/nature12859 (visited on 03/11/2026).

Tinoco, Rafael O., Jorge E. San Juan, and Julia C. Mullarney (2020). "Simplification Bias: Lessons from Laboratory and Field Experiments on Flow through Aquatic Vegetation". In: *Earth Surface Processes and Landforms* 45.1, pp. 121–143. ISSN: 1096-9837. DOI: 10.1002/esp.4743. URL: https://onlinelibrary.wiley.com/doi/abs/10.1002/esp.4743 (visited on 09/14/2025).

Torralba, Jesús, Juan Pedro Carbonell-Rivera, Luis Ángel Ruiz, and Pablo Crespo-Peremarch (Dec. 2022). "Analyzing TLS Scan Distribution and Point Density for the Estimation of Forest Stand Structural Parameters". In: *Forests* 13.12 (12), p. 2115. ISSN: 1999-4907. DOI: 10.3390/f13122115. URL: https://www.mdpi.com/1999-4907/13/12/2115 (visited on 07/14/2025).

Van Starrenburg, Corinne, Alejandra Gijón Mancheño, Johan van de Koppel, Daphne van der Wal, Matthijs H. Slegt, Maarten J. J. Schrama, Matty P. Berg, Bregje K. van Wesenbeeck, Su A. Kalloe, Bas Hofland, and Tjeerd J. Bouma (Apr. 1, 2026). "A Trade-off Approach to

Optimize Nature-Based Flood Defense Designs: Riparian Willow Forests as Case Study". In: *Ecological Engineering* 225, p. 107886. ISSN: 0925-8574. DOI: 10.1016/j.ecoleng.2025.107886. URL: https://www.sciencedirect.com/science/article/pii/S0925857425003763 (visited on 02/12/2026).

Van Starrenburg, Corinne, Lennart van Ijzerloo, Johan van de Koppel, Daphne van der Wal, and Tjeerd J. Bouma (Aug. 15, 2025). "Are Willows Suitable for Flood Defense? Quantifying Mechanical Properties of Willow Species". In: *Estuarine, Coastal and Shelf Science* 320, p. 109306. ISSN: 0272-7714. DOI: 10.1016/j.ecss.2025.109306. URL: https://www.sciencedirect.com/science/article/pii/S0272771425001842 (visited on 03/11/2026).

Van Veelen, Thomas J., Harshinie Karunarathna, and Dominic E. Reeve (Mar. 1, 2021). "Modelling Wave Attenuation by Quasi-Flexible Coastal Vegetation". In: *Coastal Engineering* 164, p. 103820. ISSN: 0378-3839. DOI: 10.1016/j.coastaleng.2020.103820. URL: https://www.sciencedirect.com/science/article/pii/S0378383920305068 (visited on 09/14/2025).

Van Wesenbeeck, Bregje K., Guido Wolters, José A. A. Antolínez, Sudarshini A. Kalloe, Bas Hofland, Wiebe P. de Boer, Ceylan Çete, and Tjeerd J. Bouma (Feb. 3, 2022). "Wave Attenuation through Forests under Extreme Conditions". In: *Scientific Reports* 12.1, p. 1884. ISSN: 2045-2322. DOI: 10.1038/s41598-022-05753-3. URL: https://www.nature.com/articles/s41598-022-05753-3 (visited on 07/09/2025).

Van Zelst, Vincent T. M., Jasper T. Dijkstra, Bregje K. van Wesenbeeck, Dirk Eilander, Edward P. Morris, Hessel C. Winsemius, Philip J. Ward, and Mindert B. de Vries (Nov. 11, 2021). "Cutting the Costs of Coastal Protection by Integrating Vegetation in Flood Defences". In: *Nature Communications* 12.1, p. 6533. ISSN: 2041-1723. DOI: 10.1038/s41467-021-26887-4. URL: https://www.nature.com/articles/s41467-021-26887-4 (visited on 09/16/2025).

Van den Hoven, Kim, Jim van Belzen, Maarten G. Kleinhans, Dirk M. J. Schot, Joanne Merry, Jantsje M. van Loon-Steensma, and Tjeerd J. Bouma (Nov. 5, 2023). "How Natural Foreshores Offer Flood Protection during Dike Breaches: An Explorative Flume Study". In: *Estuarine, Coastal and Shelf Science* 294, p. 108560. ISSN: 0272-7714. DOI: 10.1016/j.ecss.2023.108560. URL: https://www.sciencedirect.com/science/article/pii/S0272771423003505 (visited on 07/09/2025).

Van Loon-Steensma, Jantsje M. and Matthijs Kok (2016). "Risk Reduction by Combining Nature Values with Flood Protection?" In: *E3S Web of Conferences* 7. Ed. by M. Lang, F. Klijn, and P. Samuels, p. 13003. ISSN: 2267-1242. DOI: 10.1051/e3sconf/20160713003. URL: http://www.e3s-conferences.org/10.1051/e3sconf/20160713003 (visited on 07/09/2025).

Van Wesenbeeck, Bregje K., Wiebe De Boer, Siddharth Narayan, Wouter R. L. Van Der Star, and Mindert B. De Vries (Oct. 2017). "Coastal and Riverine Ecosystems as Adaptive Flood Defenses under a Changing Climate". In: *Mitigation and Adaptation Strategies for Global Change* 22.7, pp. 1087–1094. ISSN: 1381-2386, 1573-1596. DOI: 10.1007/s11027-016-9714-z. URL: http://link.springer.com/10.1007/s11027-016-9714-z (visited on 07/09/2025).

Villarin, Lauren A., David M. Chapin, and John E. Jones (Feb. 28, 2009). "Riparian Forest Structure and Succession in Second-Growth Stands of the Central Cascade Mountains, Washington, USA". In: *Forest Ecology and Management* 257.5, pp. 1375–1385. ISSN: 0378-1127. DOI: 10.1016/j.foreco.2008.12.007. URL: https://www.sciencedirect.com/science/article/pii/S0378112708008918 (visited on 01/23/2026).

Vogel, Steven (Apr. 21, 1996). *Life in Moving Fluids: The Physical Biology of Flow*. Princeton University Press. 486 pp. ISBN: 978-0-691-02616-9. Google Books: XBqncfXFsOIC.

Vuik, Vincent, Bas W. Borsje, Pim W. J. M. Willemsen, and Sebastiaan N. Jonkman (Apr. 1, 2019). "Salt Marshes for Flood Risk Reduction: Quantifying Long-Term Effectiveness and Life-Cycle Costs". In: *Ocean & Coastal Management* 171, pp. 96–110. ISSN: 0964-5691. DOI: 10.1016/j.ocecoaman.2019.01.010. URL: https://www.sciencedirect.com/science/article/pii/S0964569118307026 (visited on 07/09/2025).

Vuik, Vincent, Sebastiaan N. Jonkman, and Saskia van Vuren (2016). "Nature-Based Flood Protection: Using Vegetated Foreshores for Reducing Coastal Risk". In: *E3S Web of Conferences* 7, p. 13014. ISSN: 2267-1242. DOI: 10.1051/e3sconf/20160713014. URL: https://www.e3s-conferences.org/articles/e3sconf/abs/2016/02/e3sconf_flood2016_13014/e3sconf_flood2016_13014.html (visited on 07/10/2025).

Wardius, Yannik and Sebastian Hein (Apr. 1, 2024). "Terrestrial Laser Scanning vs. Manual Methods for Assessing Complex Forest Stand Structure: A Comparative Analysis on Plenter Forests". In: *European Journal of Forest Research* 143.2, pp. 635–649. ISSN: 1612-4677. DOI: 10.1007/s10342-023-01641-1. URL: https://doi.org/10.1007/s10342-023-01641-1 (visited on 09/11/2025).

Wesenbeeck, Bregje K. van, Vincent T. M. van Zelst, Jose A. A. Antolinez, and Wiebe P. de Boer (Apr. 3, 2025). "Quantifying Uncertainty in Wave Attenuation by Mangroves to Inform Coastal Green Belt Policies". In: *Communications Earth & Environment* 6.1, p. 258. ISSN: 2662-4435. DOI: 10.1038/s43247-025-02178-4. URL: https://www.nature.com/articles/s43247-025-02178-4 (visited on 03/27/2026).

Wilkes, Phil, Alvaro Lau, Mathias Disney, Kim Calders, Andrew Burt, Jose Gonzalez de Tanago, Harm Bartholomeus, Benjamin Brede, and Martin Herold (July 1, 2017). "Data Acquisition Considerations for Terrestrial Laser Scanning of Forest Plots". In: *Remote Sensing of Environment* 196, pp. 140–153. ISSN: 0034-4257. DOI: 10.1016/j.rse.2017.04.030. URL: https://www.sciencedirect.com/science/article/pii/S003442571730189X (visited on 07/11/2025).

Yan, Zhaojin (2019). *A Concave Hull Methodology for Calculating the Crown Volume of Individual Trees Based on Vehicle-Borne LiDAR Data*. ResearchGate. URL: https://www.researchgate.net/publication/331781106_A_Concave_Hull_Methodology_for_Calculating_the_Crown_Volume_of_Individual_Trees_Based_on_Vehicle-Borne_LiDAR_Data (visited on 09/08/2025).

You, Lei, Xiaosa Chang, Yian Sun, Yong Pang, Yan Feng, and Xinyu Song (Jan. 2023). "Volume Estimation of Stem Segments Based on a Tetrahedron Model Using Terrestrial Laser Scanning Data". In: *Remote Sensing* 15.20 (20), p. 5060. ISSN: 2072-4292. DOI: 10.3390/rs15205060. URL: https://www.mdpi.com/2072-4292/15/20/5060 (visited on 07/12/2025).

Yun, Ting, Feng An, Weizheng Li, Yuan Sun, Lin Cao, and Lianfeng Xue (Nov. 2016). "A Novel Approach for Retrieving Tree Leaf Area from Ground-Based LiDAR". In: *Remote Sensing* 8.11 (11), p. 942. ISSN: 2072-4292. DOI: 10.3390/rs8110942. URL: https://www.mdpi.com/2072-4292/8/11/942 (visited on 07/12/2025).

Zhang, Zhilin, Bensheng Huang, Chao Tan, and Xiangju Cheng (Sept. 6, 2021). "A Study on the Drag Coefficient in Wave Attenuation by Vegetation". In: *Hydrology and Earth System Sciences* 25.9, pp. 4825–4834. ISSN: 1607-7938. DOI: 10.5194/hess-25-4825-2021. URL: https://hess.copernicus.org/articles/25/4825/2021/ (visited on 08/06/2025).

Zhao, Yuting, Jungho Im, Zhen Zhen, and Yinghui Zhao (Dec. 31, 2023). "Towards Accurate Individual Tree Parameters Estimation in Dense Forest: Optimized Coarse-to-Fine Algorithms for Registering UAV and Terrestrial LiDAR Data". In: *GIScience & Remote*

Sensing 60.1, p. 2197281. ISSN: 1548-1603. DOI: 10.1080/15481603.2023.2197281. URL: https://doi.org/10.1080/15481603.2023.2197281 (visited on 09/04/2025).